Development of a generic multi-analyte optical sensor platform for fluorescence-based sensing.

by

Orla McGaughey B.Sc. (Double Hons)

A thesis presented

to

Dublin City University

For the degree of Doctor of Philosophy

Research Supervisor:
Prof. Brian MacCraith
School of Physical Sciences
Dublin City University

July 2006

Declaration

I hereby certify that this material, which I now submit for assessment on the programme of study leading to the award of Doctor of Philosophy is entirely my own work and has not been taken from the work of others save and to the extent that such work has been cited and acknowledged within the text of my work.

Signed: ..... (Candidate)
ID No.: 51185300
Date: 10/07/06

Acknowledgements

I would like to thank all the members of the Optical Sensors Lab past and present for the help in all things technical as well as making my time spent in DCU an enjoyable social time. I would like to thank my supervisor Brian MacCraith for giving me this brilliant opportunity. In particular, I would like to thank two members of OSL who I don't think I would have got this far without. Firstly, Aisling McEvoy for all her help, support and encouragement throughout my time here. Secondly to Adam for help with all set-ups electronic or mechanical, support throughout the research and also looking after me and trying to keep me somewhat calm during the writing-up and viva time. I got through it in the end. I would also like to thank all the members of the Physics Department and the staff in the NCSR .

Outside of DCU, the one person I would like to thank is my dad, Tommy, for his help throughout both my undergrad and postgrad spells in college. At last, I am no longer a poor student. I know I didn't get the thesis finished quick enough for somebody but hopefully the graduation will be better late than never.

Contents

Abstract

This work describes the development of two advanced sensor platforms based on different spectroscopic techniques. The first, and the primary focus of this work, is an enhanced generic multi-analyte sensor platform for fluorescence-based sensors and the second is an absorbance-based portable sensor for the detection of nitrates in groundwater.

A generic multi-analyte sensor platform can be applied to a broad range of areas such as food packaging and blood gas analysis. A multi-analyte optical sensor platform for enhanced capture of fluorescence was modelled, designed and fabricated. The sensor platform was developed using a range of microfabrication techniques. Films sensitive to oxygen, relative humidity and carbon dioxide respectively were developed for the context of indoor air-quality monitoring. Deposition methods for printing the sensor solutions onto the sensor platforms were also investigated. The sensor films and platforms were integrated into a working sensor chip with both a fluorescence intensity and phase fluorometric detection system.

An absorbance-based portable sensor for the detection of nitrates in groundwater was also developed. This was based on the direct absorbance of UV-light by the nitrate ion. Other contaminants, which could be found in groundwater and interfere with the nitrate detection, such as humic acid and chlorides, were investigated and compensated for.

Chapter 1

Introduction

1.1 Introduction

Sensors are now prevalent in modern day society. A sensor is a device which is capable of reliably and repeatably monitoring a physical, chemical or biological process. Sensor applications are extensive in medical, environmental and industrial processes and, for example, include automotive sensors, blood-pressure monitors, water-quality sensors and biosensors. New sensors are constantly being developed and applied in a range of industries. Sensors use a wide range of transduction mechanisms including thermal, electrical, mechanical, chemical, optical and acoustic methods to provide a sensor output in a useful form. The particular method of transduction dealt with in this thesis is optical. The signal from optical sensors is generated using different optical mechanisms such as fluorescence, absorption and other spectroscopies. Recent developments in optical sensors have been aided by advances in a range of fields including

- Low-cost optoelectronic components
- Microfabrication technology
- Sol-gel fluorescent dye immobilisation methods

The main focus of the work presented in this thesis was to develop a generic sensor platform based on a range of methods for efficient excitation and detection of fluorescence. The ability to measure several analytes simultaneously extends the applications for optical sensors. Such platforms are required to be low-cost

and mass-producible while maintaining the required sensor performance. A multi-analyte sensor platform such as that developed here can be used in areas ranging from blood-gas monitoring - which would add the necessity of a disposable platform - to indoor air-quality monitoring. In the first instance, the generic platform developed was applied to the field of indoor air-quality monitoring.

1.2 Optical Sensors and Applications

An optical sensor senses a physical parameter or the amount of a chemical or biological substance present by monitoring the variation in some light parameter. Optical sensors have been widely developed to monitor physical parameters such as temperature [1,2] and pressure [3], and biological samples with a range of biosensors [4,5]. The focus of the work developed in this thesis, however, is optical chemical sensing. Most optical chemical sensors can be split into three main categories:

1. Refractometric sensors
   Refractometric sensors are based on the change in refractive index due to the influence of the analyte to be sensed. Refractometric sensors are widely used and a typical application is in the area of relative humidity sensing [6]. Refractometric sensors were not used in the course of this work.

2. Absorption-based sensors
   Absorption-based sensors can be further split into two categories the first being direct measurement of absorbance and the second based on measurement of a colour change in an intermediate complex. Direct spectroscopic methods can be used to sense a range of compounds at a variety of wavelengths. For example, in the infrared region, water, acetone and formaldehyde [7] can be sensed directly while nitrate can be sensed directly in the UV region [8]. Nitrate sensing will be discussed in detail in Chapter 2. The second method is an indirect measurement of the analyte which is based on the absorbance properties of an analyte-sensitive reagent. An example of this is colorimetric pH sensing [9]. In theory, direct absorbance measurements would be the preferred method of optical absorption-based sensing but in practice there are limitations associated with these measurements in the development of low-cost portable sensing systems. The wavelengths where direct absorption takes place are normally in the UV and IR regions while the indirect measurements

can take place in the visible region where there is a wide range of commercially available optoelectronic components which can be used in miniaturised portable sensors.

3. Fluorescence-based sensors
   In fluorescence-based sensors the analyte to be sensed alters the fluorescence properties of the analyte-sensitive material. Frequently, this results in a reduction of fluorescence, so-called quenching. Fluorescence-based sensors have many applications including sensors for oxygen, carbon dioxide and relative humidity [10]. Fluorescence-based sensors are used in the development of the multi-analyte sensor platform reported in this work and are described in more detail in Chapter 5.

Optical sensing was chosen as the transduction mechanism due to its many advantages. The interaction between the analyte to be sensed and the sensor takes place in a reversible manner without any consumption of the analyte. Optical sensors can safely be used in environments where electronic systems are unsuitable as they are immune to electromagnetic interferences. Optical sensors can benefit from the development of a wide range of low-cost optoelectronic components which can be used to develop miniaturised sensor platforms. While optical sensors have many advantages they also have some disadvantages which need to be taken into account for sensor development. Direct measurement of light intensity is prone to drift due to many factors such as differences in sensor position and interference of ambient light. The use of lock-in detection eliminates some of these problems. Measurement of fluorescence lifetime is not prone to many of the factors that cause drift in intensity-based measurements. One method of lifetime-based sensing employs a technique called phase fluorometry which generates a phase shift proportional to the sensor lifetime. This eliminates the main problems with optical intensity measurements. The optoelectronic components used in any optical sensor detection system are prone to drift over time and with temperature. This introduces the need for referencing of the sensor output and temperature compensation also needs to be employed.

The first optical sensor developed in the course of this work was an absorbance-based sensor for the detection of nitrates in groundwater. This sensor was based on direct absorbance of the nitrate ion in the UV-region. Direct absorbance measurements are highly desirable as they provide an intrinsic measurement of the analyte

concentration without the necessity of an intermediate complex. While this is a distinct advantage over fluorescence-based sensing, the absorbing wavelengths of many analytes is in the UV and IR ranges of the spectrum for which low-cost opto-electronic components are only beginning to become available. Conversely, fluorescent indicator dyes for a range of analytes have been identified with excitation and emission wavelengths in the visible region which can take advantage of the wide range of low-cost opto-electronic components available and develop the sensors in truly miniaturised and portable sensor probes rather than lab-based measurement systems. Another advantage of fluorescence is that it is more difficult to accurately measure very small absorbances that are very close to zero absorbance rather than small fluorescence levels [11]. While in theory the range of applications of fluorescence-based sensors are less than absorbance-based sensors as a suitable dye fluorescent dye complex needs to be identified for each application - a large range of fluorescence-based sensor probes have been developed due to instrumentation limitations in the part of absorbance-based sensor. Fluorescent indicator dye complexes are available for the analytes of interest to be sensed in the second part of the work in the development of a multi-analyte optical sensor platform. A large amount of development in fluorescence-based sensors has been undertaken internationally and efficient techniques for fluorescence detection are more widely developed than those for absorbance-based sensing. The main sensor development undertaken in the course of this thesis was thus in the area of fluorescence-based sensing. This work on fluorescence-based sensing concentrates on the development of efficient sensor platforms and detection methods to obtain the optimum detection of fluorescence. Other methods of improving the performance of fluorescence-based sensors has involved amplification of the fluorescence signal using many methods including, for example, signal amplification by means of encapsulating the fluorophore in a metal nanoparticle or using surface plasmon resonance [12]. These techniques were not investigated in this work as the efficient capture of the emitted fluorescence gave rise to a sensor performance which superseded the requirements for the chosen sensor application.

The application for the fluorescence-based generic multi-analyte sensor platform reported here is indoor air quality monitoring. Air-quality monitoring is widely used in any building or car with condition control. A high level of indoor air-quality is required to prevent transmission of various airborne illnesses and continual monitoring of air quality can reduce costs by supplying condition control on demand [13].

When, for example, the oxygen concentration reaches a dangerously low level for human comfort or health, the sensor could trigger a change in the condition control parameters. The ability to measure several analytes simultaneously on a single sensor platform is an advantage in this application, as multiple analytes need to be monitored continually. Optical sensor films have been developed for the main analytes of interest for air quality monitoring i.e. oxygen, relative humidity and carbon dioxide. All of these sensor films are based on changes in fluorescence of a specific indicator dye when exposed to the analyte of interest. The principle of sensing the different analytes are described in turn.

1.2.1 Oxygen sensors

The determination of oxygen concentration is of major importance in many industrial, medical and environmental applications due to its ubiquitous nature. Some of the most common applications for oxygen sensors are in the measurement of respiration and the production of oxygen, the measurement of the performance of internal combustion engines and by divers to measure the amount of oxygen in their tanks. Most of the early work on the development of oxygen sensors concentrated on electrode-based sensors. Zirconia and titania electrodes are used for measuring gaseous oxygen while the Clark electrode is widely used for the measurement of dissolved oxygen [14]. Optical oxygen sensors are more attractive than the electrode-based sensors as they do not consume oxygen and readily lend themselves to the production of miniaturised sensor devices. Much work has been done on the development of sensors for both gaseous and dissolved oxygen. The work presented in this thesis solely focusses on gas-based sensing.

One example of an absorption-based sensor is based on the absorbance change of a bis(histidinato)cobalt(II) solution in the presence of oxygen [15]. The majority of optical oxygen sensors are based on the quenching of fluorescence of a fluorescent complex in the presence of oxygen. Many fluorescent dyes have been used for oxygen sensing including, for example, porphyrin complexes [16] and erythrosin B [17]. The most common dyes used are ruthenium-based complexes. The ruthenium complex, ruthenium(II)-tris-(4,7-diphenyl-1,10-phenanthroline)Cl_2, was initially employed in this research group as an intensity-based sensor [18–21] and then later as a phase-fluorometry-based sensor [22, 23]. The sol-gel immobilisation matrix used for the ruthenium complex can be used to tailor the properties required for the particular

sensing application such as hydrophobicity or hydrophilicity. The oxygen sensors developed and their immobilisation matrices will be described in detail in Chapter 5.

1.2.2 Relative humidity sensors

The measurement of relative humidity is of importance in a wide variety of areas, including the food industry, the manufacture of moisture-sensitive products and medical equipment such as sterilisers and incubators [24]. Another application area (and the focus of the work reported here) is that of indoor air quality monitoring. The relative humidity of a water vapour-air mixture is defined as the ratio of the partial pressure of water vapour present in the gas and the saturation vapour pressure of the gas at a given temperature. It is normally expressed as a percentage, %RH [25]. Traditional methods of measuring humidity include the use of psychrometers, involving the measurement of temperatures of wet-bulb and dry-bulb thermometers, mechanical hygrometers, using strain gauges to measure expansion or contraction of a material as a function of humidity changes and mass-sensitive devices, based on the increase in mass of a material due to adsorption of humidity [24]. Recently, many relative humidity sensors have been developed based on changes in electronic properties such as capacitance [26, 27], and resistance [26, 28, 29]. However, relative humidity sensors are often needed in situations where the aforementioned methods are inconvenient or unsuitable, and may not be suited to continuous on-line monitoring. Optical sensors can safely be used in environments where electronic systems are unsuitable as they are immune to electromagnetic interferences [30]. The majority of optical sensors for relative humidity can be divided into two main categories: absorption-based sensors [31–36] and fluorescence-based sensors [25, 30, 37–45]. The optical sensor presented in this thesis is based on the changes in fluorescence intensity and/or emission lifetime of an indicator dye. Most of the fluorescence-based optical sensors previously reported use intensity-based detection methods. Choi et al investigated the fluorescence intensity of Rhodamine 6G in a gelatin matrix [25]. The dye suffers from a very small Stokes shift, i.e. small difference between excitation and emission wavelengths ($\Delta\lambda \approx$30 nm), which necessitates the use of expensive high quality optical filters. Posch et al developed a humidity sensor based on two perylene dyes immobilised on silica gel sheets [37]. The working range of this sensor is limited due to a discontinuous response to relative humidity. Other dyes that have been investigated

include umbelliferon [38] and fluorescein [39], which have the disadvantage of low Stokes shifts (as above), and lead to difficulty in selective detection of luminescence emission. Porphyrin dyes [41] have also been used and incorporated into Langmuir-Blodgett (LB) films. Lifetime-based detection methods for humidity sensing have been investigated using an osmium dye complex [43] and a ruthenium dye complex [44, 45]. Chang et al investigated an osmium complex as a solid sensor for water content in organic solvents [43]. A ruthenium complex was used by Glenn et al as a sensor for both water content in organic solvents and relative humidity [44]. This sensor employed a complex entrapment and conditioning procedure and required daily calibration. The sensor response was negligible after five days. This ruthenium complex was again used by Bedoya et al and was this time immobilised in a polymer membrane [45].

The relative humidity sensor developed in the course of this work was based on the fluorescence of a ruthenium complex encapsulated in a sol-gel matrix. The sensor mechanism and its fabrication will be described in more detail in Chapter 5.

1.2.3 Carbon dioxide sensors

The development of sensors for the measurement of carbon dioxide concentration is of major importance for many industrial, biomedical and environmental applications. Carbon dioxide is a key parameter in many processes as a result of its vital role in animal and plant metabolism and photosynthesis. The measuring of CO_2 is crucial in the measurement of respiration in the medical area; in the monitoring of fermentation and other industrial bioprocesses; in the monitoring of environmental issues due to the influence CO_2 has on the environment. Originally, the main methods of monitoring CO_2 were using its absorption of infrared radiation for gaseous CO_2 [46] and the use of the Severinghaus electrode for dissolved CO_2 [47]. However the infrared technique is not suitable for measurement of dissolved CO_2 and is limited when measuring gaseous due to it being prone to interference, requiring long path lengths and being both bulky and expensive. The Severinghaus electrode utilises a pH electrode, placed in contact with a thin layer of an aqueous sodium bicarbonate solution. As the CO_2 interacts with the layer it causes a change in the pH which is measured by the pH electrode. The change in pH is related to the partial pressure of CO_2. However, the electrode is bulky, expensive, prone to electrical interference and interference from acidic and basic gases and exhibits slow response

and recovery times. Recently there has been much progress in the development of optical CO_2 sensors. Some work has been carried out on absorbance-based sensors [48,49] but the majority of sensors are fluorescence-based. Most of the optical CO_2 sensors developed take advantage of the change in fluorescence of an indicator dye when the pH of the surrounding medium, normally water, is altered by changing CO_2 concentration [50]. The mechanism of this pH reaction to sense carbon dioxide is described in detail in Chapter 5. The most common indicator dye, and the one used in the course of this work, is hydroxy pyrene trisulfonic acid (HPTS). It is also known as pyranine. This indicator dye can be used with widely available optoelectronic components. Due to the very short lifetime of HPTS, the phase shift can not be measured using the standard experimental fluorescence detection system. A new technique called dual luminophore referencing (DLR) is used to overcome this problem and will also be discussed in Chapter 5.

1.2.4 Application of fluorescence-based multi-analyte sensor platform

The generic fluorescence-based optical sensor platform can be demonstrated in a wide range of areas including for example, food packaging, blood-gas monitoring and indoor air-quality monitoring. As mentioned above, it was decided to demonstrate the effectiveness of the sensor platform in the area of indoor air-quality monitoring. Some applications within this area could include: demand control air-conditioning systems for buildings, condition control monitoring for vehicles or also closed-container monitoring to detect the presence of stowaways in vehicles. The optical sensor films developed for indoor air-quality monitoring - oxygen, relative humidity and carbon dioxide - have been described above. The application ranges of concentrations of interest for these sensors i.e. 0-50% oxygen (in particular 18-22%), 0-50% relative humidity and 0-20% carbon dioxide (in particular 0-2%) are used to evaluate the sensor platform performance. The minimum resolution required for this application is in the order of 0.5% for the oxygen sensor and in the order of a full percent for both the relative humidity and carbon dioxide sensors for human comfort [13].

1.3 Optical Waveguides

Optical waveguides are structures that transport light through a medium. These waveguides form the basis of the optical sensor platforms developed in this work. The fluorescence from an optical sensor film is coupled efficiently into a particular waveguide and is then transported to where it will be detected. Optical waveguides transport light by means of total internal reflection at the interfaces between the waveguide and the various media surrounding it. Waveguides can be split into two main categories: optical fibres and planar waveguide platforms. Planar waveguide platforms were used in the development of a multi-analyte sensor platform. The theory underlying the propagation of light in waveguides and how light can be coupled into and out of waveguides is described in this thesis in the context of developing an efficient optical sensor platform.

1.4 Sol-gel Technology

Sol-gel technology can be used in the development of optical sensors. Sol-gel technology enables the fabrication of glass-like structures at relatively low temperatures. The properties of these structures can be modified by changing the starting materials and process used in sol-gel fabrication which enable the structure to be tailored to suit a particular application. Sol-gel technology was used in this work to provide an immobilisation matrix for a fluorescent dye complex. This matrix entraps the dye while the particular analyte to be sensed can diffuse through the sol-gel matrix and interact with the dye and cause changes in fluorescence. The use of sol-gel also enables ease of fabrication of sensor platforms as thin films can be deposited on a wide range of substrates with a range of geometries using different deposition techniques at an early stage in the sol-gel development. These sensor immobilisation methods have been used to sense a wide range of analytes. Sol-gel technology was also used in this work in the development of a sensor platform. In this case, UV-curable sol-gel was used to form a waveguide structure to support the optical sensor films. Again the ability to tailor the properties of the material enabled refractive index modification of the layers allowing them to be used as a waveguide.

1.5 Microfabrication

One of the factors driving optical chemical sensor technology is the development of low-cost mass-producible and disposable sensor platforms. One of the factors to ensure that a sensor platform can satisfy the low-cost requirement is the elimination of an expensive inflexible fixed mask from which platforms can be made. In the development of a sensor platform, rapid prototyping technologies are desirable to realise the design and development of a platform that is ready for testing within 24 hours. Some of the polymer platforms that were fabricated as multi-analyte sensor platforms could be drawn in a CAD software package and this design used to control a laser to fabricate the platform. The platform could be developed in a matter of hours without the need for any specific fixed masks to be purchased which made the platform easily adaptable.

The sensor platforms used a range of fabrication techniques some of which came from the set of techniques called soft lithography. These methods used a rubber stamp as a patterning element and enable the rapid prototyping of platforms of various geometries and materials. These microfabrication techniques are described in detail throughout the thesis. Sensor platforms were fabricated from both polymer materials and sol-gel materials in the course of this project. A range of deposition methods were used in the course of this work for fabrication of the sol-gel waveguide platform and to deposit sensor films onto the different sensor platforms.

1.6 Thesis Objectives

The main aim of this work was the development of a generic multi-analyte optical sensor platform. This platform should be miniaturised, low-cost and mass-producible while maintaining an efficient capture of fluorescence signal. The secondary aim of this work was the development of a portable nitrate sensor. The specific objectives for this work were:

- To develop a portable absorbance-based nitrate sensor and compensate for possible interferents.
- To design an efficient sensor platform for multi-analyte sensing
- To develop a range of optical sensor films to demonstrate the effectiveness of the sensor platform

- To fabricate the sensor platform and to deposit optical sensor films onto that platform using a range of microfabrication and rapid prototyping techniques
- To integrate the sensor platform and sensor films into a working sensor device with its associated optoelectronic components

1.7 Thesis Structure

One body of work carried out in the course of this work was the development of a portable absorbance-based sensor for nitrates in groundwater. This work is detailed in Chapter 2. The sensor was developed in the laboratory and then adapted for use in the field. The nitrate level in water samples could be measured by the absorption of the nitrate ion in the UV region. Other compounds which could be present in groundwater and interfere with the detection of nitrate were investigated and their effects noted and compensated for.

The remaining chapters deal with the development of the generic multi-analyte optical sensor platform for fluorescence-based sensing. Chapter 3 describes the sol-gel process and the various factors which affect it. The application of this technology to the fabrication of sensor platforms and as an immobilisation matrix for fluorescent dyes are outlined.

Chapter 4 categorises the various types of optical waveguides. The mechanism whereby light is trapped in the waveguide and guided along its length by total internal reflection is described. The number of modes a waveguide is able to support and the fact that some of the light carried by the waveguide is present in the material outside the waveguide is also discussed.

Chapter 5 defines the principles of fluorescence and the development and operation of fluorescence-based sensors for the analytes chosen in this work i.e. oxygen, relative humidity and carbon dioxide. The various methods of detection of fluorescence signal from an optical sensor are also detailed.

Chapter 6 explains the underlying theory in the development of a generic multi-analyte optical sensor platform. The sensor platform configuration used is illustrated and the way in which fluorescence from a sensor film is coupled into a sensor platform is modelled.

Chapter 7 details the microfabrication and deposition techniques used in the fabrication of the sensor platforms. The platforms were fabricated using both poly-

mer and UV-curable sol-gel materials and both of these approaches are discussed.

Chapter 8 reports on the various experimental characterisation systems developed to monitor the fluorescence signal from an optical sensor. The evolution of this system is described through its stages necessitated by the requirements of the particular sensor platforms. Calibration systems are also developed for the different analytes sensed in this work.

Chapter 9 describes the results obtained in the development of a multi-analyte optical sensor platform. It details the results obtained from the sensor platforms made from both UV-curable sol-gel and polymer. The development of each of the optical sensor films is described in turn along with their cross-sensitivity to the other analytes being sensed. Finally, simultaneous sensing of multiple analytes is demonstrated.

Chapter 10 draws conclusions from the work developed here and also discusses future possibilities and applications for the work.

Bibliography

[1] K.T.V. Grattan and Z.Y. Zhang. *Fiber Optic Fluorescence Thermometry.* Chapman & Hall, London, 1994.

[2] J.N. Demas and B.A. DeGraff. On the design of luminescence based temperature sensors. *Proc. SPIE*, 1796:71–80, 1992.

[3] J. Hradil, C. Davis, K. Mongey, C. McDonagh, and B. D. MacCraith. Temperature-corrected pressure-sensitive paint measurements using a single camera and a dual-lifetime approach. *Measurement Science & Technology*, 13(10):1552–1557, 2002.

[4] C. A. Rowe, L. M. Tender, M. J. Feldstein, J. P. Golden, S. B. Scruggs, B. D. MacCraith, J. J. Cras, and F. S. Ligler. Array biosensor for simultaneous identification of bacterial, viral, and protein analytes. *Analytical Chemistry*, 71(17):3846–3852, 1999.

[5] H. McEvoy. *Development and optimisation of patterned optical immunosensors.* Ph.D. Thesis, Dublin City University, 2005.

[6] K. R. Kribich, R. Copperwhite, H. Barry, B. Kolodziejczyk, J. M. Sabattié, K. O'Dwyer, and B. D. MacCraith. Novel chemical sensor/biosensor platform based on optical multimode interference (MMI) couplers. *Sensors and Actuators B: Chemical*, 107(1):188–192, 2005.

[7] J. Donohue. *Development of chemical sensors using novel infrared sources.* M.Sc. Thesis, Dublin City University, 2006.

[8] C. Gibson, P. Byrne, O. McGaughey, H. Masterson, C. Haslinger, K. O'Dwyer, and B. D. MacCraith. Development of a robust nitrate sensor for water quality monitoring. *Paper in preparation.*

[9] C. S. Burke, L. Polerecky, and B. D. MacCraith. Design and fabrication of enhanced polymer waveguide platforms for absorption-based optical chemical sensors. *Measurement Science & Technology*, 15(6):1140–1145, 2004.

[10] O. McGaughey, R. Nooney, A.K. McEvoy, C. McDonagh, and B.D. MacCraith. Development of a multi-analyte integrated optical sensor platform for indoor air-quality monitoring. *Proc. SPIE*, 5993:172–183, 2005.

[11] J. Lakowicz. *Principles of Fluorescence Spectroscopy.* Plenum Press, New York, 2nd edition, 1999.

[12] O. Stranik, H.M. McEvoy, C. McDonagh, and B.D. MacCraith. Plasmonic enhancement of fluorescence for sensor applications. *Sensors and Actuators B: Chemical*, 107(1):148–153, 2005.

[13] P. Adrian. A multi-sensor package can be effective for IAQ monitoring. *Sensor Business Digest*, August, 2004.

[14] L. C. Clark. Monitor and control of blood and tissue oxygen tensions. *Transactions American Society for Artificial Internal Organs*, 2:41–49, 1956.

[15] F. Baldini, M. Bacci, F. Cosi, and A. Delbianco. Absorption-based optical-fiber oxygen sensor. *Sensors and Actuators B-Chemical*, 7(1-3):752–757, 1992.

[16] D.L. Dowling. *Optical oxygen sensing based on ruthenium and porphyrin complexes.* M.Sc. Thesis, Dublin City University, 2002.

[17] R. T. Bailey, F. R. Cruickshank, G. Deans, R. N. Gillanders, and M. C. Tedford. Characterization of a fluorescent sol-gel encapsulated erythrosin B dissolved oxygen sensor. *Analytica Chimica Acta*, 487(1):101–108, 2003.

[18] B. D. MacCraith, G. O'Keeffe, A. K. McEvoy, C. M. McDonagh, J. F. McGilp, B. O'Kelly, J. D. O'Mahony, and M. Cavanagh. Light-emitting-diode-based oxygen sensing using evanescent-wave excitation of a dye-doped sol-gel coating. *Optical Engineering*, 33(12):3861–3866, 1994.

[19] C. McDonagh, B. D. MacCraith, and A. K. McEvoy. Tailoring of sol-gel films for optical sensing of oxygen in gas and aqueous phase. *Analytical Chemistry*, 70(1):45–50, 1998.

[20] C. M. McDonagh, A. M. Shields, A. K. McEvoy, B. D. MacCraith, and J. F. Gouin. Optical sol-gel-based dissolved oxygen sensor: Progress towards a commercial instrument. *Journal of Sol-Gel Science and Technology*, 13(1-3):207–211, 1998.

[21] C. S. Burke, O. McGaughey, J. M. Sabattié, H. Barry, A. K. McEvoy, C. McDonagh, and B. D. MacCraith. Development of an integrated optic oxygen sensor using a novel, generic platform. *Analyst*, 130(1):41–45, 2005.

[22] D. Wencel, C. Higgins, A. Guckian, C. McDonagh, and B.D. MacCraith. Novel hybrid sol-gel materials for smart sensor windows. *Proc. SPIE*, 5826:696–705, 2005.

[23] C. McDonagh, C. Kolle, A. K. McEvoy, D. L. Dowling, A. A. Cafolla, S. J. Cullen, and B. D. MacCraith. Phase fluorometric dissolved oxygen sensor. *Sensors and Actuators B: Chemical*, 74(1-3):124–130, 2001.

[24] M. C. Moreno-Bondi, G. Orellana, and M. Bedoya. Fibre optic sensors for humidity monitoring. In O. S. Wolfbeis and R. Narayanaswamy, editors, *Optical Sensors: Industrial, Environmental and Diagnostic Applications*, pages 251–280. Springer-Verlag, Berlin, 2004.

[25] M. F. Choi and O. Ling Tse. Humidity-sensitive optode membrane based on a fluorescent dye immobilized in gelatin film. *Analytica Chimica Acta*, 378(1-3):127–134, 1999.

[26] Y. Sakai, Y. Sadaoka, and M. Matsuguchi. Humidity sensors based on polymer thin films. *Sensors and Actuators B: Chemical*, 35(1-3):85–90, 1996.

[27] C. Roman, O. Bodea, N. Prodan, A. Levi, E. Cordos, and I. Manoviciu. A capacitive-type humidity sensor using cross-linked poly(methyl methacrylate-co-(2 hydroxypropyl)-methacrylate). *Sensors and Actuators B: Chemical*, 25(1-3):710–713, 1995.

[28] A. Bearzotti, C. Caliendo, E. Verona, and A. D'Amico. Integrated optic sensor for the detection of H_2 concentrations. *Sensors and Actuators B: Chemical*, 7(1-3):685–688, 1992.

[29] G. Gusmano, G. Montesperelli, E. Traversa, and A. Bearzotti. Humidity-sensitive electrical properties of $MgAl_2O_4$ thin films. *Sensors and Actuators B: Chemical*, 14(1-3):525–527, 1993.

[30] S. Muto, H. Sato, and T. Hosaka. Optical humidity sensor using fluorescent plastic fiber and its application to breathing-condition monitor. *Japanese Journal of Applied Physics Part 1-Regular Papers Short Notes and Review Papers*, 33(10):6060–6064, 1994.

[31] L. I. Katzin and J. R. Ferraro. The system cobaltous chloride water acetone at 25-degrees. *Journal of the American Chemical Society*, 74(11):2752–2754, 1952.

[32] T. Asami. Determination of minute quantities of water in gas or liquid by cobaltous chloride indicator. *Analytical Chemistry*, 40(3):648–650, 1968.

[33] A. P. Russell and K. S. Fletcher. Optical sensor for the determination of moisture. *Analytica Chimica Acta*, 170:209–216, 1985.

[34] Q. Zhou, M. R. Shahriari, D. Kritz, and G. H. Sigel. Porous fiber-optic sensor for high-sensitivity humidity measurements. *Analytical Chemistry*, 60(20):2317–2320, 1988.

[35] F. Boltinghouse and K. Abel. Development of an optical relative-humidity sensor - cobalt chloride optical absorbency sensor study. *Analytical Chemistry*, 61(17):1863–1866, 1989.

[36] A. Kharaz and B. E. Jones. A distributed optical-fibre sensing system for multi-point humidity measurement. *Sensors and Actuators A: Physical*, 47(1-3):491–493, 1995.

[37] H. E. Posch and O. S. Wolfbeis. Optical sensors, 13: fibre-optic humidity sensor based on fluorescence quenching. *Sensors and Actuators*, 15(1):77–83, 1988.

[38] S. Muto, A. Fukasawa, M. Kamimura, F. Shinmura, and H. Ito. Fiber humidity sensor using fluorescent dye-doped plastics. *Japanese Journal of Applied Physics Part 2-Letters*, 28(6):L1065–L1066, 1989.

[39] S. Muto, A. Fukasawa, T. Ogawa, M. Morisawa, and H. Ito. Breathing monitor using dye-doped optical fiber. *Japanese Journal of Applied Physics Part 1-Regular Papers Short Notes and Review Papers*, 29(8):1618–1619, 1990.

[40] C. Zhu, F. V. Bright, W. A. Wyatt, and G. M. Hieftje. A new fluorescence sensor for quantification of atmospheric humidity. *Journal of the Electrochemical Society*, 136(2):567–570, 1989.

[41] D. B. Papkovsky, G. V. Ponomarev, S. F. Chernov, A. N. Ovchinnikov, and I. N. Kurochkin. Luminescence lifetime-based sensor for relative air humidity. *Sensors and Actuators B: Chemical*, 22(1):57–61, 1994.

[42] R. J. Bartlett, R. Philip-Chandy, P. Eldridge, D. F. Merchant, R. Morgan, and P. J. Scully. Plastic optical fibre sensors and devices. *Transactions of the Institute of Measurement and Control*, 22(5):431–457, 2000.

[43] Q. Chang, Z. Murtaza, J. R. Lakowicz, and G. Rao. A fluorescence lifetime-based solid sensor for water. *Analytica Chimica Acta*, 350(1-2):97–104, 1997.

[44] S. J. Glenn, B. M. Cullum, R. B. Nair, D. A. Nivens, C. J. Murphy, and S. M. Angel. Lifetime-based fiber-optic water sensor using a luminescent complex in a lithium-treated Nafion(TM) membrane. *Analytica Chimica Acta*, 448(1-2):1–8, 2001.

[45] M. Bedoya, M.T. Diez, M.C. Moreno-Bondi, and G. Orellana. Humidity sensing with a luminescent Ru(II) complex and phase-sensitive detection. *Sensors and Actuators B: Chemical*, 113(2):573–581, 2006.

[46] R. M. Mihalcea, D. S. Baer, and R. K. Hanson. Diode-laser absorption measurements of CO_2 near 2.0μm at elevated temperatures. *Applied Optics*, 37(36):8341–8347, 1998.

[47] S. Kojima, M. Loughran, and H. Suzuki. Microanalysis system for pO_2, pCO_2, and pH constructed with stacked modules. *IEEE Sensors Journal*, 5(5):1120–1126, 2005.

[48] A. Mills and Q. Chang. Colorimetric polymer film sensors for dissolved carbon dioxide. *Sensors and Actuators B: Chemical*, 21:83–89, 1994.

[49] B. H. Weigl, A. Holobar, N. V. Rodriguez, and O. S. Wolfbeis. Chemically and mechanically resistant carbon-dioxide optrode based on a covalently immobilized pH indicator. *Analytica Chimica Acta*, 282(2):335–343, 1993.

[50] A. Mills and Q. Chang. Fluorescence plastic thin-film sensor for carbon dioxide. *Analyst*, 118:839–843, 1993.

Chapter 2

Development of a Nitrate Sensor

2.1 Introduction

The aim of this work was to develop a portable sensor that could be used for measuring nitrate in water. The presence of nitrate concentrations in water can be detrimental to public health and cause environmental harm. High nitrate levels in water can cause a serious blood condition in infants known as methaemoglobinaemia ('blue baby syndrome') [1]. Nitrate is converted to nitrite in vivo and this subsequently reduces haemoglobin to methaemoglobin with a consequential reduction in oxygen carrying capacity leading to potential mental retardation. Nitrates represent a further potential health hazard in that they can react in the human stomach to produce N-nitroso compounds some of which are carcinogenic [1, 2]. The increase of nitrate concentrations in rivers and groundwater can be attributed to the application of nitrogen-rich fertiliser to agricultural land. Fertiliser run-off can thus contribute to eutrophication, the over-enrichment of surface waters resulting in ecological problems, particularly in static waters such as lakes and reservoirs.

Recent emphasis on compliance with national and EU directives on water quality sets a nitrate limit of 50ppm in surface waters [3], often expressed equivalently as 11.3ppm of nitrogen and has created a requirement for real-time in-situ monitoring of nitrates. The Irish Environmental Protection Agency currently monitors the levels of nitrates in ground-water by taking samples from three hundred locations and measuring these back at a laboratory. Our development of a portable sensor capable of taking in situ measurements can enable many more sites to be tested.

Many methods of nitrate sensing employ separation techniques requiring expensive instrumentation, and their reliance on a separation step limits their use

for continuous real-time measurements. Flow-Injection Analysis techniques exhibit the advantages of high versatility, high reproducibility and reliability, short reaction times and ease of automation. However, these methods require the reduction of nitrate to nitrous oxide and subsequent detection can involve reaction with environmentally detrimental gas [4] or carcinogenic compounds. Standard colorimetric methods [5, 6] require reagents and are also prone to interference in addition to requiring the sample to be optically clear which is often not the case in real in situ conditions. Electrochemical methods can also require the use of environmentally harmful and carcinogenic compounds in addition to requiring the use of a buffer solution to stabilise the system before measurement and are subject to fouling and drift [7, 8]. Biosensors have also been extensively investigated [9–11]. Co-immobilisation of enzyme and mediator at an electrode surface provides a reagentless technique. In all cases, the enzyme used to reduce the nitrate is nitrate reductase, NaR. The main drawbacks of using plant or E. coli NaR are the signal interference of other reducible compounds in the sample and the low stability of the NaR.

Other sensors exploit polarity-sensitive dyes immobilised in polymer matrices, which on exposure to nitrate emit a greater intensity of fluorescence. Fluorescence-based sensors have the advantages of being non-consuming and reversible as well as exhibiting high specificity and sensitivity [12–14]. Disadvantages include their dependence on temperature and pH. Commonly used indicator dyes are not sufficiently lipophilic and consequently they tend to leach out of the polymer membranes.

It has long been known that the nitrate ion absorbs UV light in the region of 210nm, allowing direct optical measurement [15]. In this spectral region the absorption is independent of pH. This is a particularly attractive sensing approach as it obviates the need for colorimetric agents that increase the complexity of the instrumentation design, and does not generate any bi-products. Karlsson et al reported such a spectroscopic technique combined with multivariate anaylsis [16]. This approach involved removing samples to the laboratory for filtering and preservation using sulphuric acid, thereby altering the original nature of the sample before using only 5 discrete wavelengths to build the model. More recently, artificial neural networks have been coupled with potentiometric detection over the range of 0.1 to 100ppm nitrate [17]. This sensor requires the use of four discrete sensors to obtain reliable measurements.

This chapter describes the development of a robust, reagent-less prototype employing UV spectrophotometry, requiring minimum maintenance, and designed to work in the field. The prototype takes advantage of recent progress in optoelectronic technology allowing optimisation of the measurement which has previously been hampered by instrumentation limitations. The sensor described is an improvement over the current state of the art as it provides a direct stable measurement of the nitrate concentration without the need for reagents, pre-treating of samples, or the use of environmentally harmful compounds. It operates in the concentration ranges of interest for nitrate detection in groundwater while also compensating for possible interferences present. The interferences, commonly present in groundwater, which could interfere with the measurement of absorbance of the nitrate ion (humic acid and chloride) were investigated. The sensor was first developed as a lab-based characterisation system and this was then improved upon and incorporated into a portable prototype which enabled continuous real-time monitoring of nitrate concentration. A chemometric model was developed and used to calibrate the sensor. This model uses absorbance values over the wavelength range from 200-250nm to compensate for interferences and other sources of drift in the measurement.

This sensor was developed as part of a project which was completed by several members of the Optical Sensors Laboratory. The design and fabrication of the required optical components for the portable sensor prototype was carried out by Dr Hugh Masterson and the chemometric model for sensor calibration was developed by Mr Pat Byrne and Dr Claudia Haslinger.

2.2 Absorbance-Based Sensing

Absorption spectroscopy is based on the absorption of electromagnetic radiation by a material, and the resulting reduction in optical power is related to the amount of absorbing material in the beam path. The emission from a source is directed onto a sample where it is absorbed. I_0 and I represent the optical intensity before and after absorption, respectively. The drop in optical intensity is sensed with a suitable detector, and the measured drop is related to the quantity of absorbing species in the sample. The property A is defined as the absorbance of the absorber, and is given by

$$A = \log_{10} \frac{I_0}{I} = \varepsilon l C \tag{2.1}$$

which is better known as the Beer-Lambert Law where l is the optical path length, C is the absorber concentration and ε is the molar absorptivity [18]. This law enables the use of spectroscopic analysis, as it states that the absorbance of a particular substance remains constant as long as its concentration and optical path length remain constant. Also, in a cell of fixed length, any change in the absorbance of a substance must be due to a change in concentration. As discussed previously, this sensor is based on the absorbance of UV radiation by the nitrate ion.

2.3 Lab-Based Characterisation System

The initial lab-based system developed in this work is illustrated in Figure 2.1. The UV light, from a deuterium lamp (DTM6 UV-Vis Fibrelight; Heraeus, Germany), is launched into an Ocean Optics reflectance probe (R200-7-UV/VIS; Ocean Optics, The Netherlands). The signal is then reflected back to an Ocean Optics UV-Vis Spectrophotometer (S2000; Ocean Optics, The Netherlands). Different concentrations of nitrate and interfering species were used evaluate sensor performance. Initial proof of principle measurements were carried out on this apparatus.

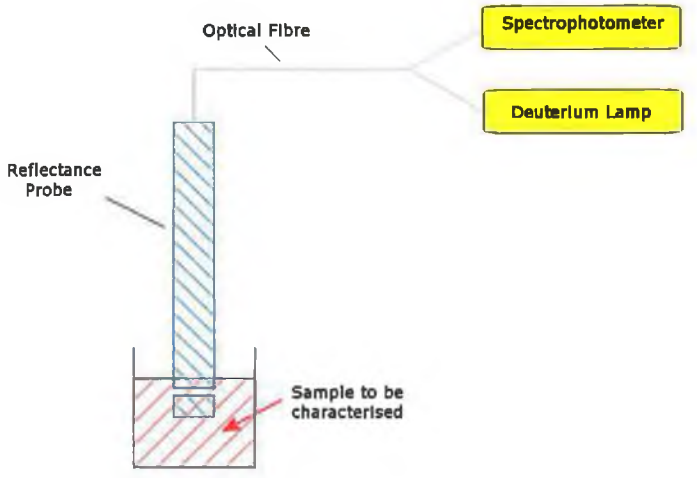

Figure 2.1: Nitrate sensor - Initial lab-based setup.

2.3.1 Nitrate absorbance

The first spectra to be taken were for different nitrate concentrations. Absorbance spectra for 1ppm to 90ppm nitrate are shown in Figure 2.2. The increase in absorbance with increasing nitrate concentrations can be seen within the range 200-250nm. The sensor is most sensitive from 0-50ppm i.e. the greatest change in absorbance occurs. Between 50ppm and 90ppm this sensor configuration still shows a measurable change in nitrate absorbance. This suits the stated objectives for a required sensitivity from 0-50ppm nitrate.

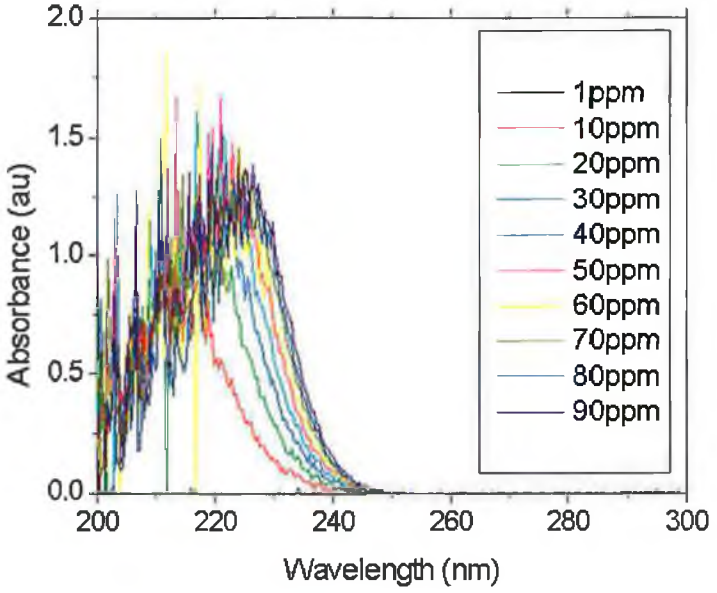

Figure 2.2: Sodium nitrate absorbance 1-90ppm - Initial lab-based setup.

This spectrophotometer gives a noisy signal in the wavelength range of interest for nitrate sensing. At nitrate concentrations above 60ppm, the absorbance difference between the concentrations becomes smaller and the noise is a much larger influence. The nitrate signal could only be monitored above 220nm using this spectrophotometer which eliminated approximately half the working range of the sensor as the nitrate absorbance varies mainly from 200-240nm.

2.3.2 Interferences

Humates are sold as fertilisers which increase the overall content of nitrogen and nitrates in the soil. On dissolution in water, humates produce humic acid which is thus often present as a contaminant in ground and surface water bodies due to run off after excessive fertiliser application to agricultural soil. It is a large organic compound with wide ranges of molecular weight and size. Humic acid is a potential interferent for nitrate measurements [19]. The absorbance of humic acid alone was investigated and the results shown in Figure 2.3. It was found that humic acid absorbs in the same region as nitrate. From a calibration plot, Figure 2.4, of the absorbance of humic acid it was shown that the absorbance is linear with increasing humic acid concentration.

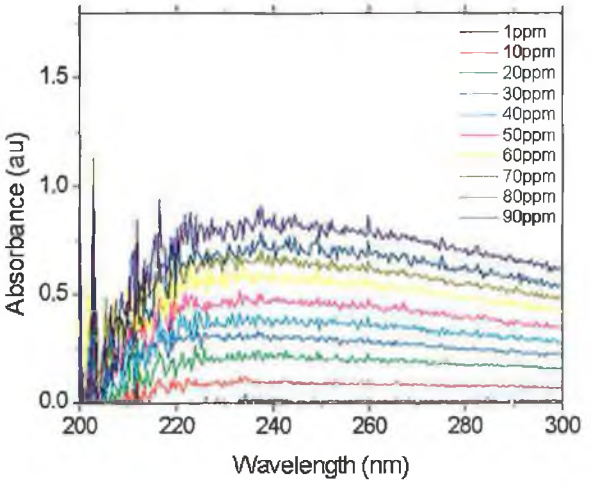

Figure 2.3: Humic acid absorbance 1-90ppm - Initial lab-based setup.

Humic acid concentration is not directly measured as a water quality parameter. It is only indirectly gauged from colour measurements carried out as standard and recorded in hazen units [20]. There is no limit defined for colour of drinking water. The Environmental Protection Agency of Ireland guidelines state 'Acceptable to consumers and no abnormal change' [3]. Thus humic acid solutions were spectroscopically compared to a selection of colour standards using a 10mm path length cuvette in a 50-Scan, Varian Cary UV/Vis spectrophotometer (JVA Analytical Ltd; Dublin). The spectra shown in Figure 2.5 compare the absorption of the two types

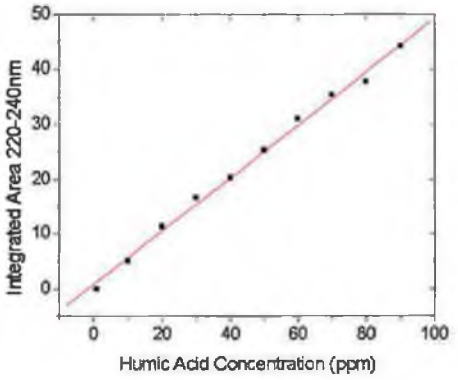

Figure 2.4: Humic acid calibration plot - Initial lab-based setup.

of solution. The graph clearly contrasts the spectroscopic features and provides a good illustration of the importance of using humic acid solutions rather than hazen colour standards whilst developing a calibration for the sensor.

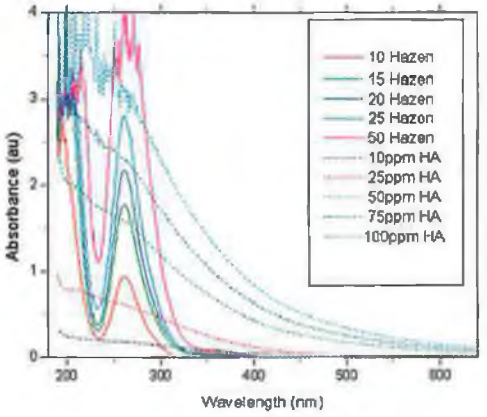

Figure 2.5: Comparison of spectra resulting from Humic Acid and Colour Standards. Humic Acid (HA) spectra shown as dotted lines. Colour Standard spectra shown as solid lines.

2.4 Prototype-Based System

After the feasibility of the sensing mechanism was demonstrated, a prototype system was developed. From the initial work the performance of the spectrophotometer was evaluated. The Ocean Optics spectrophotometer, used in the lab characterisation system (Section 2.3) gave a very noisy signal from 200-220nm. As this is a large fraction of within our nitrate absorption range an alternative was sought. A new spectrophotometer (EPP2000C; Stellar Net Inc., England) was found which exhibited less noise in the wavelength range of interest as shown in Figure 2.6.

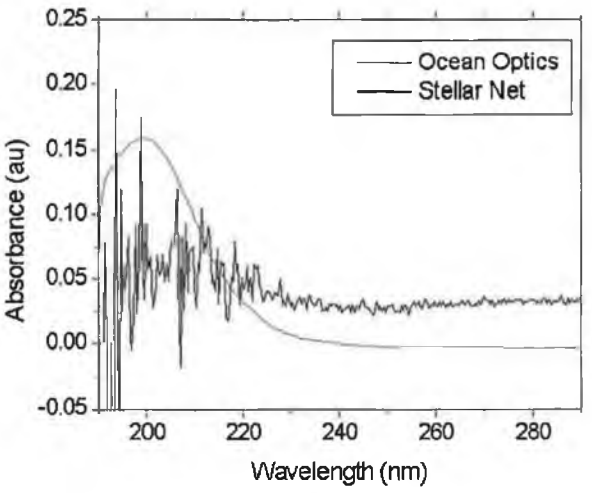

Figure 2.6: Spectrophotometer performance from 200-300nm for a 1ppm nitrate solution.

The new prototype was designed by Dr. Hugh Masterson, another member of the Optical Sensors Laboratory, around this new spectrophotometer and the miniaturised Fibrelight source. A schematic of the prototype design is shown in Figure 2.7. The microspectrometer and light source are connected to the sensor probe head using UV-transmitting optical fibres. The fibres are protected using stainless steel tubing. Light from the UV source is delivered to the sensor head via the optic fibre and traverses the sample by reflection from mirrors angled at 90° to each other and at 45° with respect to the axis. The return beam is focused into a second optical fibre parallel to the first one and is delivered to the microspectrometer for detection and data processing.

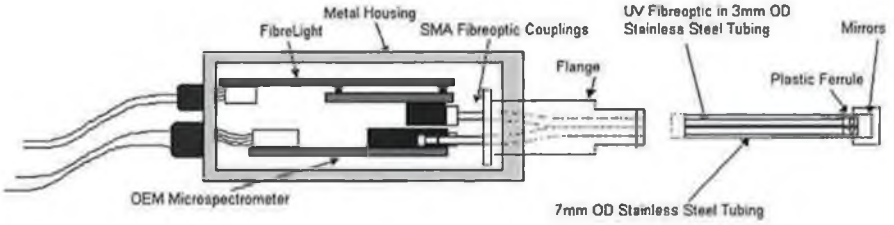

Figure 2.7: Nitrate sensor prototype design.

At the sensor head of the probe the two collinear tubes are parallel and in contact with one another. The end of the tubing section is machined to fit into the last part of the optical sensor head which creates the fluid chamber and supports the mirrors. The sensor probe-head is shown in Figure 2.8. The path length of the sensor head can be varied to allow optimisation of the absorption signal and to prevent saturation in strongly absorbing solutions. The use of the new spectrophotometer, deuterium light source and non-solarising optical fibre enabled the development of a portable sensor prototype for nitrate sensing, removing the current necessity for lab-based measurement and enabling real-time in-situ continuous monitoring of nitrate concentrations.

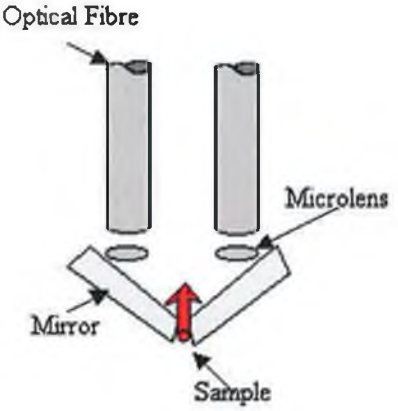

Figure 2.8: Nitrate sensor prototype: probe-head design.

2.4.1 Nitrate absorbance

As for the lab-based characterisation system, the absorbance of sodium nitrate in pure water samples was first investigated. This was done for 1-100ppm Nitrate and is shown in Figure 2.9. As before the sensor is most sensitive from 0-50ppm. The absorbance peak shifts to higher wavelengths with increasing nitrate concentration.

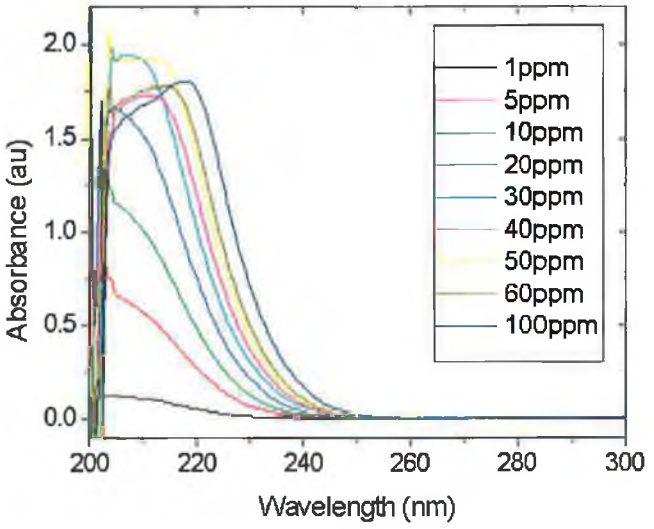

Figure 2.9: Nitrate absorbance 1-100ppm measured using portable sensor prototype.

2.4.2 Interferences

Nitrate solutions were dosed with different inteferening species (e.g. humic acid and sodium chloride) to investigate the effect on nitrate detection. Nitrate solution was first contaminated with humic acid. Figure 2.10 shows the effect of dosing humic acid, up to 50ppm, into a solution of 20ppm nitrate. When the humic acid concentration was increased to 30ppm the absorbance of nitrate was completely masked thus the effect of humic acid on nitrate absorption must be considered for sensor calibration.

The other interference investigated was sodium chloride. Sodium chloride was added to 5ppm, 20ppm and 50ppm nitrate respectively and the absorbance spectra

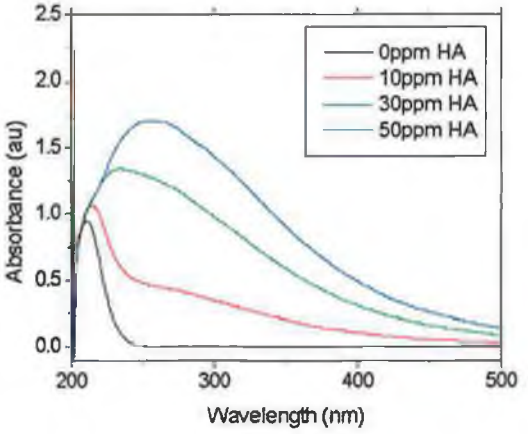

Figure 2.10: 20ppm nitrate absorbance dosing in humic acid (HA).

are shown in Figure 2.11. The addition of sodium chloride leads to a small increase in absorbance. This is only significant enough to interfere with the detection of nitrate for chloride concentrations above approx 200ppm. From data of raw water in the Dublin City area the chloride concentration is within the range 7 to 19ppm [21] and thus does not interfere with measurement of nitrate absorption in this area.

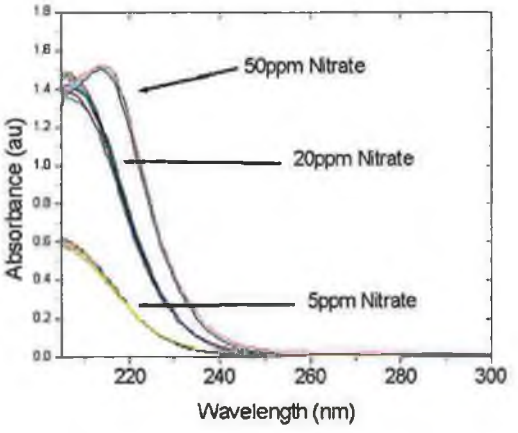

Figure 2.11: Nitrate absorbance dosing in sodium chloride.

2.5 Chemometric Model

A chemometric model was developed and tested in the research group (by Mr Pat Byrne and Dr Claudia Haslinger) to develop a calibration model for the nitrate sensor. This model used all the experimental data which was obtained with the portable sensor prototype and as described above to develop a model for determining nitrate concentration in both clean water or pre-treated samples and also in samples which contained the interferent humic acid. This model also compensated for the fact that the peak of nitrate absorbance shifts to higher wavelengths with increasing nitrate concentration. This chemometric approach is described in detail in [19]. The use of complex statistical analysis programmes has allowed the development of a sensing system which can process raw untreated samples directly. This has the advantages of removing the need for chemical reagents or sample pre-treatment to remove interferences and achieving a robust and compact portable system.

Initial data analysis was carried out using Principal Component Analysis (PCA) to determine relationships between variables and to indicate how the data groups by parameter, in this case nitrate concentration. A plot of the scores of principal component 1, PC 1 versus PC 2 is used to identify patterns within the data. A theoretical calculation was used to indicate potential outliers within the data. The outliers can thus be identified and removed from the model to improve prediction accuracy.

Having examined these data using PCA, the next step was to generate a partial least squares (PLS) model. Initially, four independent data sets in which the nitrate concentration was randomly varied from 1-100ppm nitrate were examined. The regression model was initially validated using the data that it was created from. In this case the concentration values were predicted and plotted against the known or measured values. The regression model produces a regression coefficient for each x-variable used. In this case, the x-variables correspond to absorbance values recorded at each specific wavelength. The wavelength range selected for this regression model was from 205nm to 250nm as this encompassed the region of interest where most variation in absorbance occurs due to nitrate. The wavelength region below 205nm was found to be too noisy to be useful for modelling and above 250nm displayed very little response to nitrates. These regression coefficients can now be used to predict concentrations from unknown or blind samples. This prediction can be carried out

internally in the software or in any device capable of basic data processing by the use of an exported model.

The generation of a robust model for use in real applications requires consideration of the effects of interfering substances, in particular humic acid and chloride. A comprehensive calibration model was generated using known dosing of interferences, which would be capable of operating with or without interference elements present. A series of samples with varying concentrations of nitrate and varying amounts of humic acid were examined. The method chosen to model the nitrate response in the presence of the interference element was second order PLS or PLS2 regression. Using this algorithm two or more responses can be modelled simultaneously, in this case the effect of varying nitrate concentration and the variation in amount of humic acid added.

The initial optical sensor prototype calibration has been carried out using clean solutions of known nitrate concentrations. PCA and subsequent influence plots identified outliers that could then be discarded to achieve a more robust calibration algorithm. An influence plot based on a PCA analysis of nitrate data is shown in Figure 2.12. This plot highlights that for clean nitrate solutions the 100ppm nitrate values are distinctly separate from the rest of the samples although the values of residual variance and influence for these samples are still relatively low. A small number of 50ppm nitrate data points also show marginally higher residual variance as compared to the majority of the samples.

An initial prediction was carried out for independent data sets of clean nitrate solutions randomly varied from 1-100ppm. The results of this prediction using PLS regression model on a set of blind nitrate samples is shown in Figure 2.13. The estimated deviation in prediction is shown as error bars and the resulting data points are fitted with a linear fit through the origin to indicate the performance of the model. Having previously discarded some higher concentration solutions through the analysis process, this graph indicates a good fit over the nitrate concentration range of 0-100ppm.

The effect of interferences on the detection of nitrate was then incorporated into the chemometric model. The scores for a PLS2 regression generated from nitrate samples of varying concentrations contaminated with humic acid in varying amounts is shown in Figure 2.14. The PLS2 model validation shows very good linearity with a small offset and a very good correlation coefficient.

Further solutions contaminated with humic acid were then used to add to the

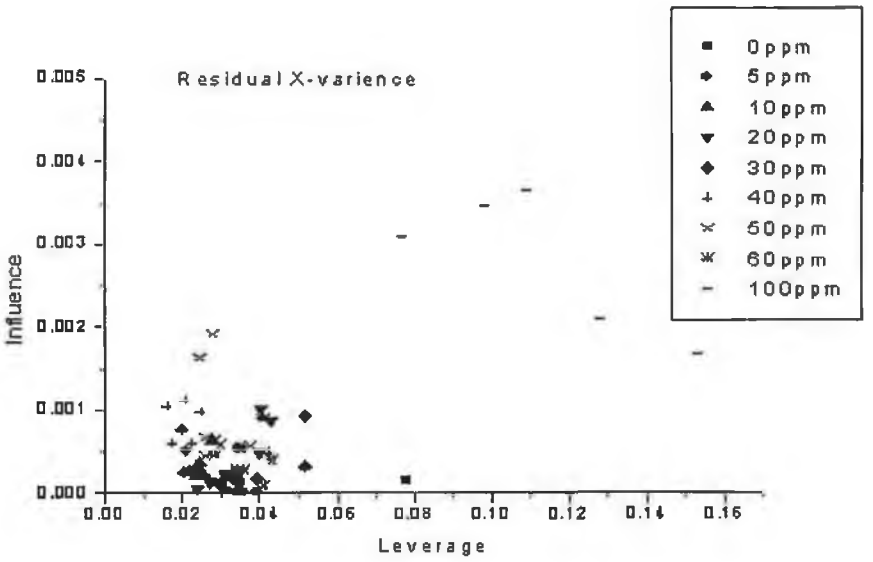

Figure 2.12: . Influence plot for PCA on nitrate absorption showing samples that exhibit high residual variance or high leverage.

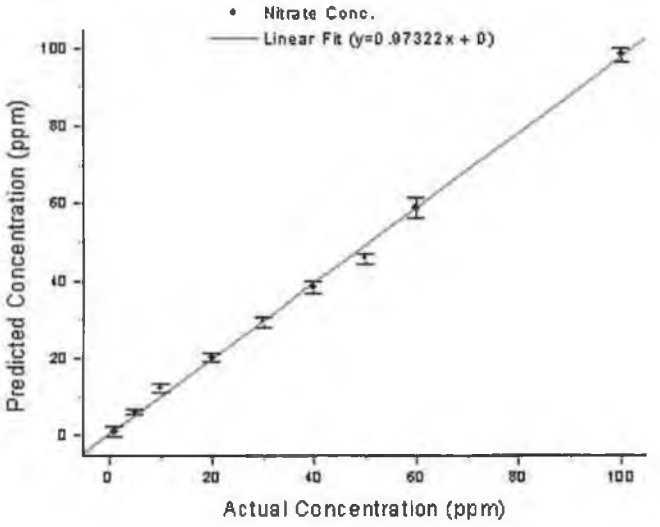

Figure 2.13: Prediction of nitrate concentration on a set of blind samples using a regression model created using data from 4 independent nitrate runs.

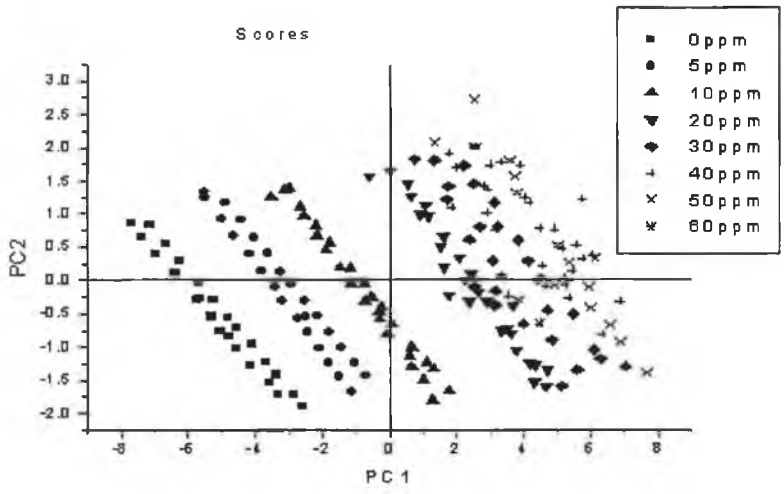

Figure 2.14: Scores plot for PLS2 regression of sodium nitrate with humic acid interference.

data set and the model was used to predict the concentration of nitrate present in samples from independent 'blind' runs with varying degrees of humic acid contamination. The resultant predictions are shown in Figure 2.15. The combination of nitrate and humic acid absorption reduces the signal to a lower level with the present prototype design and path length. As a consequence, the higher concentration nitrate solutions are not very well fitted by this model due to a saturation effect which is augmented by the presence of the strongly absorbing humic acid.

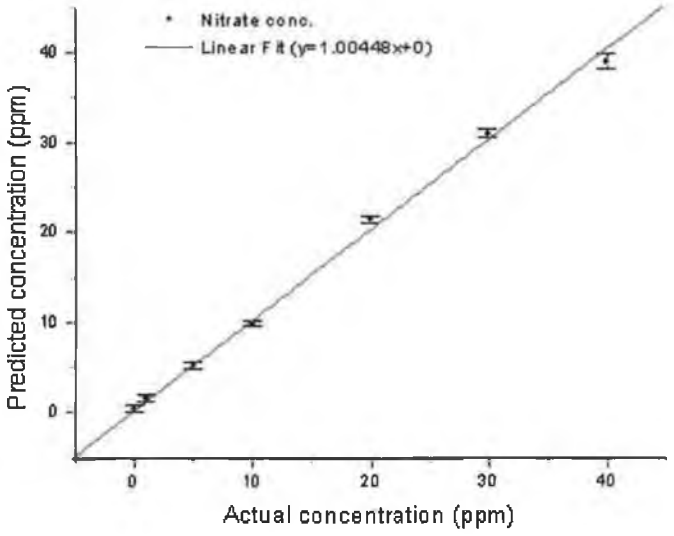

Figure 2.15: Plot of predicted nitrate concentration against actual concentration for 3ppm humic acid contamination.

This problem can be addressed by decreasing the path length in the sensor-probe-head to achieve a greater range as required.

2.6 Conclusion

A nitrate sensor has been developed based on UV-spectrophotometry. This enables a direct measurement of nitrate concentration without the use of reagents, moving parts, separation steps or the production or use of any potentially harmful compounds. State-of-the-art optical instrumentation such as spectrometers, optical fibres and light sources have been evaluated and used to develop a robust portable prototype for continuous, in-situ sensing of nitrate concentration in water. The dependence of absorption on nitrate concentration was established and the effect of key interferences has been investigated. In clean or pre-treated water samples the sensor working range is from 0-100ppm nitrate. Chemometric modelling software tools have been employed to produce calibration data for nitrate concentrations between 0 and 40ppm nitrate allowing for interferences. The PLS2 regression, generated using samples with varying nitrate concentrations some of which were contaminated and some of which were clean, provides a system fully capable of dealing with realistic samples and providing accurate predictions of nitrate concentration. In its current state the prototype achieves reliable detection of nitrate up to 40ppm nitrate in the presence of representative contaminants with a limit of detection of 1ppm nitrate. This is an improvement on the dynamic range reported for previous multivariate analysis methods [16]. The effect of chloride was found to be insignificant with the concentration of chloride in locally found groundwater samples. The regression model is exportable to allow the model to be integrated with a measurement system for instantaneous calculation of nitrate concentration. The working range of the sensor can be further extended by altering the path length in the optical probe head to prevent saturation of the detector. It was then chosen to further develop optical sensors based on fluorescence rather than absorbance properties of materials, as outlined in Chapter 1, and the remainder of this thesis deals with a fluorescence-based sensor platform.

Bibliography

[1] C. K. Chow and C. B. Hong. Dietary vitamin E and selenium and toxicity of nitrite and nitrate. *Toxicology*, 180(2):195–207, 2002.

[2] R.H. Liu and J.H. Hotchkiss. Potential genotoxicity of chronically elevated nitric oxide: A review. *Mutation Research/Reviews in Genetic Toxicology*, 339(2):73–89, 1995.

[3] Environmental Protection Agency Ireland. Parameters of water quality. Technical report, 2001.

[4] P. Mikuska and Z. Vecera. Simultaneous determination of nitrite and nitrate in water by chemiluminescent flow-injection analysis. *Analytica Chimica Acta*, 495(1-2):225–232, 2003.

[5] Z. Legnerova, P. Solich, H. Sklenarova, D. Satinsky, and R. Karlicek. Automated simultaneous monitoring of nitrate and nitrite in surface water by sequential injection analysis. *Water Research*, 36(11):2777–2783, 2002.

[6] M. A. Stanley, J. Maxwell, M. Forrestal, A. P. Doherty, B. D. MacCraith, D. Diamond, and J. G. Vos. Comparison of the analytical capabilities of an amperometric and an optical sensor for the determination of nitrate in river and well water. *Analytica Chimica Acta*, 299(1):81–90, 1994.

[7] S. J. Cho, S. Sasaki, K. Ikebukuro, and I. Karube. A fluorescent nitrate sensing system using a reaction cartridge and titanium trichloride. *Talanta*, 54(5):903–911, 2001.

[8] S. J. Cho, S. Sasaki, K. Ikebukuro, and I. Karube. A simple nitrate sensor system using titanium trichloride and an ammonium electrode. *Sensors and Actuators B: Chemical*, 85(1-2):120–125, 2002.

[9] D. Kirstein, L. Kirstein, F. Scheller, H. Borcherding, J. Ronnenberg, S. Diekmann, and P. Steinrucke. Amperometric nitrate biosensors on the basis of pseudomonas stutzeri nitrate reductase. *Journal of Electroanalytical Chemistry*, 474(1):43–51, 1999.

[10] L. H. Larsen, L. R. Damgaard, T. Kjaer, T. Stenstrom, A. Lynggaard-Jensen, and N. P. Revsbech. Fast responding biosensor for on-line determination of nitrate/nitrite in activated sludge. *Water Research*, 34(9):2463–2468, 2000.

[11] C. J. Taylor, L. A. Bain, D. J. Richardson, S. Spiro, and D. A. Russell. Construction of a whole-cell gene reporter for the fluorescent bioassay of nitrate. *Analytical Biochemistry*, 328(1):60–66, 2004.

[12] G. J. Mohr and O. S. Wolfbeis. Effects of the polymer matrix on an optical nitrate sensor based on a polarity-sensitive dye. *Sensors and Actuators B: Chemical*, 37(1-2):103–109, 1996.

[13] G. J. Mohr, I. Murkovic, F. Lehmann, C. Haider, and O. S. Wolfbeis. Application of potential-sensitive fluorescent dyes in anion- and cation-sensitive polymer membranes. *Sensors and Actuators B: Chemical*, 39(1-3):239–245, 1997.

[14] C. Huber, I. Klimant, C. Krause, T. Werner, and O. S. Wolfbeis. Nitrate-selective optical sensor applying a lipophilic fluorescent potential-sensitive dye. *Analytica Chimica Acta*, 449(1-2):81–93, 2001.

[15] R. C. Hoather and R. F. Rackham. Oxidised nitrogen in waters and sewage effluents observed by ultra-violet spectrophotometry. *Analyst*, 84(1002):548–551, 1959.

[16] M. Karlsson, B. Karlberg, and R.J.O. Olsson. Determination of nitrate in municipal waste water by UV spectroscopy. *Analytica Chimica Acta*, 312(1):107–113, 1995.

[17] J. Gallardo, S. Alegret, and M. del Valle. A flow-injection electronic tongue based on potentiometric sensors for the determination of nitrate in the presence of chloride. *Sensors and Actuators B: Chemical*, 101(1-2):72–80, 2004.

[18] B.J. Clark, T. Frost, and M.A. Russell. *UV Spectroscopy, techniques, instrumentation, data handling*. Chapman & Hall, London, 1993.

[19] C. Gibson, P. Byrne, O. McGaughey, H. Masterson, C. Haslinger, K. O'Dwyer, and B. D. MacCraith. Development of a robust nitrate sensor for water quality monitoring. *Paper in preparation.*

[20] T McNally. Central Water Testing Laboratory, Dublin Corporation, Dublin, Personal communication, 2002.

[21] Dublin Corporation. Roundwood, Ballyboden and Ballymore Eustace water quality data. Technical report, 2002.

Chapter 3

The Sol-Gel Process

3.1 Introduction

Sol-gel processing methods are now being widely used since they provide a versatile method for fabricating glass at low temperatures [1–3]. Sol-gel is a material fabrication technique that forms glass and ceramic structures from metal alkoxide precursors. In 1846, Ebelman first prepared a metal alkoxide solution from $SiCl_4$ and alcohol and this was found to gel on exposure to the atmosphere [3]. The main limiting factor on the use of sol-gel processing at this time was that drying took in order of 1 year or more which negated the usefulness of this process. The main problem to be overcome was cracking during drying due to the large amount of shrinkage which takes place. This problem is not as prevalent with small area coatings and can also be controlled with careful control of the chemical process. This leads to much shorter drying times making sol-gel processing an attractive method of glass and ceramic production.

Sol-gel processing to fabricate glasses can be performed at approximately 100°C, which is an order of magnitude less than other glass fabrication procedures (~1000°C). This makes sol-gel a less expensive method to produce glass and the low temperature means compounds, in the case of this work fluorescent dyes, which could not withstand the high temperature of the glass production process can be immobilised in the glass. The optical transparency of the sol-gels is also an advantage as this enables them to be used as optical sensors.

Another advantage of the sol-gel process exploited in this work is the ability to coat a wide range of substrates with a large range of different geometries with the sol and then cure the sol in position. This enables the sol to be deposited

using a wide range of thin film deposition techniques, as described in Section 7.5, on a range of sensor platforms such as silicon, PMMA and planar glass substrates (as shown in Chapter 7). The sol-gel process was used in this work as a method of providing an immobilisation matrix for a range of fluorescent dyes for sensing applications and to develop a sensor platform using UV-curable sol-gel materials and a range of photolithographic and soft-lithographic techniques.

This chapter details the various stages in the sol-gel process and the main factors which influence the process. One of the advantages of sol-gel is the ability to tailor the sol-gel films properties to suit the application and methods of doing this will be described. The application of the sol-gel process in the course of this work as both a sensor platform and as a sensor immobilisation matrix will be detailed.

3.2 Sol-gel Processing

Before describing the sol-gel process, the various parts of a sol-gel will first be defined. A colloid is a solid particle with diameters of 1-100nm. A sol consists of a colloidal suspension of particles in a liquid. A gel is an interconnected, rigid network with pores of submicrometer dimensions and polymeric chains whose average length is greater than a micron [3]. The sol-gel process is a process for making glass and ceramic materials. The sol-gel process involves the transition of a system from a liquid ("sol") into a solid ("gel") phase.

There are three methods used for making sol-gels [3]:

1. Gelation of a solution of colloidal powder
2. Hydrolysis and polycondensation of alkoxide or nitrate precursors followed by hypercritical drying of gels
3. Hydrolysis and polycondensation of alkoxide followed by aging and drying of gels under near ambient atmospheres

The third method is the most commonly used and is used in the case of this work. The most common silicon precursor used is tetraethoxysilane (TEOS), which is a silicon alkoxide which consists of a silicon atom surrounded by four ethoxy groups. This has been used in the work presented here along with a range of other precursors as shown in Table 3.1. Most of the other precursors used are organoalkoxysilanes - where the central metal atom is again surrounded by four ligands but this time at

least one is an organic group. In this case, the bonds are direct metal-carbon bonds as opposed to metal-oxygen-carbon bonds that are present in silicon alkoxides.

	Chemical Formula	Chemical Name
TEOS	$Si(OC_2H_5)_4$	Tetraethoxysilane
MTEOS	$CH_3Si(OC_2H_5)_3$	Methyltriethoxysilane
ETEOS	$C_2H_5Si(OC_2H_5)_3$	Ethyltriethoxysilane
PTEOS	$CH_3CH_2CH_2Si(OC_2H_5)_3$	Propyltriethoxysilane
TMOS	$Si(OCH_3)_4$	Tetramethoxysilane
MAPTMS	$CH_2CCH_3CO_2(CH_2)_3Si(OCH_3)_3$	Methacryloxypropyl -trimethoxysilane

Table 3.1: Sol-gel precursors.

In general, the sol-gel process consists of the formation of an interconnected 3-D network by the simultaneous hydrolysis and condensation of an organometallic precursor. The gel is termed a xerogel when the pore liquid has been removed at approximately ambient pressure by thermal evaporation (drying) and shrinkage occurs. A gel is defined as dried when the physically adsorbed water is completely evacuated. The process of treating a gel at elevated temperatures, which substantially reduces the number of pores, is called densification. A dense glass is obtained when all the pores in the gel are removed. In the case of this work, the xerogel is the material of interest as its porous nature is exploited for use in optical sensing. A fully densified gel would not be suitable for sensing as the analyte could not enter the matrix.

3.2.1 Outline of the process

A sol-gel material is fabricated by mixing a precursor, as described in Section 3.2, catalyst, water and a suitable solvent. This allows hydrolysis and condensation reactions to proceed and a gel is formed. A series of thermal treatments can then be undertaken to control the densification of the gel. An outline of the process is shown in Figure 3.1. The sol-gel process lends itself to film fabrication - at the stage where a liquid sol has been created, a thin glass film can be formed by a range of deposition techniques. After using a relatively low temperature treatment, porous xerogel films are formed and are the basis of the sensors used in this work.

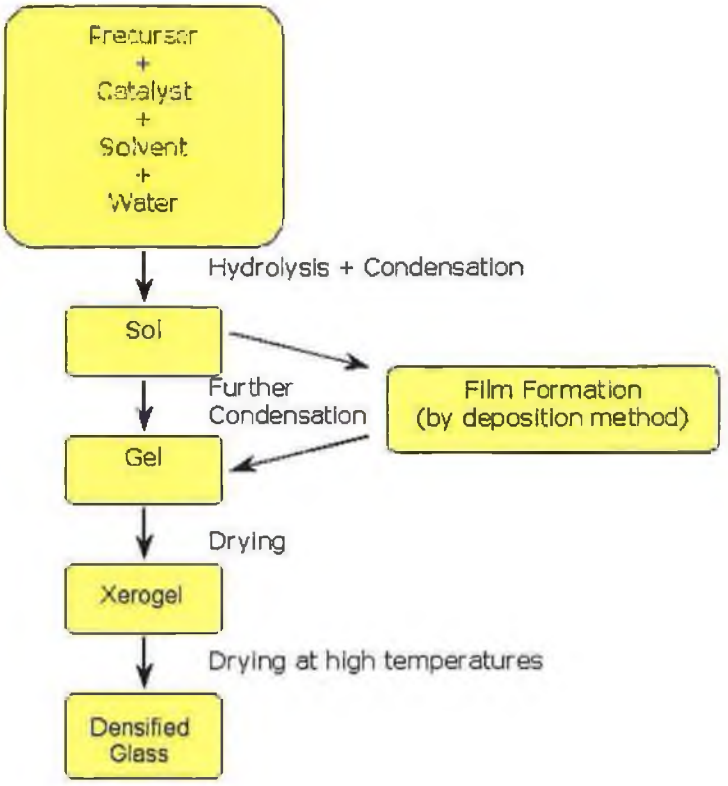

Figure 3.1: Outline of the sol-gel process [4].

3.2.2 Hydrolysis and condensation

As mentioned in Section 3.2.1, when the components of a sol-gel are mixed together hydrolysis and condensation reactions begin to occur. Hydrolysis is the reaction which replaces alkoxide groups (OR) with hydroxyl groups (OH) by the nucleophilic attack on silicon atoms by oxygen [2], forming the hydrolysed molecule and alcohol as shown in Equation 3.1 where R represents an alkyl group (C_xH_{2x+1}). Depending on the actual reaction conditions condensation may begin before hydrolysis is complete [5]. Both alcohol (Equation 3.2) and water (Equation 3.3) condensation reactions of the silanol groups occur by a nucleophilic condensation reaction and produce siloxane bonds, $\equiv$ Si – O – Si $\equiv$, and the by-products of the reactions are either alcohol or water respectively.

$$\equiv Si - OR + H_2O \Leftrightarrow \equiv Si - OH + ROH \tag{3.1}$$

$$\equiv Si - OR + HO - Si \equiv \Leftrightarrow \equiv Si - O - Si \equiv + ROH \tag{3.2}$$

$$\equiv Si - OH + HO - Si \equiv \Leftrightarrow \equiv Si - O - Si \equiv + H_2O \tag{3.3}$$

As water and alkoxysilanes are immiscible, a mutual solvent such as alcohol is used as a homogenising agent. It is important to note that the alcohol can also participate in the reverse reactions shown in Equations 3.1 and 3.2. The siloxane bonds link together, as the condensation reactions occur, to build a polymeric chain which interlink to form a 3-D network or a gel. The gel is formed when the polymeric chain can support a stress elastically [3]. The time to reach this stage (the gel point) is typically known as the gelation time, t_{gel}. The rates of hydrolysis and condensation are very dependent on process parameters such as sol pH and molar ratio of water to precursor as well as processing temperature and drying conditions. These factors in turn influence film properties such as thickness, porosity and refractive index which are very relevant for optical sensor applications [6]. The influence of a number of process parameters on sol-gel film properties are described in Section 3.2.3 and 3.3.

3.2.3 Aging and drying

When the gel, that has been formed by a series of hydrolysis and condensation reactions, remains in its pore liquid, its properties continue to evolve even after it has reached the gel point. This process is known as aging. In some cases, it is preferable to age the sol prior to coating to either increase the film viscosity or to alter the porosity of the sol. If the sol is not viscous enough the coating procedure may not be successful [5]. Altering the pore size of the gel can influence the sensitivity of the sensor [6]. Aging can be carried out in either ambient conditions or at elevated temperatures.

Drying is the removal of liquid from the interconnected pore network. Drying can be divided into three distinct stages. During the first stage of drying, known as the constant rate period, the decrease in the volume of the gel is equal to the volume of the liquid lost by evaporation and the rate of evaporation per unit area of drying is independent of time. The gel network is deformed by the large capillary forces, which causes shrinkage of the object. Stage 1 continues until the critical point - the density of the gel network increases and it strengthens sufficiently to

resist shrinkage - is reached. The second stage, the first falling rate period, occurs by flow through the surface films that cover partially empty pores , the liquid flows to the surface where evaporation takes place, the flow is driven by the gradient in capillary pressure. The final stage - the second falling rate period - then occurs and the liquid can now only escape through the diffusion of its vapour to the surface. During the course of the work undertaken in this project drying of all gels normally occurred at <100°C (typically 70 °C for sensor matrices) and the gel formed a xerogel.

3.3 Factors Affecting the Sol-gel Process

3.3.1 Influence of water to precursor ratio - R value

The R value of a sol is the molar ratio of water to precursor solution, (H_2O:Precursor), and this plays a large role in the structural evolution of sol-gel materials. This is due to the the fact that the hydrolysis and condensation (Equations 3.1–3.3) which govern the sol-gel process depend on water. In theory, R=2 is sufficient for complete hydrolysis and condensation to yield anhydrous silica as shown by the net reaction described in Equation 3.4 [2].

$$nSi(OR)_4 + 2nH_2O \rightarrow nSiO_2 + 4nROH \tag{3.4}$$

This R value has been shown not to be sufficient for complete hydrolysis and condensation to occur due to the formation of intermediate species and reverse reactions taking place. A higher R value is thus used in general to ensure that the hydrolysis and condensation reactions go to completion. As the R value is increased, the extra water ensures faster hydrolysis. When the R value is increased to a point where the extra water is in excess in the hydrolysis reaction, this water starts to dilute the sol and reduce the relative silica content which results in longer gel times and thinner films. The effect of increasing the R value on the gel time is shown in Figure 3.2. The conditions under which the sol is prepared, particularly the sol pH, influence the position of the minimum of the curve.

It can clearly be seen that sol viscosity, film thickness and other film properties are highly dependent on the R value and the sol pH which effect the hydrolysis and condensation process [5].

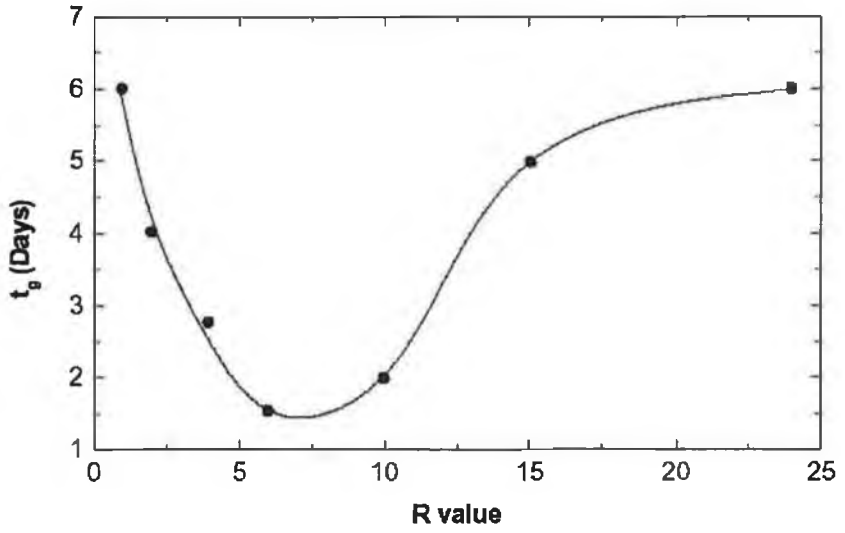

Figure 3.2: Influence of R value on gel time [2].

3.3.2 Influence of sol pH

The pH of a silica-based sol-gel material is defined with respect to the isoelectric point of silica. This is the point at which the electron mobility and surface charge are zero and occurs at pH≈2. Below this point (pH<2) acid catalysis - which is characterised by fast hydrolysis and relatively long gel times - occurs. Above this point (pH>2) base catalysis - which is characterised by slow hydrolysis and a fast condensation rate which gives shorter gel times - occurs. This means that sols made under acid catalyis conditions are generally weakly branched structures with small pores whereas those made under base catalysis conditions form a particulate gel with larger pores [1]. It can clearly be seen that by altering the sol pH the microstructure of the resultant sol can be tailored. Figure 3.3 shows how the condensation rate [Condensation Rate = (1/gel time)] is influenced by the sol pH.

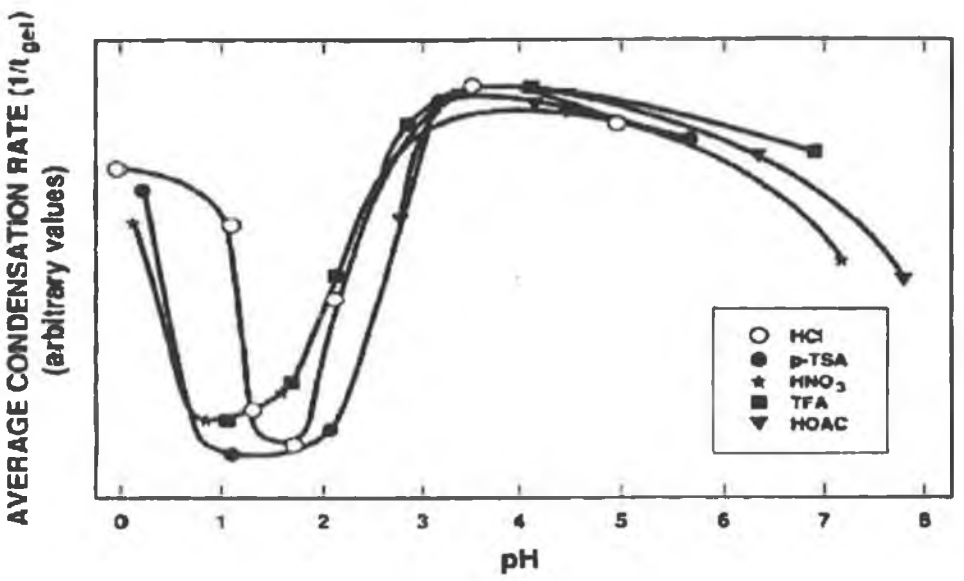

Figure 3.3: Influence of sol pH on the condensation rate [2].

3.3.3 Influence of solvent

As mentioned in Section 3.2.2, a solvent is used in the sol-gel process as water and the alkoxysilane precursor solutions are immiscible. This gives rise to a more homogenous sol. Solvents play a role in both the hydrolysis and condensation reactions. Solvents can be either polar or non polar and this polarity can influence the rate of hydrolysis by effecting the catalysis. For example, the polar solvent ethanol (EtOH), used in the many of the sol-gels developed in this work, can reduce the catalysis in acid catalysed materials due to solvent bonding to hydronium ions in the sol [2]. Solvents can also dilute the sol which reduces the precursor concentration and decreases the reaction rates thus increasing the gel time. This process is shown, in Figure 3.4 for a sol containing different ratios of ethanol and TEOS over a range of R values. The gel time increases with increasing ethanol content.

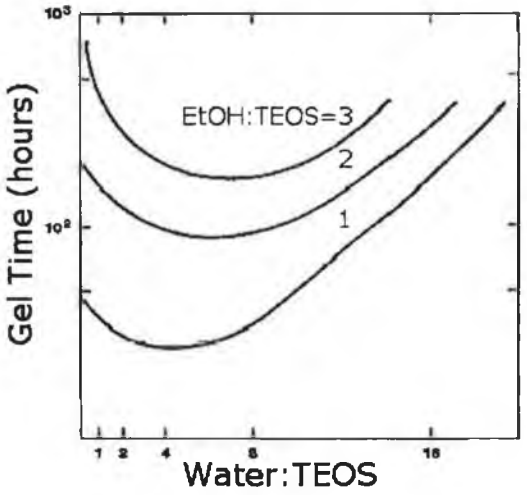

Figure 3.4: Gel time versus H_2O:TEOS ratio, R, for three ratios of EtOH to TEOS [2].

3.4 Ormosils

The surface of a standard TEOS or TMOS-based gel or film is covered with hydroxyl groups and is highly hydrophilic. This allows the absorption of a layer of water molecules. For some applications, such as dissolved oxygen sensing [7] and carbon dioxide sensing [8], a more hydrophobic surface is required. There are two main methods of removing the surface hydroxyl groups: thermal dehydration and chemical modification. Thermal dehydration is not used in the development of sensor films as it involves densification of the films and removal of the pores which facilitate the sensor chemistry. Chemical modification is used in this work by using a combination of organic and inorganic precursor materials. The modified materials are known as ORMOSILS (*OR*ganically *MO*dified *SIL*icates) [9]. Ormosils have at least one organic group replacing the ethoxy groups surrounding the central metal ion. These precursors replace one of the surface hydroxyl group with an alkyl group giving rise to a hydrophobic surface. Ormosils have the general form R'Si$(OR)_3$ where OR is the standard alkoxy group and R' is the organic ligand which has replaced an alkoxy group. A typical example of an organically modified silicon precursor is methyltriethoxysilane (MTEOS, $CH_3Si(OC_2H_5)_3$) where the alkoxy group is replaced by an organic ligand. It can also be shown that as the aliphatic group of the modified precursor gets larger - for example, MTEOS (CH_3) to ETEOS (C_2H_5)

- this further enhances the hydrophobicity of the film [10].

Advantages other than hydrophobicity can be obtained when using ormosils. It has been shown that using a combination of TEOS and an organically modified alkoxide precursor as a dye immobilisation matrix reduces the leaching of the dye from the matrix and also improves the film stability [11]. As there is the possibility of using any organic moiety, tuning of a range of properties such as thermal stability, refractive index and pore size is also achievable. Thicker coatings can be obtained, without cracking, by adding ormosils - a higher content of ormosils increase the thickness of the film [12]. The addition of organic groups exert an influence on the structure of the gel: it reduces the network connectivity of the gel allowing a better densification without cracking of the gel when drying. The ability to control the pore size leads to an ability to control the sensitivity of a sensor dye encapsulated in a sol-gel matrix [6]. Furthermore, an increase in the pore size leads to a shorter response time of the sensor [1].

3.5 Encapsulation of Molecules within the Sol-gel Matrix

As mentioned in Section 3.2.1, one of the advantages of using the sol-gel is the low-temperature required for the process. This enables the encapsulation of materials, which would be unable to withstand other high-temperature processes, in a sol-gel matrix. This ability of sol-gel to provide a suitable matrix for fluorescent dyes has led to the production of a large number of optical sensors for different analytes such as oxygen and dissolved oxygen [7, 13–15], carbon dioxide and dissolved carbon dioxide [8, 16, 17], relative humidity [18, 19], pH [20, 21], ammonia [22, 23] and nitrite [24] which have all been developed in this laboratory. They can also be used to entrap proteins and enzymes for biosensors [25]

All of these sensors employ the use of a sol-gel matrix to entrap a fluorescent dye. Due to the porous structure of the sol-gel matrix, the analyte to be sensed can travel through the interconnected pores of the matrix and react with the fluorescent dye while the dye is maintained within the matrix. The pore size of the sol-gel matrix can be tailored to aid dye entrapment as described in Section 3.2 and 3.3. The sol-gel matrix is optically transparent which allows its use as an optical sensor. The fluorescent dye can be excited and the fluorescent emission collected through the

matrix. Sol-gel films with a fluorescent dye entrapped are known as doped sol-gel films.

3.6 Photocurable Sol-gels

Photocurable sol-gel materials can be used in the fabrication of optical components [26–28]. These materials are photocurable due to the presence of photopolymerisable organic functionalities. When exposed to light of a suitable wavelength, usually in the UV-region, the exposed part becomes densified. Materials in non-exposed areas are soluble in a wide range of standard solvents found in all laboratories (e.g. isopropanol) and can be removed easily. This photocurable property enables the writing of particular structures, such as ridge waveguides [15], with the use of a particular mask and standard photolithographic technique. This extends the amount of materials that can be used for photolithography from the range of standard photoresists.

These photocurable sol-gel materials are used to fabricate waveguide structures as will be described in detail in Section 7.3. The sol is prepared using a combination of the silicon alkoxide precursor (TEOS) and a second precursor (MAPTMS) which contains an acrylate part. A photoinitiator is added to the sol at the end of the synthesis to make the sol photosensitive and its refractive index was modified to enable waveguiding as described in Section 3.7

3.7 Refractive Index Modification

In the case of optical sensing, it is necessary for the sol-gel layer to have a lower refractive index than the substrate supporting it to ensure preferential coupling of fluorescence into the substrate as will be described in Chapter 6. In the course of this work, ridge waveguides have been fabricated using UV-curable sol-gels. For efficient waveguiding, the guiding layer must have a higher refractive index than the layer directly beneath it, in this case the buffer layer, for total internal reflection and waveguiding to occur. This will be discussed in more detail in Chapter 4. Due to these facts, the tailoring of refractive index is a key part of sol-gel film fabrication.

Atkins et al have altered the refractive index of a sol-gel film by using a combination of ormosils along with the standard TEOS precursor solution [29]. By

varying the ratio of the ormosils (PhTEOS and MTEOS) the refractive index of the film changes while the % organic component remains the same. This refractive index change is independent of pH. The film properties such as film thickness, hydrophobicity, gel time, and cracking during drying depend on the relative ratio of ormosils.

Another method of refractive index modification, and the method used in the work undertaken in this project, involves the use of higher refractive index metal alkoxide precursors along with the standard precursors (TEOS) in the sol preparation. Previous work in this area has used both zirconia (ZrO_2) and titania (TiO_2) precursors. Titania has been used in the fabrication of planar sol-gel waveguides [22,30]. A major consideration in the use of these higher refractive index metal alkoxide precursors is to ensure that the hydrolysis rates for all parts of the sol are similar to ensure a homogenous gel is formed. These metal alkoxide precursors have a different hydrolysis rate to the silica precursors. In the case of titania, to address this problem a choice of a suitable catalyst (e.g. $SiCl_4$) is required for the hydrolysis of the precursors to proceed at a similar rate. In the work undertaken in this laboratory, zirconia is used as a refractive index modifier [15,31]. A complexing agent was used with zirconia to ensure a homogenous gel was produced. This is described in more detail in Section 7.3. The ratio of precursors used can determine the final refractive index of the film thus making it possible to fabricate waveguide layers with different refractive indices using the sol-gel process.

3.8 Conclusion

The sol-gel process for fabrication of glass-like structures at relatively low temperatures has been explained in detail in this chapter. The method to fabricate these structures from the hydrolysis and condensation of a range of precursor solutions has been discussed. It has been shown that one of the main advantages of using sol-gel processing is the ability to alter the process in a range of ways - by changing factors such as precursor type, aging, drying, solvent type, pH and R value - which give the ability to tailor the sol-gel film for a particular application. The use of sol-gel materials as immobilisation matrices for fluorescent dyes and its relevance to optical sensing has been described. Sol-gel materials were also used in the fabrication of waveguide structures.

Bibliography

[1] B. D. MacCraith and C. McDonagh. Enhanced fluorescence sensing using sol-gel materials. *Journal of Fluorescence*, 12(3-4):333–342, 2002.

[2] C.J. Brinker and G.W. Scherer. *Sol-gel science : the physics and chemistry of sol-gel processing.* Academic Press, New York, 1990.

[3] L. L. Hench and J. K. West. The sol-gel process. *Chemical Reviews*, 90(1):33–72, 1990.

[4] A.K. McEvoy. *Development of an optical sol-gel-based dissolved oxygen sensor.* Ph.D. Thesis, Dublin City University, 1996.

[5] C. McDonagh, F. Sheridan, T. Butler, and B. D. MacCraith. Characterisation of sol-gel-derived silica films. *Journal of Non-Crystalline Solids*, 194(1-2):72–77, 1996.

[6] C. McDonagh, P. Bowe, K. Mongey, and B. D. MacCraith. Characterisation of porosity and sensor response times of sol- gel-derived thin films for oxygen sensor applications. *Journal of Non-Crystalline Solids*, 306(2):138–148, 2002.

[7] A. K. McEvoy, C. M. McDonagh, and B. D. MacCraith. Dissolved oxygen sensor based on fluorescence quenching of oxygen-sensitive ruthenium complexes immobilized in sol-gel- derived porous silica coatings. *Analyst*, 121(6):785–788, 1996.

[8] C. von Bültzingslöwen, A. K. McEvoy, C. McDonagh, B. D. MacCraith, I. Klimant, C. Krause, and O. S. Wolfbeis. Sol-gel based optical carbon dioxide sensor employing dual luminophore referencing for application in food packaging technology. *Analyst*, 127(11):1478–1483, 2002.

[9] H. Schmidt. Organic modification of glass structure - new glasses or new polymers. *Journal of Non-Crystalline Solids*, 112(1-3):419–423, 1989.

[10] C. McDonagh, B. D. MacCraith, and A. K. McEvoy. Tailoring of sol-gel films for optical sensing of oxygen in gas and aqueous phase. *Analytical Chemistry*, 70(1):45–50, 1998.

[11] R. Makote and M. M. Collinson. Organically modified silicate films for stable pH sensors. *Analytica Chimica Acta*, 394(2-3):195–200, 1999.

[12] P. Innocenzi, M.O. Abdirashid, and M. Guglielmi. Structure and properties of sol-gel coatings from methyltriethoxysilane and tetraethoxysilane. *Journal of Sol-Gel Science and Technology*, 3:47–55, 1994.

[13] A. K. McEvoy, C. McDonagh, and B. D. MacCraith. Optimisation of sol-gel-derived silica films for optical oxygen sensing. *Journal of Sol-Gel Science and Technology*, 8(1-3):1121–1125, 1997.

[14] C. McDonagh, C. Kolle, A. K. McEvoy, D. L. Dowling, A. A. Cafolla, S. J. Cullen, and B. D. MacCraith. Phase fluorometric dissolved oxygen sensor. *Sensors and Actuators B: Chemical*, 74(1-3):124–130, 2001.

[15] C. S. Burke, O. McGaughey, J. M. Sabattié, H. Barry, A. K. McEvoy, C. McDonagh, and B. D. MacCraith. Development of an integrated optic oxygen sensor using a novel, generic platform. *Analyst*, 130(1):41–45, 2005.

[16] C. von Bültzingslöwen, A. K. McEvoy, C. McDonagh, and B. D. MacCraith. Lifetime-based optical sensor for high-level pCO_2 detection employing fluorescence resonance energy transfer. *Analytica Chimica Acta*, 480(2):275–283, 2003.

[17] C.S. Burke, A. Markey, R.I. Nooney, P. Byrne, and C. McDonagh. Development of an optical sensor probe for the detection of dissolved carbon dioxide. *Sensors and Actuators B: Chemical*, page In Press, 2006.

[18] O. McGaughey, J.V. Ros-Lis, A. Guckian, A.K. McEvoy, C. McDonagh, and B. D. MacCraith. Development of a fluorescence lifetime-based sol-gel humidity sensor. *Analytica Chimica Acta*, 570:15–20, 2006.

[19] O. McGaughey, R. Nooney, A.K. McEvoy, C. McDonagh, and B.D. MacCraith. Development of a multi-analyte integrated optical sensor platform for indoor air-quality monitoring. *Proc. SPIE*, 5993:172–183, 2005.

[20] C. Malins, H. G. Glever, T. E. Keyes, J. G. Vos, W. J. Dressick, and B. D. MacCraith. Sol-gel immobilised ruthenium(II) polypyridyl complexes as chemical transducers for optical ph sensing. *Sensors and Actuators B: Chemical*, 67(1-2):89–95, 2000.

[21] T. M. Butler, B. D. MacCraith, and C. McDonagh. Leaching in sol-gel-derived silica films for optical pH sensing. *Journal of Non-Crystalline Solids*, 224(3):249–258, 1998.

[22] C. Malins, A. Doyle, B. D. MacCraith, F. Kvasnik, M. Landl, P. Simon, L. Kalvoda, R. Lukas, K. Pufler, and I. Babusik. Personal ammonia sensor for industrial environments. *Journal of Environmental Monitoring*, 1(5):417–422, 1999.

[23] C. S. Burke, L. Polerecky, and B. D. MacCraith. Design and fabrication of enhanced polymer waveguide platforms for absorption-based optical chemical sensors. *Measurement Science & Technology*, 15(6):1140–1145, 2004.

[24] S. Ferretti, S. K. Lee, B. D. MacCraith, A. G. Oliva, D. J. Richardson, D. A. Russell, K. E. Sapsford, and M. Vidal. Optical biosensing of nitrite ions using cytochrome cd(1) nitrite reductase encapsulated in a sol-gel matrix. *Analyst*, 125(11):1993–1999, 2000.

[25] B. C. Dave, B. Dunn, J. S. Valentine, and J. I. Zink. Sol-gel encapsulation methods for biosensors. *Analytical Chemistry*, 66(22):A1120–A1127, 1994.

[26] S. Aubonnet, H. F. Barry, C. von Bültzingslöwen, J. M. Sabattié, and B. D. MacCraith. Photo-patternable optical chemical sensors based on hybrid sol-gel materials. *Electronics Letters*, 39(12):913–914, 2003.

[27] S. I. Najafi, T. Touam, R. Sara, M. P. Andrews, and M. A. Fardad. Sol-gel glass waveguide and grating on silicon. *Journal of Lightwave Technology*, 16(9):1640–1646, 1998.

[28] P. Coudray, P. Etienne, Y. Moreau, J. Porque, and S. I. Najafi. Sol-gel channel waveguide on silicon: fast direct imprinting and low cost fabrication. *Optics Communications*, 143(4-6):199–202, 1997.

[29] G. R. Atkins, R. M. Krolikowska, and A. Samoc. Optical properties of an ormosil system comprising methyl- and phenyl-substituted silica. *Journal of Non-Crystalline Solids*, 265(3):210–220, 2000.

[30] L. Yang, S. S. Saavedra, N. R. Armstrong, and J. Hayes. Fabrication and characterization of low-loss, sol-gel planar wave-guides. *Analytical Chemistry*, 66(8):1254–1263, 1994.

[31] M. Oubaha, M. Smaihi, P. Etienne, P. Coudray, and Y. Moreau. Spectroscopic characterization of intrinsic losses in an organic-inorganic hybrid waveguide synthesized by the sol-gel process. *Journal of Non-Crystalline Solids*, 318(3):305–313, 2003.

Chapter 4

Waveguide Theory

4.1 Introduction

An optical waveguide is a dielectric structure that transports energy at wavelengths in the infrared, ultraviolet (UV) or visible portions of the electromagnetic spectrum [1]. Optical waveguides can be split into two main categories: the most common type are optical fibres and the second is planar waveguides.

4.1.1 Optical fibres

Optical fibres generally consist of a central core medium which is surrounded by an outer cladding region as shown in Figure 4.1.

The core medium has a higher refractive index than the cladding therefore allowing the light to travel along the fibre by the means of total internal reflection. Total internal reflection occurs when the light strikes the core/cladding interface of the fibre at an angle greater than the critical angle for this interface. The critical angle, θ_c can be calculated using Equation 4.1:

$$\theta_c = \sin^{-1} \frac{n_{clad}}{n_{core}} \tag{4.1}$$

where n_{clad} and n_{core} are the cladding and core refractive indices respectively.

Fibre optics are used for a wide range of applications including transmitting data optically over large distances. Optical fibres are very suitable for this purpose due to their extremely low propagation losses and the fact that they are highly flexible. Optical fibres can also be used for sensing applications. Light is not only confined to the fibre core, as suggested by the ray optics analysis of propagation

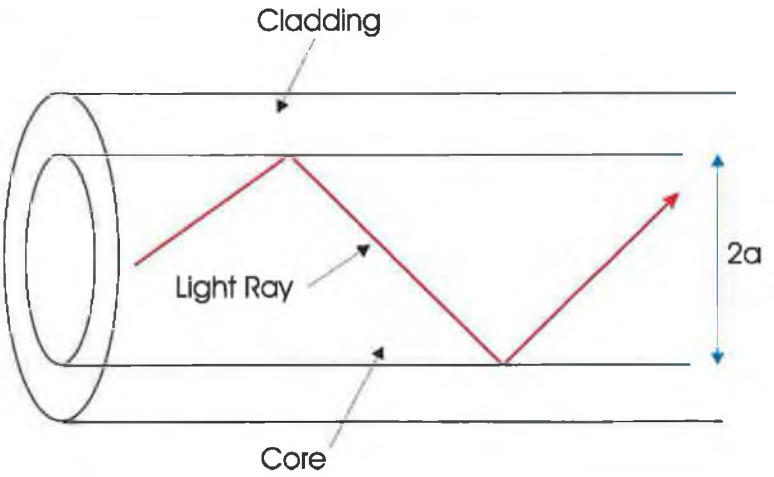

Figure 4.1: Basic structure of an optical fibre.

but can also propagate in the cladding. At the point where total internal reflection occurs an electromagnetic wave is present in the cladding which decays exponentially with distance from the interface where it was formed. This propagation in the cladding is known as the evanescent field. When optical fibres are used in sensor applications this evanescent field can either be used to directly sense an analyte if the interrogation wavelength coincides with the absorption wavelength of the analyte, or an intermediate step can be added whereby a material which reacts optically with the analyte to be sensed, for example by either fluorescence or absorption, can be attached to the waveguide and be investigated by the evanescent field. Indirect sensing is more common due to the larger range of applications. Optical fibres can also be used to carry optical signals to and from an optical probe head and this can be used in the development of optical sensor systems. Absorbance-based sensing of nitrate ions in ground water has been demonstrated with a portable sensor probe with optical fibres which carry UV light to the probe head and return the signal after absorbance. This work will be described in detail in Chapter 2.

While the use of optical fibres in the development of a portable nitrate sensor has been successfully demonstrated, the use of optical fibres in sensor probe configurations cause a range of difficulties associated with their geometry and their fragile nature. The incorporation of optical fibres into an optical probe requires the use of expensive optical elements such as microlenses to successfully couple light into and out of the fibre. Precise alignment of light into an optical sensor can add

difficulty and it is preferable to carry out all the optical parts of sensor detection in the probe head itself and then transmit the signal electrically to whatever detection mechanism is used to prevent distortion of the signal and low signal levels.

For evanescent-wave sensing applications, the properties of the modified cladding layer are crucial in the sensor development. The rate of diffusion of a particular analyte is dependent on the cladding properties and this governs the response time of the sensor. In general, commercially available optical fibres can not be used since the cladding needs to be stripped and replaced with an analyte-sensitive sensing layer. Deposition of the sensing layer onto an optical fibre is difficult due to the geometry of the fibre and standard deposition techniques such as micro-contact printing, pin-printing and spin-coating can not uniformly deposit a sensor layer on the surface of an optical fibre. In general, the deposition method which is used is dip-coating.

4.1.2 Planar waveguides

A planar waveguide consists of a thin dielectric layer deposited on a substrate. The refractive index of the dielectric layer being higher than that of the substrate. A general planar waveguide structure is shown in Figure 4.2. The light travels through the structure again by total internal reflection at both interfaces. These waveguide structures can have many planar geometries and be either symmetric or asymmetric. The substrate and a protective layer are optional for these structures.

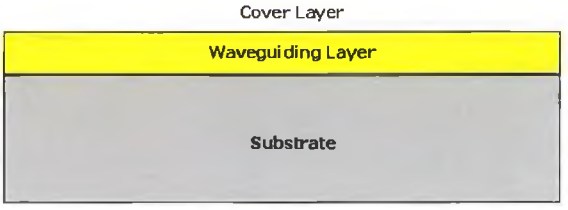

Figure 4.2: Basic structure of a planar waveguide.

Planar waveguide structures do not suffer from some of the disadvantages seen with the use of optical fibres. Their planar geometry lends itself to ease of fabrication and deposition of sensor layers using a much broader range of deposition

techniques. Changes in the absorbance or fluorescence of the sensor layers when interacting with a particular analyte to be sensed can change the light level in the waveguide. Planar waveguides can be incorporated into sensor probes without the need for extensive optical components. Planar waveguide platforms can be used in a variety of ways and are adaptable to the requirements of many optical sensors. They are used in the development of a multi-analyte sensor platform in the main body of this work.

The planar waveguides used in this work were slab waveguides. These are the most basic form of planar waveguides and will be discussed for both symmetric and asymmetric configurations. The light propagation in these waveguides will be described using classical ray optics.

4.2 Slab Waveguides

A planar waveguide consists of a thin waveguiding layer of thickness, d, and refractive index, n_g, which is surrounded by a substrate (medium which supports guiding layer) with refractive index, n_s and a cover layer (medium above the substrate) of refractive index n_l.

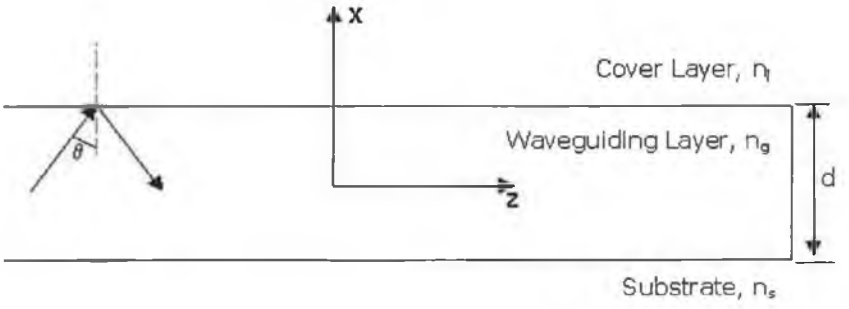

Figure 4.3: Basic structure of a slab waveguide.

This general form is shown in Figure 4.3. The waveguide is described as symmetric if $n_l = n_s$ and asymmetric otherwise. This work will describe the general case when the waveguide can be either symmetric or asymmetric. The initial slab waveguides used in the course of this work consisted of a free standing waveguide layer without a substrate i.e. a waveguide layer surrounded by air, and with a sensor layer deposited on top of the waveguide and were thus asymmetric waveguides.

Figure 4.3 shows a light ray incident on the waveguide at an angle, θ, relative to the normal. The critical angles for both the upper and lower interfaces are defined as:

$$\theta_c^{lg} = \sin^{-1} \frac{n_l}{n_g} \tag{4.2}$$

$$\theta_c^{gs} = \sin^{-1} \frac{n_s}{n_g} \tag{4.3}$$

where θ_c^{lg} is the critical angle for the cover layer/guiding layer interface and θ_c^{gs} is the critical angle at the guiding layer/substrate interface. In general, for the work presented here, the cover layer refractive index is greater than the substrate refractive index i.e. $n_l > n_s$ and it then follows that $\theta_c^{lg} > \theta_c^{gs}$. There are now three possible ranges of incident angle θ where propagation can occur [2].

1. $\theta_c^{lg} < \theta < 90°$: In this case the light is confined in the waveguide by total internal reflections at both interfaces and propagates as shown in Figure 4.4. This mode is called a guided mode.

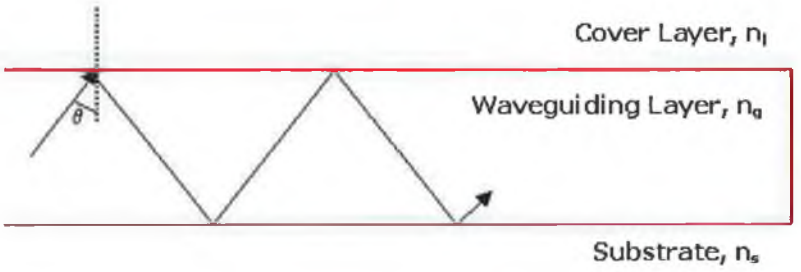

Figure 4.4: Guided mode: $\theta_c^{lg} < \theta < 90°$.

2. $\theta_c^{gs} < \theta < \theta_c^{lg}$: In this case the light undergoes total internal reflection at the waveguide/substrate interface and remains in the waveguide while total internal reflection is not present at the waveguide/cover layer interface as shown in Figure 4.5. Light is able to escape through the cover layer according to Snell's law as $\theta < \theta_c^{lg}$. This light is a cover radiation mode.

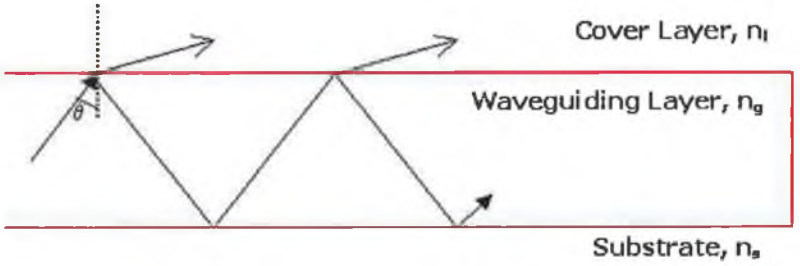

Figure 4.5: Cover radiation mode: $\theta_c^{gs} < \theta < \theta_c^{lg}$.

3. $\theta < \theta_c^{gs}$: In this case, light is able to escape the waveguide at both the waveguide/substrate and the waveguide/cover layer interfaces as shown in Figure 4.6. This mode is called a substrate-cover radiation mode.

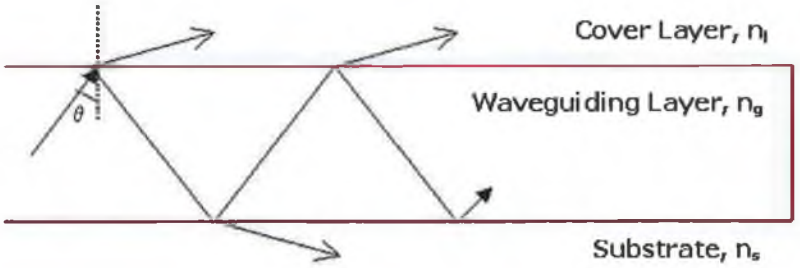

Figure 4.6: Substrate-cover radiation mode: $\theta < \theta_c^{gs}$

4.2.1 Symmetric slab waveguides

To look in more detail at the guidance conditions and the number of modes supported in a slab waveguide we will first look at a symmetric slab waveguide as shown in Figure 4.7. This will first be analysed and then extended to the case of asymmetric waveguides. The symmetric slab waveguide shown consists of a semi-infinite dielectric slab of thickness, d, and refractive index, n_1 surrounded between two regions of refractive index, n_2 where $n_1 > n_2$.

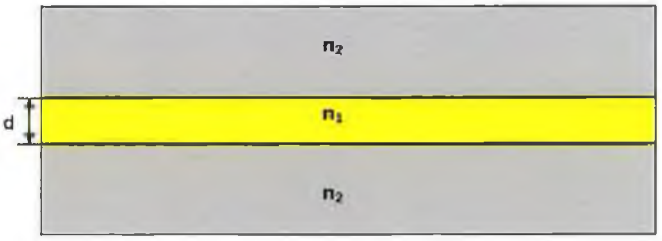

Figure 4.7: Symmetric slab waveguide.

As before, illustrated in Figure 4.4 a ray can propagate completely in the waveguide by total internal reflection when $\theta_c < \theta < 90°$ where θ_c is the critical angle at the waveguide core/outer cladding interface and θ is the internal ray angle with respect to the normal as before. While the diagram only shows a single ray in reality an infinite number of such rays are also propagating in the waveguide. The rays shown represent lines drawn normally to the plane wavefronts. To determine the condition for a mode to propagate in the guide the situation must be split into two cases, the first where $\theta < 45°$ and the second for $\theta > 45°$. The following is a standard wave optics approach to the analysis of guidance conditions within a slab waveguide and can be found in *Optoelectronics:an introduction* by Wilson [3].

The first case is illustrated in Figure 4.8. All the points along the same wavefront must have identical phase. The wavefront FC intersects two of the upwardly travelling portions of the same ray at points A and C. Destructive interference will take place, making it impossible for light to travel down the guide unless the phase at points A and C is the same or differs by a multiple of 2π.

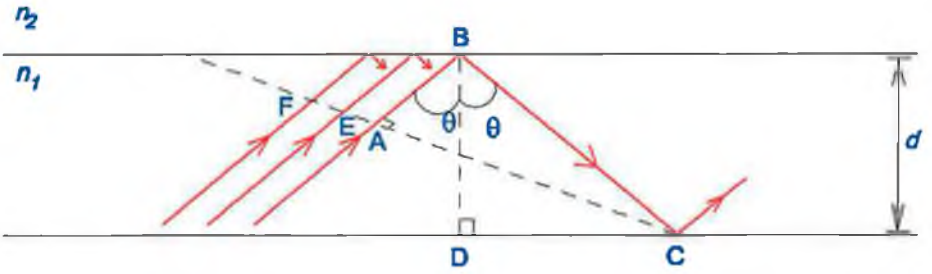

Figure 4.8: Parallel wavefronts where $\theta < 45°$.

The phase difference between A and C depends on the path length AB+BC and

the phase changes due to reflections at the interfaces, B and C. The phase change on reflection is denoted as $\phi(\theta)$.The total phase change can be written as:

$$(AB + BC)\frac{2\pi n_1}{\lambda_0} - 2\phi(\theta) \tag{4.4}$$

where the first term $(AB + BC)\frac{2\pi n_1}{\lambda_0}$ depends on the path difference and the second, $2\phi(\theta)$,depends on the reflection. Thus the phase difference can be expressed as:

$$\text{Phase Difference} = \frac{2\pi}{\lambda_0}(\text{Optical Path Difference}) = \frac{2\pi n_1}{\lambda_0}(AB + BC)$$

From the triangle ABC in Figure 4.8:

$$AB = BC\cos 2\theta$$

$$\Rightarrow AB + BC = BC + BC\cos 2\theta = BC(1 + \cos 2\theta)$$

But

$$\cos 2\theta = 2\cos^2\theta - 1.$$

$$AB + BC = BC(1 + 2cos^2\theta - 1) = 2BC\cos^2\theta$$

Then from triangle BDC in Figure 4.8:

$$BC\cos\theta = d$$

$$\Rightarrow AB + BC = 2d\cos\theta$$

For a mode to propagate, the phase difference must equal $2m\pi$ where m is an integer,

$$(AB + BC)\frac{2\pi n_1}{\lambda_0} - 2\phi(\theta) = 2m\pi$$

$$2d\cos\theta\left(\frac{2\pi n_1}{\lambda_0}\right) - 2\phi(\theta) = 2m\pi$$

$$\frac{4\pi n_1 d\cos\theta}{\lambda_0} - 2\phi(\theta) = 2m\pi$$

$$\frac{2\pi n_1 d\cos\theta}{\lambda_0} - \phi(\theta) = m\pi \tag{4.5}$$

The condition for a mode to propagate when the internal angle, $\theta < 45°$ is shown in Equation 4.5. Next the second situation where $\theta > 45°$ is analysed. This is shown in Figure 4.9.

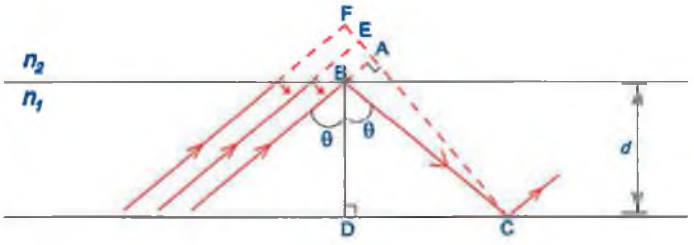

Figure 4.9: Parallel wavefronts where $\theta > 45°$.

The phases at A and C must again be equal, but this time the distance AB represents a negative path length since the ray would have to travel backwards along AB to get from A to B. The total phase change between A and C is

$$(BC - AB)\frac{2\pi n_1}{\lambda_0} - 2\phi(\theta)$$

From Figure 4.9, (BC-AB)=2dcosθ so that the same condition, Equation 4.5 exists for all internal ray angles $> 45°$ *and* $< 45°$. For each value of m, there will be a value of θ which solves the equation. It can be seen that, Figure 4.10 [3], for each value of m there is at most one value of θ *i.e.* θ_m which satisfies the condition for propagation.

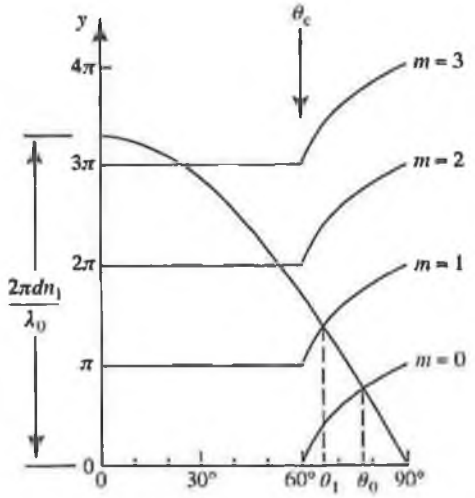

Figure 4.10: Graphical solutions to propagation condition, Equation 4.5 [3].

Each value of θ_m provides a distinct distribution of electric field across the guide

and is called a mode. The characteristics of the mode also depend on whether it is polarised as transverse magnetic (TM) or transverse electric (TE). The resulting modes will be known as TM_m and TE_m modes.

If a particular mode has a value of θ_m such that $\theta_m = \theta_c$ the mode is known as a cut-off mode. If $\theta_m < \theta_c$ the mode is below cut-off and it will not propagate for a significant distance as it will be quickly attenuated. If $\theta_m > \theta_c$ the mode is above cut-off and will be supported by the guide. From the condition for a mode to propagate, Equation 4.5, it can be shown that both TE_m and TM_m modes will be cut-off if:

$$\frac{2\pi n_1 d \cos\theta}{\lambda_0} - \phi(\theta) = m\pi$$

Expressing this condition in terms of refractive index:

$$\cos^2\theta_c + \sin^2\theta_c = 1$$

$$\cos\theta_c = (1 - \sin^2\theta_c)^{\frac{1}{2}}$$

But

$$\sin\theta_c = \frac{n_2}{n_1}$$

$$\Rightarrow (1 - \sin^2\theta_c)^{\frac{1}{2}} = \left[1 - \left(\frac{n_2}{n_1}\right)^2\right]^{\frac{1}{2}}$$

A cut-off mode is present when:

$$\frac{2\pi n_1 d \cos\theta}{\lambda_0}\left[1 - \left(\frac{n_2}{n_1}\right)^2\right]^{\frac{1}{2}} = \pi m$$

or

$$V = \frac{\pi}{2}m \tag{4.6}$$

where

$$V = \frac{\pi d n_1}{\lambda_0}\left[1 - \left(\frac{n_2}{n_1}\right)^2\right]^{\frac{1}{2}}$$

$$\Rightarrow V = \frac{\pi d}{\lambda_0}\left(n_1^2 - n_2^2\right)^{\frac{1}{2}} \tag{4.7}$$

The parameter V is referred to in a variety of ways, V parameter, normalised guide thickness or normalised frequency [3]. From Equation 4.6, the total number of guided modes in a waveguide is given by:

$$N = 1 + INT\left(\frac{2V}{\pi}\right) \tag{4.8}$$

where INT means to take the integer value of $\frac{2V}{\pi}$. It can be seen for this that the number of modes present in a guide will increase with

1. Increasing guide thickness
2. Larger refractive index difference between layers
3. Smaller wavelength of light

It can also be shown from Equation 4.8, that if $V < \frac{\pi}{2}$ only one mode m=0 will propagate i.e.

$$N = 1 + INT\left(\frac{2V}{\pi}\right)$$

gives an integer term of zero so therefore N=1. This is called a single mode guide. This implies that the m=0 mode will always propagate regardless of the dimensions of the guide, refractive indices and wavelength of light and has no cut-off. This is not true for asymmetric waveguides.

A mode is made up of an infinite number of rays propagating in the waveguide at some internal angle. Taking a point anywhere within the waveguide, only two of the rays can pass through it at the same time - one travelling upwards and one downwards as shown in Figure 4.11. In general there will be a phase difference between these two, so that they interfere and this leads to a variation in the field amplitude across the guide. Each mode has a unique field variation associated with it. This phase difference as a function of position within the guide may be determined as illustrated in Figure 4.11.

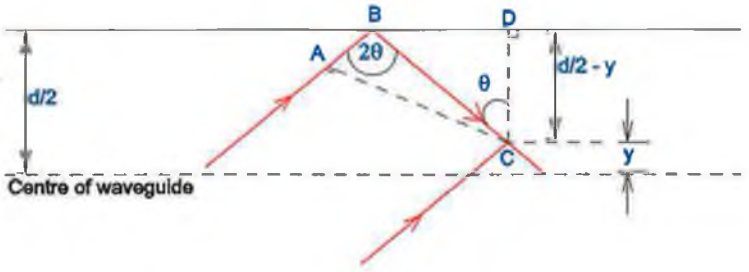

Figure 4.11: Two rays for the same mode travelling in opposite directions and meeting at a point, C, in the waveguide.

Two rays meet at point C, a distance y above the centre of the guide. The line AC represents a wavefront, and thus all points must have the same phase, therefore

the phases at points A and C are the same. The phase difference between the two rays meeting at C, $\Delta\Phi_y$, arises from the path difference AB+BC together with a phase change of $\phi(\theta)$ on reflection at the interface at point B.

From Figure 4.11:

$$AB = BC\cos 2\theta,\ AB + BC = 2BC\cos^2\theta$$

As

$$BC = \frac{\left[\frac{d}{2} - y\right]}{\cos\theta}$$

$$AB + BC = 2\left[\frac{d}{2} - y\right]\cos\theta$$

$$\Delta\Phi_y = (AB + BC)\frac{2\pi n_1}{\lambda_0} - \phi(\theta)$$

$$= 2\left[\frac{d}{2} - y\right]\frac{2\pi n_1\cos\theta_m}{\lambda_0} - \phi(\theta)$$

Rearranging the condition for modes to propagate, Equation 4.5, gives

$$\frac{2\pi n_1\cos\theta}{\lambda_0} = \frac{m\pi + \phi(\theta)}{d}$$

$$\Rightarrow \Delta\Phi_y = 2\left[\frac{d}{2} - y\right]\frac{m\pi + \phi(\theta)}{d} - \phi(\theta)$$

$$= 2\frac{d}{2}\left(\frac{m\pi + \phi(\theta)}{d}\right) - 2y\frac{(m\pi + \phi(\theta))}{d} - \phi(\theta)$$

$$= m\pi + \phi(\theta) - \frac{2y}{d}(m\pi + \phi(\theta)) - \phi(\theta)$$

$$\Delta\Phi_y = m\pi - \frac{2y}{d}[m\pi + \phi(\theta)] \tag{4.9}$$

Now the resultant of two waves with a phase difference $\Delta\Phi_y$ may be written as

$$E_0[\cos(\omega t) + \cos(\omega t + \Delta\Phi_y)]$$

or

$$2E_0 cos\left(\omega t + \frac{\Delta\Phi_y}{2}\right) cos\left(\frac{\Delta\Phi_y}{2}\right)$$

The effective amplitude of the electric field is thus given by $2E_0 cos\left(\omega t + \frac{\Delta\Phi_y}{2}\right)$ which can be written as

$$2E_0 cos\left(\frac{m\pi}{2} - \frac{y}{d}(m\pi + \phi(\theta))\right)$$

At the centre of the guide (y=0) this will have a value of $\pm 2E_0$ or zero, depending on whether m is even or odd. At the guide edges (y=d/2) the amplitude is $2E_0 \cos\phi(\theta)$. The complete mode field pattern is obtained by matching this equation with the exponential decline (E field) in the cladding region. This equation for exponential decline in the cladding region Equation 4.10 is derived in Appendix B, Equation B.23.

$$F(y) = \exp\left[-\frac{2\pi n_2}{\lambda_0}\left(\left(\frac{n_1}{n_2}\right)^2 \sin^2\theta - 1\right)^{\frac{1}{2}} y\right] \tag{4.10}$$

Plots of the transverse E field amplitudes for the four lowest modes in symmetric planar waveguides are shown in Figure 4.12 [3].

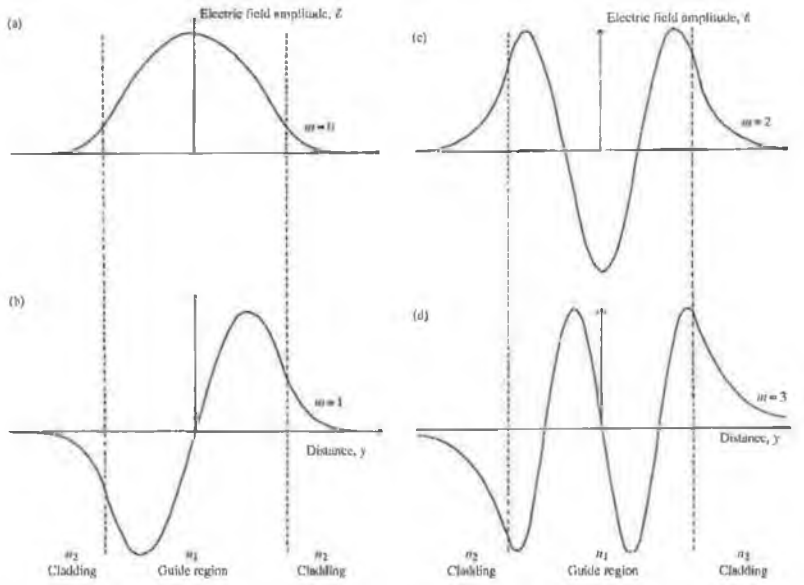

Figure 4.12: Transverse E field amplitudes for the four lowest modes in symmetric planar waveguides [3].

The mode field is next investigated around the cut-off. A plot of the mode field near to and far away from the cut-off is shown in Figure 4.13 [3]. This shows that near the cut-off a significant amount of the mode field is present in the cladding. At the cut-off all the energy from the mode is present in the cladding.

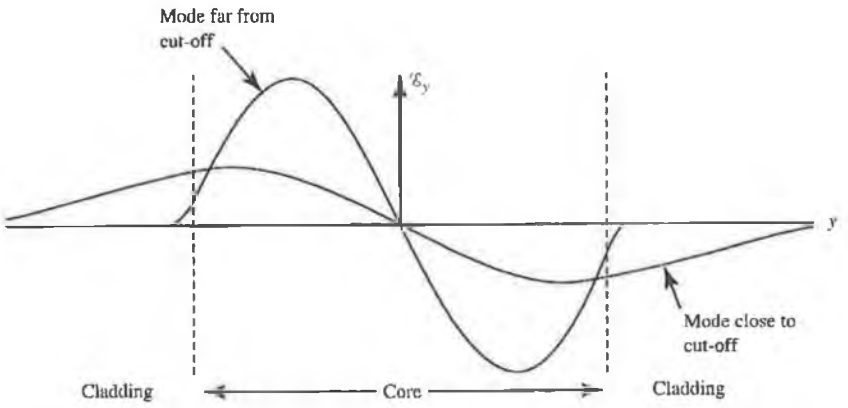

Figure 4.13: Mode field of TE_m modes close to and far from the cut-off [3].

4.2.2 Asymmetric slab waveguides

The treatment of slab waveguides is now extended to asymmetric slab waveguides. The phase changes at the upper and lower interfaces are denoted as $\phi_1(\theta)$ and $\phi_2(\theta)$, respectively. Equation 4.5 can be modified so that the condition for a ray to be able to propagate becomes

$$\frac{4\pi n_1 d\cos\theta}{\lambda_0} - \phi_1(\theta) - \phi_2(\theta) = 2m\pi \tag{4.11}$$

For a guided mode to be supported in the waveguide, total internal reflection must occur at both interfaces. For this to happen, the internal guide angle, θ, must always be greater than the critical angle at both interfaces. These critical angles are denoted by θ_{c1} and θ_{c2} for the upper and lower interfaces respectively. The waveguides first used in this work are highly asymmetric as the material under the guide is air with a refractive index of 1. Therefore the critical angle at the lower interface will be much less than that at the upper interface. For guided rays in the waveguide, it can always be assumed that the internal guide angle will always be much greater then the critical angle at the lower interface and therefore $\phi_2(\theta)$ can be approximated by π. The propagation condition can now be written as

$$\frac{4\pi n_1 d\cos\theta}{\lambda_0} = \phi_1(\theta) + (2m+1)\pi \tag{4.12}$$

In a similar manner to before, the condition for the m=1 mode to propagate

becomes

$$\frac{4\pi n_1 d\cos\theta_{c1}}{\lambda_0} > 3\pi \tag{4.13}$$

In contrast to the symmetric waveguide case, it is now possible for no mode at all to propagate which happens when

$$\frac{4\pi n_1 d\cos\theta_{c1}}{\lambda_0} < \pi \tag{4.14}$$

Thus the condition for only a single mode to propagate becomes

$$\pi < \frac{4\pi n_1 d\cos\theta_{c1}}{\lambda_0} < 3\pi \tag{4.15}$$

By putting $\cos\theta_{c1} = [1 - (\frac{n_2}{n_1})^2]^{\frac{1}{2}}$ this condition can be written as

$$\frac{\pi}{4} \leq V \leq \frac{3\pi}{4} \tag{4.16}$$

where V is defined again as in Equation 4.7. In terms of the guide thickness we have

$$\frac{1}{4(NA)} \leq \frac{d}{\lambda_0} \leq \frac{3}{4(NA)} \tag{4.17}$$

where NA is defined as $(n_1^2 - n_2^2)^{\frac{1}{2}}$

From Equation 4.17, for an asymmetric waveguide there is a minimum thickness below which no mode will propagate - this is in contrast to the case for the symmetric guide.

4.3 Summary

The different types of optical waveguides have been defined. The light propagation in slab waveguides, both symmetric and asymmetric has been described in detail along with the mode structure in the waveguides and the number of modes that a guide can support. A more rigorous wave optics approach by solving Maxwell's equations was demonstrated in the work of a previous member of the research group, Lubos Polerecky [4, 5]. He developed a model to explain how the radiation emitted from a fluorescent layer is coupled into a waveguide structure. This model will also be used in Chapter 6, to model the coupling of fluorescence into the various sensor platforms.

Bibliography

[1] A.W. Snyder and J.D. Love. *Optical Waveguide Theory.* Chapman & Hall, London, 1983.

[2] T. Tamir. *Guided-wave optoelectronics.* Springer-Verlag, New York, 2nd edition, 1990.

[3] J. Wilson and J. Hawkes. *Optoelectronics: an introduction.* Prentice Hall, London, 3rd edition, 1998.

[4] L. Polerecky. *Optimisation of multimode waveguide platforms for optical chemical sensors.* Ph.D. Thesis, Dublin City University, 2002.

[5] L. Polerecky, J. Hamrle, and B. D. MacCraith. Theory of the radiation of dipoles placed within a multilayer system. *Applied Optics*, 39(22):3968–3977, 2000.

Chapter 5

Fluorescence-based Sensing

5.1 Introduction

All of the optical sensor films used in the course of this work are based on changes in the luminescence of an indicator when exposed to an analyte. This chapter describes the processes involved in emission of luminescence and then goes on to discuss the factors that cause changes in the emitted luminescence. The luminescent dyes used during the course of this work are described along with the various methods of detecting a luminescence signal and how this relates to the concentration of the analyte that is being sensed. Finally, the actual fabrication process for the different sensor films developed is described.

5.2 Principles of Fluorescence

When a molecule absorbs electromagnetic energy, this energy is usually lost through non-radiative decay paths such as collisional processes. With certain molecules, which absorb radiation, only part of the energy is lost via collisions and the electron drops back to ground state by emitting a photon of lower energy, and therefore higher wavelength, than was absorbed. This emission process is known as fluorescence [1]. The difference between the peak emission wavelength and the peak excitation wavelength of a particular molecule is called the Stokes shift [2]. This enables the selective detection of the fluorescence emission at higher wavelengths than the excitation. The fluorescence lifetime is the mean time a molecule remains in the excited state before returning to the ground state [3]. All of the sensors described in this work are based on the principle of fluorescence emission.

All electrons in a molecule carry a spin quantum number, S=1/2. This can either represent spin up, ⇑, S=1/2, or spin down ,⇓, S=-1/2. Multiplicity is a term used to express the orbital angular momentum of a given state [4] and is related to the spin by Equation 5.1:

$$M = 2S + 1 \tag{5.1}$$

When all the electrons in a particular state are paired i.e. have opposite spin the total spin quantum number, S=0 (+1/2-1/2=0). In this cause the multiplicity equals 1 and the state is referred to as a singlet state. If the electrons are not paired the total spin quantum number S=1 (+1/2+1/2=1). This state is called a triplet state and its multiplicity equals 3.

When a molecule absorbs radiation it is excited to a higher energy singlet state, as shown in Figure 5.1. This molecule can decay to the ground state by both radiative and non-radiative decay processes. The decay of the molecule from the excited singlet state directly to the ground state with the emission of a photon is the fluorescence emission process. Because some energy is lost in the short time before the decay to the ground level, due to several non-radiative processes, the photon emitted is of a lower energy than that absorbed. The other radiative decay process is phosphorescence. This involves a transition of the molecule from a singlet state, S_1, to a triplet state, T_1, which is called intersystem crossing. Since transitions between states of different multiplicity are quantum mechanically forbidden, T_1 has a much longer lifetime than S_1 and thus phosphorescence lifetimes are much longer than fluorescence lifetimes.

5.2.1 Fluorescence quenching

A process which decreases the fluorescence intensity and lifetime is called quenching. Quenching can occur by different mechanisms. One such mechanism is called collisional quenching. This occurs when the excited state molecule interacts with another molecule, called a quencher, and the fluorescence is decreased. The process of collisional quenching is described by the Stern-Volmer equation, Equation 5.2:

$$\frac{F_0}{F} = 1 + K_{sv}[Q] = 1 + k_q \tau_0 [Q] \tag{5.2}$$

where F_0 is the fluorescence in the absence of the quencher, F is the fluorescence at the quencher concentration, [Q], K_{sv} is the Stern-Volmer constant, k_q is the

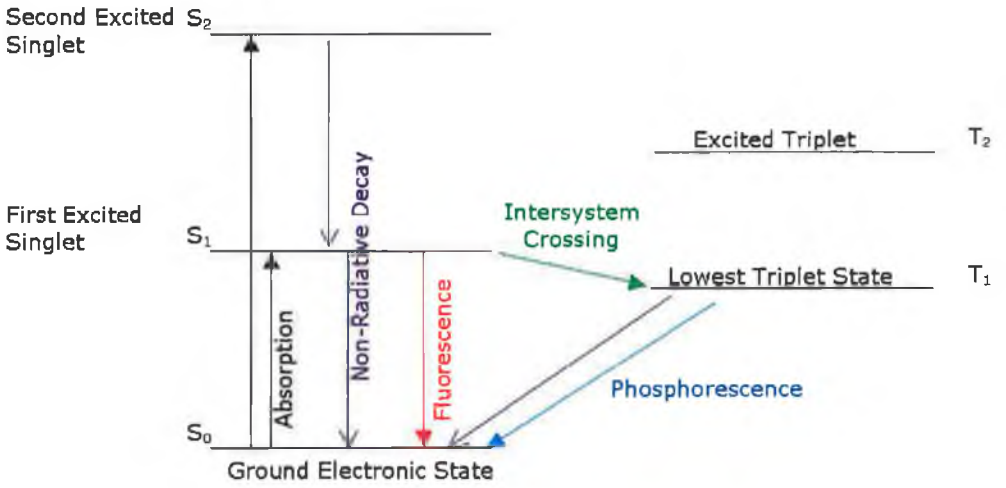

Figure 5.1: Simplified energy level diagram showing absorption and relaxation processes [5].

biomolecular quenching constant and τ_0 is the unquenched lifetime. This relates either the fluorescence intensity or fluorescence lifetime, which are both represented by F in Equation 5.2, to the concentration of the quencher, Q.

Quenching also occurs when the excited molecule reacts with the quencher to form a non-fluorescent complex; this is known as dynamic quenching. Quenching can also occur by many non-molecular mechanisms such as attenuation of incident light by the molecule itself or other absorbing species [1].

5.3 Fluorescence Sensors

The sensor films developed in this work use sol-gel as the immobilisation matrix i.e. the luminophore is encapsulated in a porous sol-gel matrix that enables the analyte to diffuse through and react with the luminophore. The analytes chosen to be sensed for this work were oxygen, relative humidity and carbon dioxide. This combination of analytes was chosen to be applied in the area of indoor air-quality monitoring. Spectral compatibility - i.e. each fluorescent dye having similiar excitation and emission spectra to enable the use of the same optoelectronic components - was an important factor in the choice of fluorescent indicator dyes for the sensor films developed during the course of this work. The fabrication and mechanism of all of

these fluorescence-based sensor films will be described in detail.

5.3.1 Oxygen sensing

Optical oxygen sensing is commonly based on the quenching by oxygen of either the fluorescence intensity or lifetime of an oxygen-sensitive polypyridyl complex which has been incorporated in a suitable porous matrix. In this work, the fluorescent complex, ruthenium(II)-tris-(4,7-diphenyl-1,10-phenanthroline)Cl_2, hereafter referred to as $Ru(dpp)_3Cl_2$, was chosen because of its highly emissive metal-to-ligand charge transfer state, long lifetime, and strong absorption in the blue-green region of the spectrum, which is compatible with high-brightness blue light-emitting diodes (LEDs) [6]. The chemical structure of $Ru(dpp)_3^{2+}$ is shown in Figure 5.2.

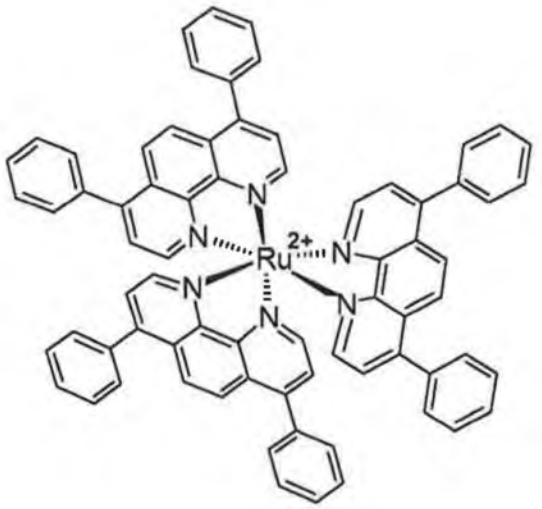

Figure 5.2: Chemical structure of ruthenium(II)-tris-(4,7-diphenyl-1,10-phenanthroline), $Ru(dpp)_3^{2+}$.

The excitation and emission spectra of the complex are shown in Figure 5.3. The excitation peak is at 450nm and the emission peak occurs at 610nm. The operation of all of the sensors developed in this work are based on changes in the luminescent properties of the fluorophores. The oxygen sensor comprises a ruthenium-doped oxygen-sensitive complex, $Ru(dpp)_3Cl_2$, immobilised in a porous sol-gel coating. The intensity and lifetime of the complex decrease in the presence of oxygen due to collisional quenching of the oxygen molecule with the $Ru(dpp)_3Cl_2$ in its excited

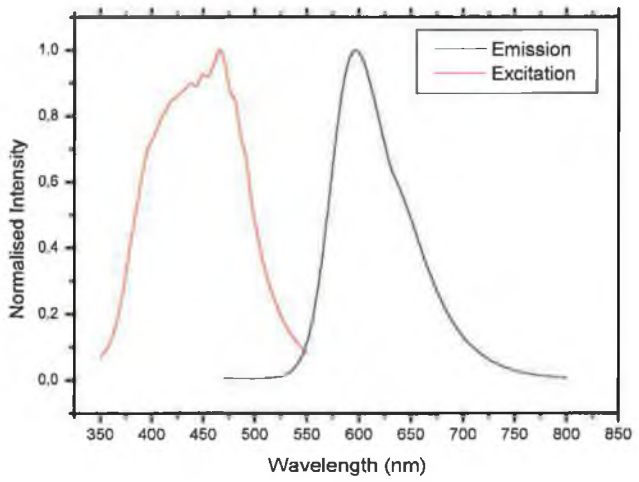

Figure 5.3: Excitation and emission spectra of $Ru(dpp)_3Cl_2$ immobilised in sol-gel matrix.

state, resulting in non-radiative decay to the ground state [7]. For preliminary work, the dye complex was immobilised in a sol-gel matrix similar to previous oxygen sensors [8, 9] and as the work progressed the complex was immobilised in a humidity-insensitive sol-gel coating tailored specifically to prevent cross-sensitivity by moisture.

The doped sol-gel formulation employed for the production of an oxygen-sensitive membrane is similar to one reported previously [10]. The oxygen-sensitive complex, $Ru(dpp)_3Cl_2$, was dissolved in ethanol and mixed with the catalyst, pH 1 HCl, whilst stirring. The sol-gel precursor, methyltriethoxysilane (MTEOS), was then added and the mixture was stirred for 4 hours at room temperature prior to deposition. After deposition, the sensor and substrate were cured for 18 hours at 70°C.

All initial work was carried out using this sol-gel formulation based on the sol-gel precursor, MTEOS. However, during our investigations, the oxygen sensor based on the MTEOS precursor was found to display cross-sensitivity to humidity. From work carried out within the Optical Sensors Laboratory, it was found that by replacing the MTEOS precursor with the precursor, ethyltriethoxysilane (ETEOS), the humidity cross-sensitivity could be minimised [11]. While the humidity cross-

sensitivity is eliminated completely when the film is cured at high temperatures, i.e. greater than 100°C, these temperatures were not used in this work as the glass-transition temperature of the plastic substrate being used, PMMA, was approximately 100°C. Furthermore it was critical to maintain a comparable curing regime for all of the sensor films used in the multi-analyte sensor chip. The ETEOS-based oxygen sensor was thus cured at 70°C and the sensor showed a very small cross-sensitivity to relative humidity. This is shown in Chapter 9.

5.3.2 Relative humidity sensing

A relative humidity sensor was developed using a ruthenium dye complex as the fluorophore which is immobilised in a sol-gel matrix. This sensor has similar spectral properties as those developed for oxygen and carbon dioxide and shows a measurable change in fluorescence intensity and lifetime with changing relative humidity values. Transition metal complexes of the type ruthenium(II)diphenylphenanthroline-dipyridophenazinehexafluorophosphate, ($[Ru(dpp)_2dppz](PF_6)_2$, hereafter referred to as Ru(dppz)), are typically used as DNA intercalators [12]. The chemical structure of $[Ru(dpp)_2dppz]^{2+}$ is shown in Figure 5.4.

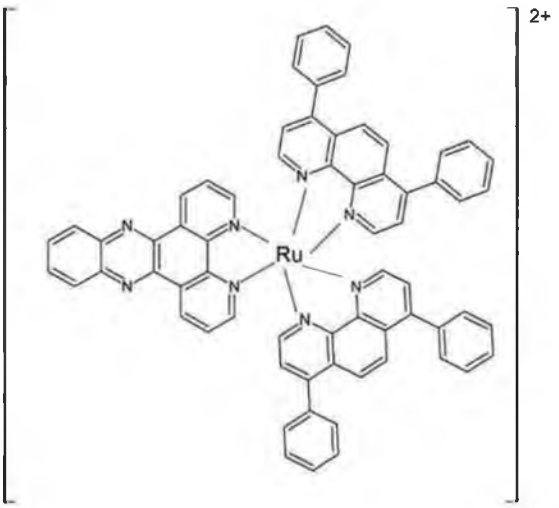

Figure 5.4: Chemical structure of ruthenium(II)diphenylphenanthroline-dipyridophenazine, $[Ru(dpp)_2dppz]^{2+}$.

The luminescence behaviour of these dipyridophenazine-based metallointercalators is very sensitive to the solvent environment. In organic solutions, emission from the photoexcited Ru(dppz) metal-to-ligand charge transfer (MLCT) state is easily detected. In aqueous and protic solutions, the emission is quenched via the interaction of protons with the phenazine nitrogens on the dppz ligand [13]. The quenching of this complex can be used to develop intensity or lifetime-based sensors for measuring both atmospheric relative humidity and water content in organic solvents [14]. The indicator is immobilised in a largely hydrophilic sol-gel matrix to ensure proton diffusion into the matrix to interact with the phenazine nitrogens. This sensing dye is highly suitable as a relative humidity sensor for the multi-analyte application. Its spectral properties enable it to be excited in the visible region ($\lambda_{ex} \approx 450nm$) and its large Stokes shift enables easily discriminated detection of fluorescence at the emission peak, $\lambda_{em} \approx 593nm$ as shown in Figure 5.5. It was chosen as a suitable indicator for this work as its spectral properties are compatible with the excitation and detection optoelectronics of the oxygen-sensitive complex, $Ru(dpp)_3Cl_2$, thus allowing the use of common optoelectronic components and phase-sensitive detection electronics for both sensors.

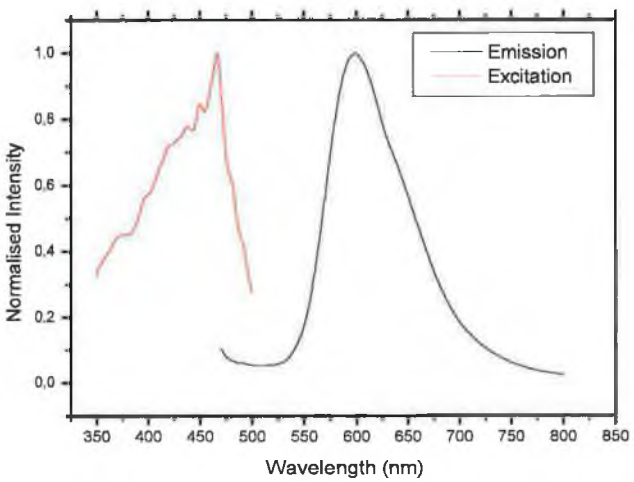

Figure 5.5: Excitation and emission spectra of Ru(dppz) immobilised in sol-gel matrix.

The relative humidity sensor was prepared in the following manner: the

humidity-sensitive dye complex, Ru(dppz), was dissolved in acetonitrile and mixed with pH 1 HCl, which acted as the catalyst, whilst stirring. The sol-gel precursors, methyltriethoxysilane (MTEOS), and tetraethoxysilane (TEOS) (Ratio: 1:1.5 MTEOS:TEOS) were then added and the mixture was stirred for 30 minutes at room temperature. The sol was then aged, for a range of times between 30 minutes and 6 hours, at 70°C before coating. After deposition, the sensor was cured for 18 hours at 70°C.

5.3.3 Carbon dioxide sensing

There is no simple analogue to the oxygen-sensitive and humidity-sensitive ruthenium complexes for carbon dioxide sensing. Instead the acidic nature of carbon dioxide is exploited by using a pH sensor to indirectly measure carbon dioxide concentration. A pH sensitive dye, 8-Hydroxypyrene-1,3,6-trisulfonic acid trisodium salt, hereafter referred to as HPTS, is encapsulated in a sol-gel matrix. The chemical structure of this dye is shown in Figure 5.6.

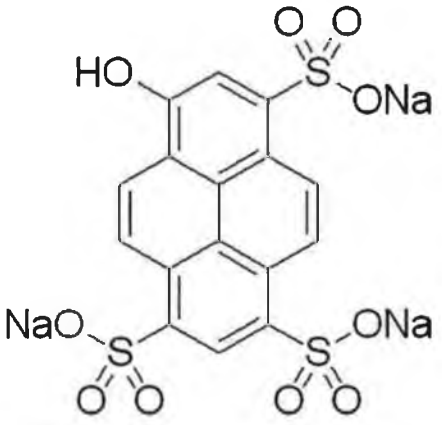

Figure 5.6: Chemical structure of 8-hydroxypyrene-1,3,6-trisulfonic acid trisodium salt, HPTS.

When carbon dioxide diffuses through the matrix it reacts with the water present in it to form carbonic acid according to Equation 5.3.

$$CO_2 + H_2O \Longleftrightarrow H_2CO_3 \tag{5.3}$$

This acid formation causes a change in pH and as a result inhibits the dissociation of the fluorescent indicator according to the following Equation 5.4:

$$[D^-] + H^+ \Longleftrightarrow [HD] \tag{5.4}$$

where $[D^-]$ is the deprotonated and [HD] is the protonated form of HPTS respectively. Since the fluorophore being monitored is the deprotonated form of the dye, the CO_2 concentration can be determined from changes in fluorescence of the deprotonated dye. In effect, the fluorescence from the deprotonated form of HPTS is dynamically quenched by the hydrogen ions forming a compound [HD] with the fluorophore $[D^-]$. In the wavelength range being monitored for CO_2 sensing, the compound [HD] does not fluoresce.

The deprotonated form of the indicator dye HPTS also absorbs in the blue region of the spectrum and emits in the green region. This enables the use of the same light source, a single blue LED, to excite both the HPTS for carbon dioxide sensing and the ruthenium complexes for oxygen and relative humidity sensing. The excitation and emission spectra of the HPTS dye complex are shown in Figure 5.7

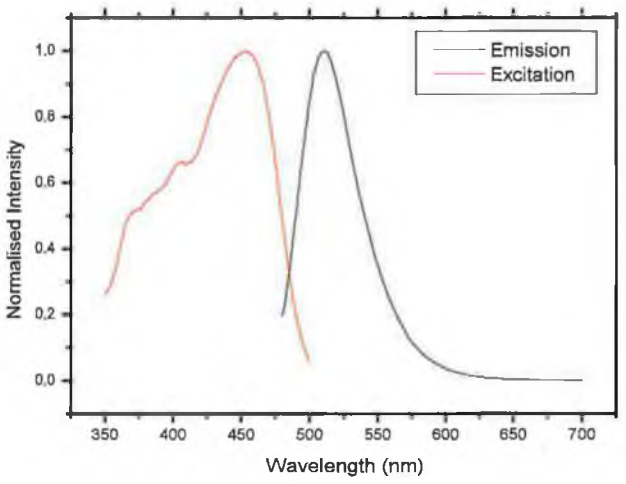

Figure 5.7: Excitation and emission spectra of HPTS dye complex.

Initially the HPTS dye was immobilised in a sol-gel matrix in a similar manner to the oxygen sensors described in Section 5.3.1. It was found that this method

did not incorporate enough water in the matrix to enable carbon dioxide sensing over a prolonged period of time. To this end methods of maintaining water in the sensor matrix were investigated and will be described in Section 5.3.3.

The pH-sensitive indicator dye has a very short lifetime and thus is not suited to phase fluorometry using low-cost components. A new sensing technique Dual Luminophore Referencing (DLR) is used to overcome this. This involves co-immobilising sol-gel nanoparticles doped with the ruthenium complex along with HPTS in the sensing matrix. This enables a phase domain measurement and provides a referenced intensity output [15–17]. This technique is described in detail in Section 5.4.3.

Intensity-based CO_2 sensor films

Sensor films for intensity-based carbon dioxide were first developed using the HPTS dye immobilised in a TMOS-based sol-gel matrix [18]. The sensor films were prepared in the following manner: the HPTS was first dissolved in methanol and then mixed with the catalyst, pH4 HCl. The sol-gel precursor, tetramethoxysilane, (TMOS), was then added, dropwise, while stirring. The mixture was then stirred for 1 hour and aged for 18 hours at room temperature prior to coating. After coating, the sensor was cured for 18 hours at 70°C. While these sensor films showed a clear response to changing carbon dioxide concentration, the sensor matrix dried out easily and the absence of water resulted in a rapid decrease in sensitivity of the sensor.

As the sensing mechanism for carbon dioxide sensing involves the reaction of carbon dioxide with water in the sensor membrane to form carbonic acid resulting in a change in the pH, a key challenge in the development of the sensor matrix is to ensure that sufficient water is maintained within the matrix. This challenge has been addressed by Mills et al [19, 20] and Wolfbeis [21] by using an ion-pairing method to encapsulate highly polar dyes into hydrophobic materials such as silicone rubber and ethyl cellulose. This technique utilises a phase transfer reagent to incorporate the dye into the lipophilic support matrix, and incorporates sufficient water of crystallisation into the matrix. The work undertaken in this lab [22, 23] involves encapsulation of the dye in a hydrophobic sol-gel matrix. A lipophilic dye-counter-ion pair is created by using a phase transfer reagent, in this case tetraoctylammounium hydroxide (TOA-OH), thus allowing the polar dye to be incorporated in a glass matrix.

The carbon dioxide sensor films were produced in the following manner: Tetraoctylammonium bromide was dissolved in MTEOS with the addition of a few drops of chloroform. This was added to the HPTS in aqueous NaOH and stirred. The organic layer was extracted and washed several times. This solution of the dye/counter-ion pair in MTEOS was added dropwise to aqueous HCl (pH1 or pH2) and stirred for one hour. Tetraoctylammonium hydroxide solution (TOA-OH) was prepared by stirring silver oxide and tetraoctylammonium bromide in methanol for 4 hours. The methanolic free base was decanted and stored in the refrigerator. Various amounts of TOA-OH were added before coating. The sensor films were cured for 18 hours at 70°C and were stored in a humid atmosphere for one week prior to testing to allow for stabilisation of the films.

Lifetime-based CO_2 sensor films

As described in Section 5.3.3, due to the short lifetime of the indicator dye, HPTS, direct measurement of the fluorescence lifetime is not possible with the deliberately low-cost instrumentation used in the course of this work. Dual Luminophore Referencing (DLR) is the technique employed (Section 5.4.3) to enable measurement of CO_2 in the phase domain. This technique involves co-immobilising the indicator dye, HPTS in a matrix with a reference luminophore. The reference luminophore used in this work is $Ru(dpp)_3Cl_2$. To eliminate cross-sensitivity of the reference luminophore to oxygen, the $Ru(dpp)_3Cl_2$ dye complex, was encapsulated in dense sol-gel particles which were oxygen impermeable. The excitation and emission spectra for the DLR-based sol-gel sensor films are shown in Figure 5.8.

The phase transfer reagent used in the fabrication of these carbon dioxide sensors is cetyltrimethylammonium hydroxide (CTA-OH). The CO_2 sensor was prepared in the following manner: a solution of CTA-OH in methanol was prepared as reported elsewhere [24]. Dense TEOS microparticles containing the ruthenium complex were synthesised and used as the DLR reference [25]. The particles were added to the MTEOS-based sol. After mixing, the required quantity of HPTS dissolved in CTA-OH, was added [16]. The mixture was then saturated with CO_2 gas and films were deposited on a substrate for characterisation. Films were dried at 70°C for four days and then stored under humid conditions.

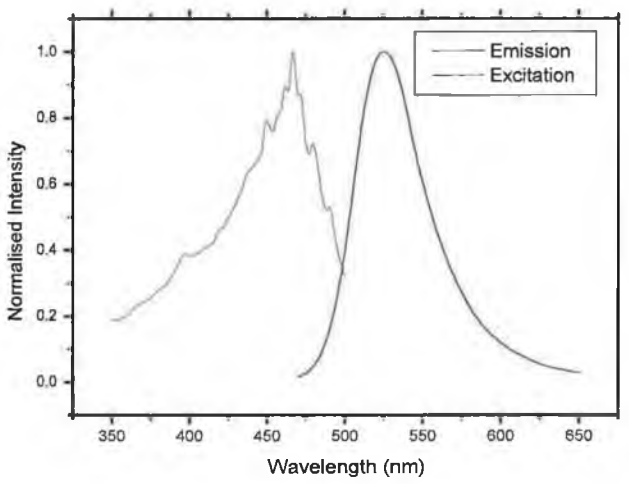

Figure 5.8: Excitation and emission spectra of carbon dioxide sensor film which consisted of HPTS and ruthenium dye complexes co-immobilised in sol-gel matrix for DLR-based sensing.

5.3.4 Sensor dye summary

In summary, all the sensor films are based on a fluorescent dye immobilised in a sol-gel matrix. The oxygen sensor uses a ruthenium dye complex, $Ru(dpp)_3Cl_2$ and either MTEOS or ETEOS as the sol-gel precursor. The relative humidity sensor exploits a different ruthenium dye complex, Ru(dppz), in a sol-gel matrix based on a mixture of TEOS and MTEOS sol-gel precursors. The carbon dioxide sensor consists of an indicator dye, HPTS, and a reference dye, $Ru(dpp)_3Cl_2$ in TEOS-based particles, co-immobilised in a MTEOS-based sol-gel matrix. All of the sensor films have spectral properties that allow them to be monitored using the same optical configuration.A comparison of the excitation spectra of the sensor films for the three different analytes is shown in Figure 5.9 along with the emission spectra of the blue excitation LED. The emission spectra of the three sensors are also shown, confirming that all three sensors are spectrally compatible and can be analysed with the same optical configuration.

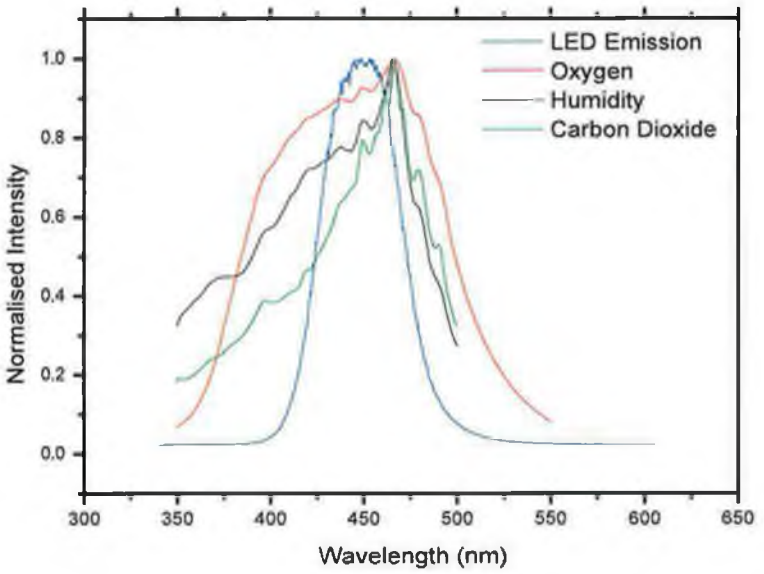

(a) Excitation Spectra

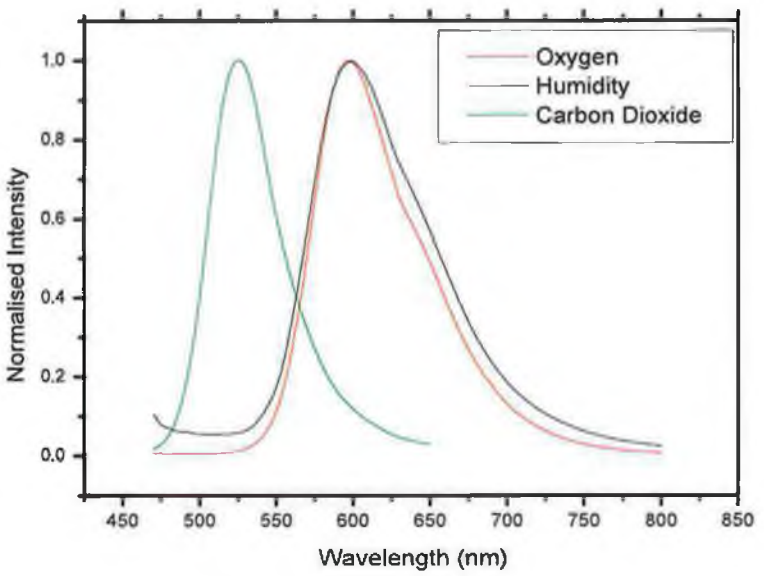

(b) Emission Spectra

Figure 5.9: Excitation and emission spectra of both oxygen and carbon dioxide sensing films along with emission spectra of the blue light source.

5.4 Fluorescence Detection Methods

5.4.1 Intensity-based sensing

Initially, the detection mechanism used for the sensor films in this work involved monitoring the fluorescence intensity for a range of analyte concentrations. This intensity was monitored using a range of detectors, for example: a linear image sensor, a CCD camera and photodiodes. Intensity-based sensing is the simplest method of monitoring the fluorescence output from a sensor film as it does not require advanced detection and control electronics. However intensity-based sensing suffers many problems due to lack of repeatability. Factors, such as drift in the light source or detector, or the interference of ambient light, can lead to changes in the fluorescence intensity from a sensor film. Intensity-based sensing can be improved upon by incorporation of lock-in detection but some problems will still remain and cause a non-repeatable output to be obtained.

To overcome the problem of ambient light affecting the fluorescence light intensity signal, lock-in detection can be used. This involves modulating the excitation light source and using a reference signal of the same frequency so that the detection circuitry can effectively extract the emitted signal from the sensing film. The detection circuitry can consist of a commercial lock-in amplifier or custom-built electronics including a lock-in chip such as the AD630. Both have been used for the preliminary measurements during the course of this work. As intensity-based sensing exhibits substantial stability problems the use of lifetime-based sensing was investigated.

5.4.2 Lifetime-based sensing

The fluorescence lifetime of an indicator is an intrinsic property and is virtually independent of fluctuations in light intensity, detector sensitivity and light path of the optical system [1]. In the case of a single exponential decay, the lifetime, τ, is defined as the time after which the fraction 1/e of the excited molecules still exist in the excited state. This is illustrated in Figure 5.10.

In this laboratory, previous optical sensor designs have been based on intensity quenching [8, 22, 23, 26–28]. While these sensors exhibit very good signal-to-noise ratio (SNR) and sensor response data, they suffer from baseline drift due to LED output fluctuations and are susceptible to drift due to sensor film positioning vari-

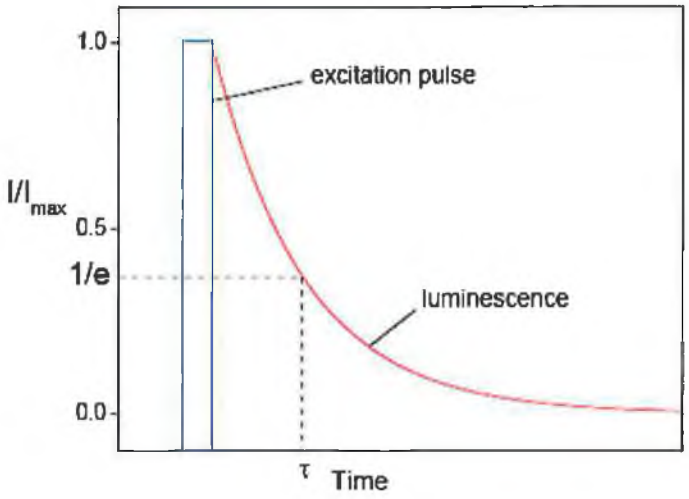

Figure 5.10: Fluorescence lifetime measurement of single exponential decay [16].

ations. There is also the possibility of response variations due to dye leaching and photobleaching. Most of these problems can be overcome by directly measuring the lifetime of the sensor. These effects can be minimised by operating the sensor in the time domain instead of the intensity domain.

Two methods of lifetime-based measurement were used in the course of this work. The first, direct measurement of lifetime was used to measure the absolute value of fluorescence lifetime. In the second case, which was used for most of the work presented, the lifetime is monitored as a function of analyte concentration using phase fluorometric techniques, where one measures an analyte-sensitive phase difference between the modulated reference excitation signal and the resultant modulated fluorescence emission signal. Lifetime sensors have been previously developed in this group for both oxygen and carbon dioxide using phase fluorometry [10, 17].

Phase fluorometry

Phase fluorometry involves operating in the time domain instead of in the intensity domain [10]. If the excitation signal is sinusoidally modulated, the dye fluorescence is also modulated but is time delayed or phase-shifted, relative to the excitation signal as shown in Figure 5.11.

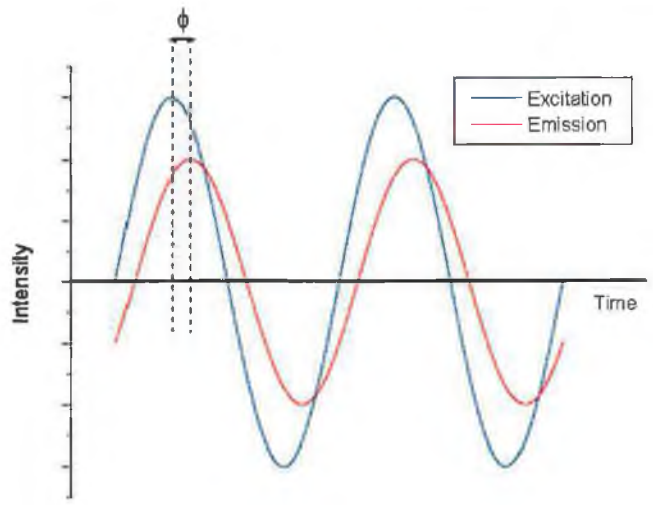

Figure 5.11: Principle of phase fluorometric technique.

The fluorescent species is excited with light having a time-dependent intensity, E(t), of the form shown in Equation 5.5.

$$E(t) = A \sin \omega t \tag{5.5}$$

where A is the amplitude of the excitation signal and ω is the angular frequency which is equal to $2\pi f$ where f is the modulation frequency. The resultant emission from the fluorescent species is modulated at the same frequency as the excitation. The modulated emission is phase-shifted by an angle, ϕ, relative to the excitation. The phase-shifted emission, R(t), is written in the form of Equation 5.6:

$$R(t) = A_{em} \sin (\omega t - \phi) \tag{5.6}$$

where A_{em} is the amplitude of the emission and ϕ is the phase shift. The relationship between the lifetime, τ, of the indicator and the corresponding phase shift, ϕ, for a single exponential decay is described by Equation 5.7:

$$\tau = \frac{\tan \phi}{2\pi f} \tag{5.7}$$

This phase shift, ϕ, is illustrated in Figure 5.11. While multi-exponential decay is present from both the intrinsic properties of the dye and the non-homogeneity of the film, phase fluorometry measures a phase angle which is proportional to the

average lifetime and thus the sensor calibration is not effected by having multi-exponential decay present.

5.4.3 Dual Luminophore Referencing

As discussed previously in Section 5.3.3, a pH indicator dye, HPTS, is used for optical carbon dioxide sensing. The fluorescence lifetime of this dye is too short to be measured by the standard low-cost instrumentation used for phase fluorometry. To overcome this problem a new detection method called Dual Luminophore Referencing (DLR) is used [15]. In the DLR referencing scheme, two different luminescence signals are generated in the sensing membrane. These can be represented as two single sine wave signals as indicated in Figure 5.12. The luminophores must have a significant overlap in their excitation and emission spectra, so that both signals are excitable by a single light source and detected by a single filter-detector combination. In the case of optical carbon dioxide sensing, the inert reference dye used is a ruthenium dye complex which has similar spectral properties to the indicator dye, HPTS, as shown in Figure 5.9. As shown in Figure 5.12, the total signal amplitude (Total Emission) is a superposition of the two signals generated by the analyte-sensitive fluorophore (HPTS) and the inert reference luminophore [16].

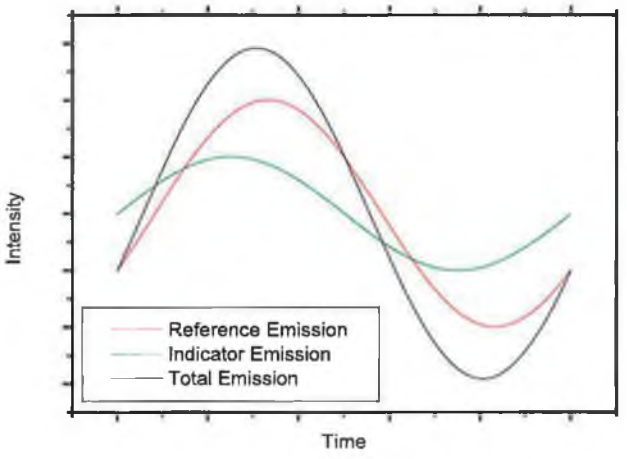

Figure 5.12: Emission of both luminophores and the total signal.

The HPTS signal has a phase angle, $\phi_{HPTS} \approx 0$, due to its very short lifetime,

whereas, in the absence of oxygen quenching, the reference has a constant amplitude and phase angle, ϕ_{ref}, determined by the modulation frequency, f, and its decay time, τ. The superposition of the two signals will result in a non-zero phase angle, ϕ_m of the total measured signal.

The sensing membrane is excited in the same manner as in Equation 5.5. This results in a phase-shifted emission from both the reference and indicator luminophores according to Equation 5.8 and 5.9:

$$R_{ref}(t) = A_{ref} \sin(\omega t - \phi_{ref}) \tag{5.8}$$

$$R_{ind}(t) = A_{ind} \sin(\omega t - \phi_{ind}) \tag{5.9}$$

The resultant total emission is the sum of the emission from the two luminophores. Using approximate values for the lifetime of the selected fluorescent dyes, Equation 5.7, and a typical modulation frequency of 20kHz, phase angle values have been calculated and are shown in Table 5.1. These values are used to display the phase shift between the total emission signal and the excitation signal when the indicator amplitude changes i.e. when the carbon dioxide concentration changes. As the indicator amplitude decreases, which coincides with an increase in the carbon dioxide concentration as described in Section 5.3, the total phase angle increases. This is shown in Figure 5.13 where the indicator intensity is varied and the phase shift variation is shown. The DLR technique provides a fluorescence output signal which can be measured in the phase domain. This method eliminates some of the problems of unreferenced intensity measurements. As part of this work, a model of the DLR technique has been developed in Matlab, described in Appendix C (Section C.1), and is used to determine the effect of varying the different parameters in the DLR equations.

Fluorescent Dye	Approx Lifetime, τ	Phase Angle, ϕ, °
Ruthenium	5μs	32.14
HPTS	5ns	0.035

Table 5.1: Phase Angles for both fluorescent dyes calculated from approximate fluorescent lifetimes.

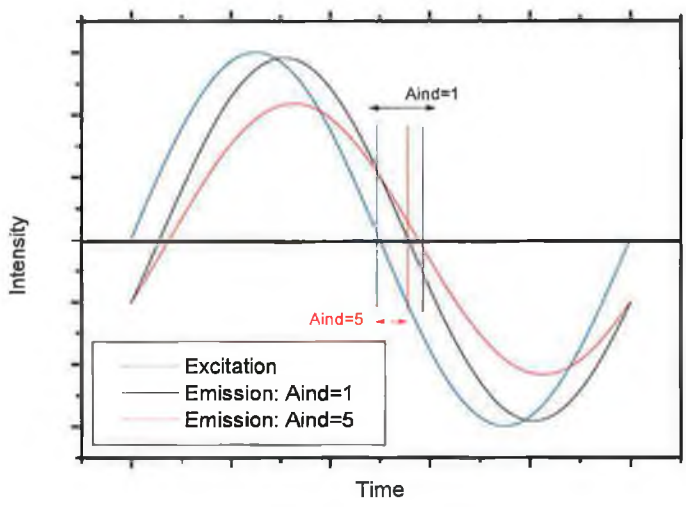

Figure 5.13: Dual Luminophore Referencing - Changes in phase shift, ϕ induced by changes in indicator amplitude.

The range and sensitivity of the sensor can be tailored by altering the ratio of fluorescence from the indicator dye to fluorescence from the reference dye reaching the detector. This can be achieved by altering the respective concentrations of the reference and indicator dyes or by changing the optical filtering.

Figure 5.14 shows the relationship between the indicator amplitude and the phase angle for a range of reference amplitudes, A_{Ref}. This figure shows the higher the ratio of fluorescence emission from HPTS to Ru results in a more sensitive sensor.

The total phase angle, measured from the DLR scheme needs to be correlated with the carbon dioxide concentration. A theoretical analysis [15] of the process shows that $\cot \phi_m$ is linearly dependent on the amplitude ratio of the two signals (A_{ind} / A_{ref}), thereby referencing out any drifts that might occur due to power fluctuations or temperature changes and is described by Equation 5.10.

$$\cot \phi_m = \cot \phi_{ref} + \frac{1}{\sin \phi_{ref}} \frac{A_{ind}}{A_{ref}} \tag{5.10}$$

In summary, the DLR technique provides a referenced intensity output. As the carbon dioxide concentration increases the amplitude of the indicator fluores-

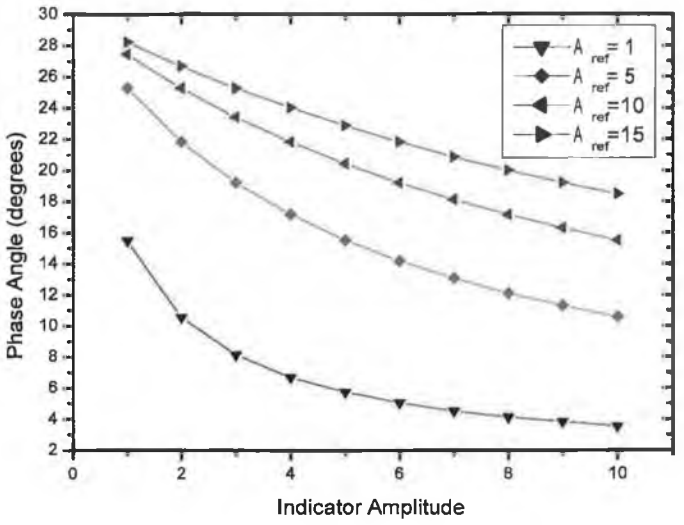

Figure 5.14: Relationship between indicator amplitude and phase angle for a range of reference amplitudes.

cence decreases and the total phase angle increases. This phase angle can thus be correlated with carbon dioxide concentration. The sensitivity of the sensor can be altered by changing the ratio of the fluorescence from the indicator dye to the reference dye or by decreasing the amount of reference dye present. The higher proportion of indicator dye to reference dye increases sensitivity. This ratio can be changed either in the actual composition of the sensor film itself or by altering the optical filtering.

5.5 Summary

The principle of luminescence emission and how this can be applied to detect changes in analyte concentration from an analyte-specific sensor film has been described. The analyte-sensitive indicator dyes used for oxygen, carbon dioxide and relative humidity sensors have been detailed along with the fabrication methods for the sensor films for these analytes. Methods of detection using both intensity and lifetime measurements have also been described.

Bibliography

[1] J. Lakowicz. *Principles of Fluorescence Spectroscopy.* Plenum Press, New York, 2nd edition, 1999.

[2] D. Rendell. *Fluorescence and Phosphorescence.* Wiley, Chichester, 1987.

[3] J.N. Demas. *Excited State Lifetime Measurements.* Academic Press, New York, 1983.

[4] G.D. Christian. *Analytical Chemistry.* John Wiley & Sons, New York, 4th edition, 1986.

[5] G.G. Guilbault. *Practical Fluorescence; Theory, Methods and Techniques.* Dekker, New York, 1973.

[6] J. N. Demas, B. A. DeGraff, and P. B. Coleman. Oxygen sensors based on luminescence quenching. *Analytical Chemistry*, 71(23):793A–800A, 1999.

[7] A.K. McEvoy. *Development of an optical sol-gel-based dissolved oxygen sensor.* Ph.D. Thesis, Dublin City University, 1996.

[8] C. McDonagh, B. D. MacCraith, and A. K. McEvoy. Tailoring of sol-gel films for optical sensing of oxygen in gas and aqueous phase. *Analytical Chemistry*, 70(1):45–50, 1998.

[9] A. K. McEvoy, C. McDonagh, and B. D. MacCraith. Optimisation of sol-gel-derived silica films for optical oxygen sensing. *Journal of Sol-Gel Science and Technology*, 8(1-3):1121–1125, 1997.

[10] C. McDonagh, C. Kolle, A. K. McEvoy, D. L. Dowling, A. A. Cafolla, S. J. Cullen, and B. D. MacCraith. Phase fluorometric dissolved oxygen sensor. *Sensors and Actuators B: Chemical*, 74(1-3):124–130, 2001.

[11] D. Wencel, C. Higgins, A. Guckian, C. McDonagh, and B.D. MacCraith. Novel hybrid sol-gel materials for smart sensor windows. *Proc. SPIE*, 5826:696–705, 2005.

[12] R. M. Hartshorn and J. K. Barton. Novel dipyridophenazine complexes of ruthenium(ii) - exploring luminescent reporters of DNA. *Journal of the American Chemical Society*, 114(15):5919–5925, 1992.

[13] Y. Jenkins, A. E. Friedman, N. J. Turro, and J. K. Barton. Characterization of dipyridophenazine complexes of ruthenium(ii) - the light switch effect as a function of nucleic-acid sequence and conformation. *Biochemistry*, 31(44):10809–10816, 1992.

[14] S. J. Glenn, B. M. Cullum, R. B. Nair, D. A. Nivens, C. J. Murphy, and S. M. Angel. Lifetime-based fiber-optic water sensor using a luminescent complex in a lithium-treated Nafion(TM) membrane. *Analytica Chimica Acta*, 448(1-2):1–8, 2001.

[15] C. Huber, I. Klimant, C. Krause, T. Werner, T. Mayr, and O. Wolfbeis. Optical sensor for seawater salinity. *Fresenius Journal of Analytical Chemistry*, 368:196–202, 2000.

[16] C. von Bültzingslöwen. *Development of optical sensors ("optodes") for carbon dioxide and their applications to Modified Atmosphere Packaging (MAP).* Ph.D. Thesis, University of Regensburg, 2003.

[17] C. von Bültzingslöwen, A. K. McEvoy, C. McDonagh, B. D. MacCraith, I. Klimant, C. Krause, and O. S. Wolfbeis. Sol-gel based optical carbon dioxide sensor employing dual luminophore referencing for application in food packaging technology. *Analyst*, 127(11):1478–1483, 2002.

[18] V.J. Murphy. *Quasi-distributed fibre-optic chemical sensing using telecom fibre.* M.Sc. Thesis, Dublin City University, 1997.

[19] A. Mills and K. Eaton. Optical sensors for carbon dioxide: an overview of sensing strategies past and present. *Quimica Analitica*, 19:12–24, 2000.

[20] A. Mills, Q. Chang, and N. McMurray. Equilibrium studies on colorimetric plastic film sensors for carbon dioxide. *Analytical Chemistry*, 64:1383–1389, 1992.

[21] B.H. Weigl and O.S. Wolfbeis. New hydrophobic materials for optical carbon dioxide sensors based on ion pairing. *Analytica Chimica Acta*, 302:249–254, 1995.

[22] C. Malins, M. Niggemann, and B. D. MacCraith. Multi-analyte optical chemical sensor employing a plastic substrate. *Measurement Science & Technology*, 11(8):1105–1110, 2000.

[23] C. Malins and B. D. MacCraith. Dye-doped organically modified silica glass for fluorescence based carbon dioxide gas detection. *Analyst*, 123(11):2373–2376, 1998.

[24] Q. Chang, L. Randers-Eichhorn, J. R. Lakowicz, and G. Rao. Steam-sterilizable, fluorescence lifetime-based sensing film for dissolved carbon dioxide. *Biotechnology Progress*, 14(2):326–331, 1998.

[25] G. De, B. Karmakar, and D. Ganguli. Hydrolysis-condensation reactions of TEOS in the presence of acetic acid leading to the generation of glass-like silica microspheres in solution at room temperature. *Journal of Materials Chemistry*, 10(10):2289–2293, 2000.

[26] B. D. MacCraith, G. O'Keeffe, A. K. McEvoy, C. M. McDonagh, J. F. McGilp, B. O'Kelly, J. D. O'Mahony, and M. Cavanagh. Light-emitting-diode-based oxygen sensing using evanescent-wave excitation of a dye-doped sol-gel coating. *Optical Engineering*, 33(12):3861–3866, 1994.

[27] C. M. McDonagh, A. M. Shields, A. K. McEvoy, B. D. MacCraith, and J. F. Gouin. Optical sol-gel-based dissolved oxygen sensor: Progress towards a commercial instrument. *Journal of Sol-Gel Science and Technology*, 13(1-3):207–211, 1998.

[28] C. S. Burke, O. McGaughey, J. M. Sabattié, H. Barry, A. K. McEvoy, C. McDonagh, and B. D. MacCraith. Development of an integrated optic oxygen sensor using a novel, generic platform. *Analyst*, 130(1):41–45, 2005.

Chapter 6

Sensor Platform Theory

6.1 Introduction

The aim of this work is to develop a low-cost mass-producible sensor platform for fluorescence-based sensing which is capable of efficient capture and detection of the fluorescence from thin film optical sensors. A range of optical sensor platforms have been developed which are all based on the concept of efficient fluorescence capture. Sensor platforms consisting of a waveguide layer with a sensor film deposited on top, as described in Chapter 4, have been developed in the course of this work. Much work has been done on improving the efficiency of collection of fluorescence and a theoretical model developed previously in this research group was used to optimise fluorescence detection [1,2]. This model describes the emission of fluorescence from a radiating body in a multi-layer system. The sensor platforms were produced from a range of materials, glass, polymethyl methacrylate (PMMA), and a ridge waveguide platform, a type of slab waveguide, was made from UV curable sol-gel. The sensor platform fabrication and deposition of the sensor film is discussed in detail in Chapter 7.

6.2 Sensor Platform Configuration

All of the sensor platforms developed in this work are based on the generic configuration shown in Figure 6.1. Sensor films are deposited on top of each waveguide and are excited directly by a blue LED. Direct excitation is an important design feature of the sensor chip as it is considerably more efficient than evanescent-wave excitation. The fluorescence is emitted anisotropically from the sensor films, as will

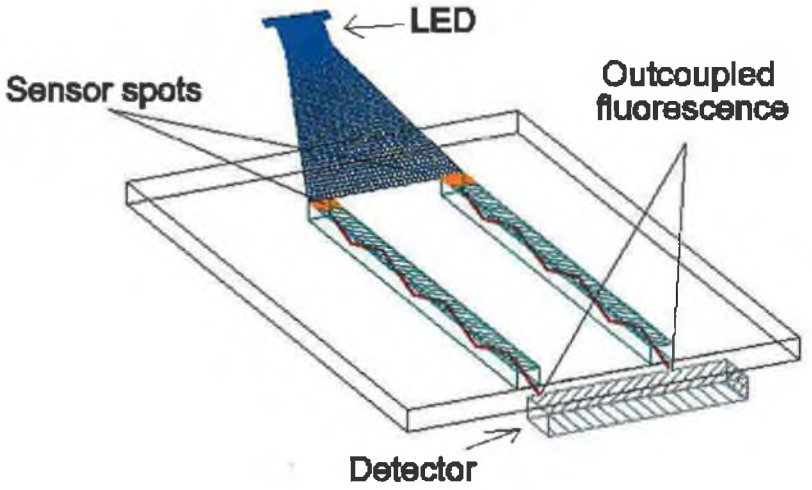

Figure 6.1: General sensor platform configuration.

be discussed in Section 6.3, and this is coupled efficiently into the waveguide and travels along its length. The fluorescence from the waveguides is detected at the endface. This sensor platform configuration is based on a US Patent developed by MacCraith et al [3]. All of the sensor platforms developed in this work are designed in this way. As can be seen in Figure 6.1, this configuration is inherently suitable for multi-analyte detection. Each channel can have its own excitation source, and can be easily adapted for the required number of analytes to be sensed.

6.3 Fluorescence Angular Profile Modelling

Studies by Polerecky et al [2] and others showed that the radiation of a molecule located in the vicinity of a dielectric substrate is highly anisotropic and the majority of the emission is directed into the substrate. This was developed into a full theoretical model of the anisotropic radiation of molecules located near an interface for systems employing multi-layer structures and thin luminescent films [1, 2]. In summary, the model shows that the angular distribution of radiation from a randomly orientated dipole located near an interface, is highly anisotropic and a large portion is radiated into the substrate itself which has a higher refractive index than the medium surrounding it, air. An image of the angular distribution of fluorescence from a dipole located at a glass substrate is shown in Figure 6.2.

Figure 6.2(a) shows a 3-dimensional picture of the emission and as the emission is axially symmetric it is possible to plot a 2-dimensional image of the fluorescence emission as shown in Figure 6.2(b). It has been shown that, a dipole located at a surface preferentially radiates into the higher refractive index substrate at angles close to the critical angle and the portion of intensity radiated into the environment is relatively small. Similarly, a configuration for the efficient detection of light emitted from a single molecule was published by Enderlein et al [4].

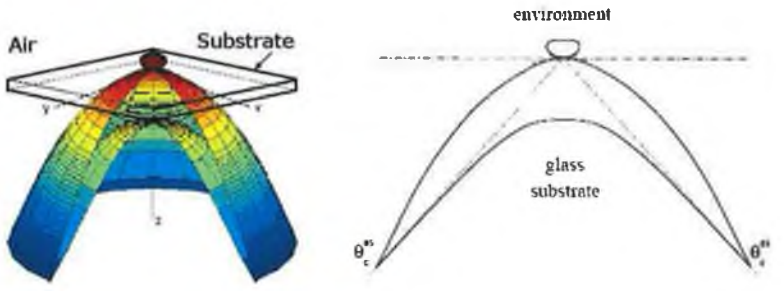

(a) 3D Profile (b) 2D Profile

Figure 6.2: Angular profile of fluorescence emission from a randomly orientated dipole at a glass interface surrounded by air.

The Polerecky model was adapted to deal with the sensor platforms used in the course of this work. The sensor platforms developed within this project consist of a sensor spot deposited on either a planar substrate, Figure 6.3, acting as a waveguide or a ridge waveguide, Figure 6.4. The fluorescence from the sensing film is coupled into the waveguide anisotropically. The coupled fluorescence exhibits a definite peak at a particular angle. The sensing platforms were developed so that they could act as waveguides. The refractive index values was chosen were so that the fluorescence signal would undergo total internal reflection. Thus, the fluorescence from the sensing film was captured and transmitted along the waveguide. The planar substrates, glass and PMMA, were surrounded by air, which facilitated total internal reflection. The support substrate most commonly employed for the fabrication of ridge waveguide structures is silicon due to its ability to be cleaved cleanly, thereby producing waveguide endfaces of optical quality. However, due to the high refractive index of silicon ($n \approx 3.4$) it is necessary to first deposit a buffer layer of lower refractive index, which acts as an interface for total internal reflection of light propagating along the guiding layer. The effect of altering the fabrication

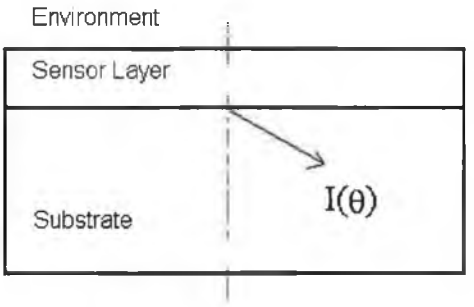

Figure 6.3: Planar waveguide.

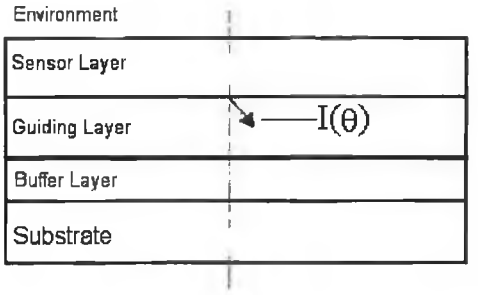

Figure 6.4: Ridge waveguide.

process and thus the layers in the waveguide structure was investigated using the model described above and the effects on the angular profile of emission and its intensity were investigated.

The optical sensors developed in this work were for oxygen, relative humidity and carbon dioxide. These sensor films were deposited as thin layers on the various sensor platforms developed. The fabrication and deposition of these sensor layers are described in more detail in Section 5.3. The difference in the angular profile of emission of fluorescence from the different sensor layers was investigated. This difference in emission was due to the different refractive indices of the sensor layers. The refractive indices of the different sensor layers were measured using a Metricon prism coupler and were found to be 1.433 for the oxygen film, 1.437 for the relative humidity film and 1.444 for the carbon dioxide film. These values were measured with an experimental error of ± 0.0005.

Initially the angular profile of fluorescence was investigated for the two planar waveguides, glass and PMMA, and then for UV curable sol-gel ridge waveguide configurations. The planar sensor platforms were used for all the optical sensor films whereas the UV curable ridge waveguide platform was investigated for an oxygen sensor layer only. The fluorescence was guided along the waveguides and detected in air at the endface. The angle of detection relative to the endface was then calculated for the different sensor configurations. By finding the angle of peak emission of fluorescence into the substrate the angle for detection of peak fluorescence intensity from the sensor platform can be found and used to design efficient detection systems for optical sensor platforms.

6.3.1 Planar waveguides

Figures 6.5(a), 6.5(b) and 6.5(c) show the angular profile of intensity of fluorescence coupled into the substrate for oxygen, relative humidity and carbon dioxide sensor layers deposited on the glass and PMMA substrates, respectively. The angle shown in these figures is within the substrate and is measured with respect to the normal at the waveguide sensor layer interface. As the critical angle for the layer substrate interface increases, the angle at which the peak intensity occurs is greater and it is shifted towards the higher critical angle. As the critical angle increases, the range of angles for which total internal reflection can occur in the waveguide decreases and therefore the intensity decreases. The critical angles for the different layer substrate interfaces are shown in Table 6.1.

It can also be seen that the intensity at the peak angle decreases with increasing sensor layer refractive index and decreasing substrate refractive index.

Substrate	Sensor Layer	Critical Angle
Glass	Oxygen	71.06°
Glass	Relative Humidity	71.54°
Glass	Carbon Dioxide	72.38°
PMMA	Oxygen	74.10°
PMMA	Relative Humidity	74.67°
PMMA	Carbon Dioxide	75.73°

Table 6.1: Critical angle for the sensor layer/substrate interface.

From Figures 6.6 and 6.7 we can see that the angle of peak intensity and the intensity of that peak increase with increasing sensor layer thickness. Up until the thickness reaches $2\mu m$, both the intensity and the angle always increase with thickness. After this, interference effects take over and while the intensity never decreases it does not increase in proportion to the thickness increase (Figure 6.7).

From these results it can be seen that increasing the sensor layer refractive index, or decreasing the substrate refractive index, will increase the angle of peak intensity of fluorescence in the substrate. As changing these refractive index values results in a smaller difference between the substrate and sensor layer, the intensity of the fluorescence in the substrate will be decreased. This decreases again results from an increase in the substrate/interface critical angle.

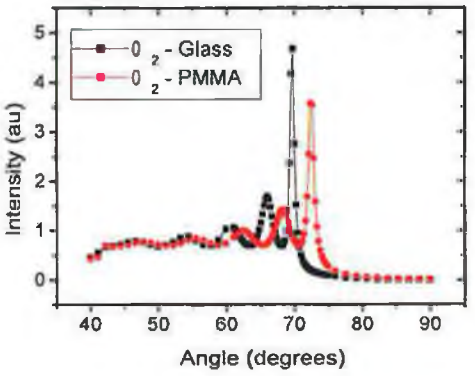

(a) Oxygen Sensor Layer

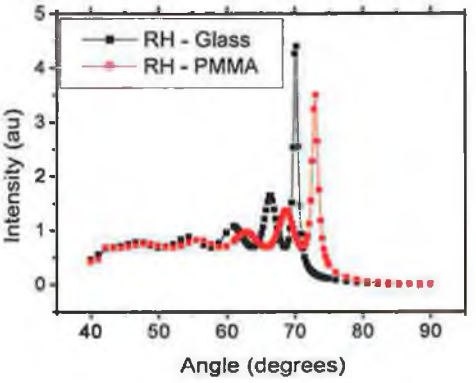

(b) Relative Humidity Sensor Layer

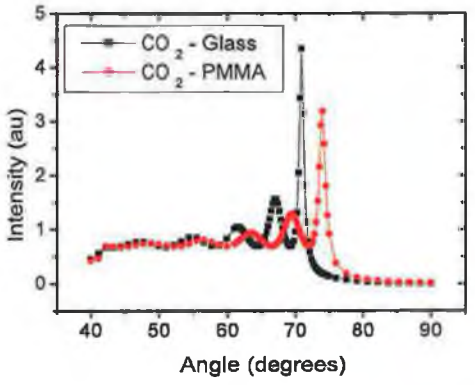

(c) Carbon Dioxide Sensor Layer

Figure 6.5: Angular profile of fluorescence intensity for different sensor layers.

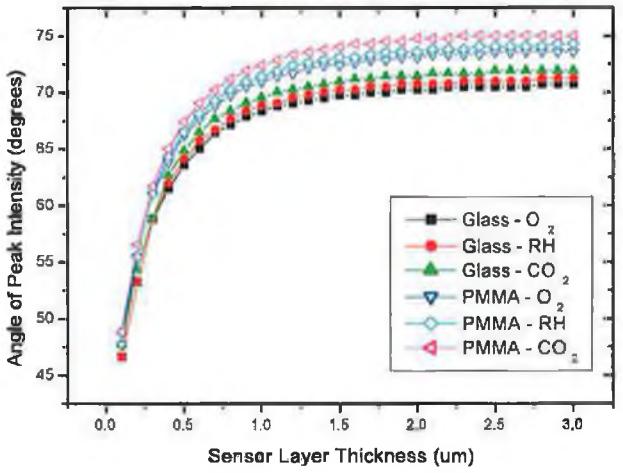

Figure 6.6: Angle at which peak fluorescence intensity occurs for sensor layer thickness between 1μm and 2μm.

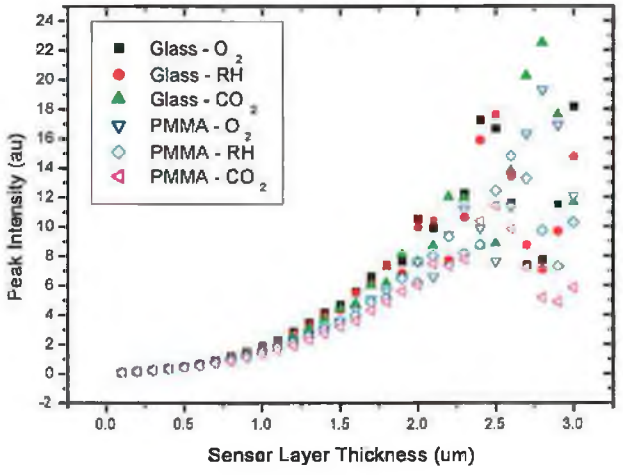

Figure 6.7: Peak fluorescence intensity for sensor layer thickness between 1μm and 2μm.

Detection Angles

Using the values for the angles of peak fluorescence intensity in the different sensor platforms and the Fresnel equations, Equations B.1- B.4 in Appendix B, the angle of detection in air at the endface, for sensor layer thicknesses between 1μm and 2μm is shown in Table 6.2. A diagram of where the relevant angles are measured is shown in Figure 6.8, where θ_1 is the angle of propagation in the waveguide as described in previous section, θ_2 is the angle in the waveguide endface/air interface, and θ is the angle of detection in air at the endface. In all cases the proportion of light transmitted through the substrate/air interface was calculated to be greater than 90%.

Substrate	Sensor	Angle of Detection in Air
Glass	O_2	31°-34°
Glass	RH	30°-33°
Glass	CO_2	29°-32°
PMMA	O_2	26°-29°
PMMA	RH	25°-28°
PMMA	CO_2	23°-27°

Table 6.2: Angle of detection of fluorescence in air at endface from sensor layer with thickness between t=1μm and t=2μm deposited on different substrates.

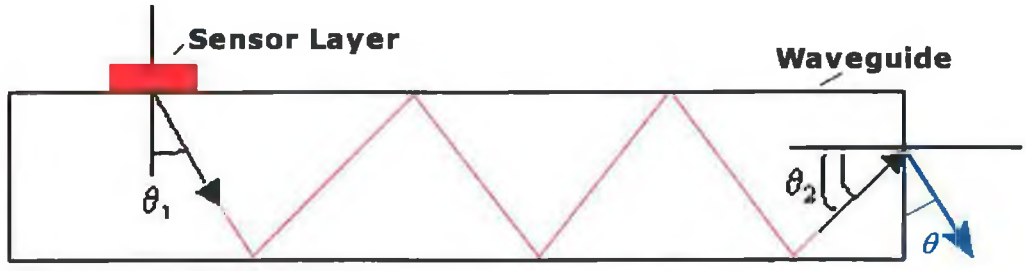

Figure 6.8: Angle of detection in air, θ at endface of waveguide.

These values can be incorporated into the experimental setup design for the different sensor platforms to gain optimum detection of the fluorescence captured into the waveguide.

6.3.2 UV curable ridge waveguides

Ridge waveguide sensor platforms were fabricated using UV curable sol-gel. The advantage of using sol-gel in the fabrication of waveguides is the ability to tailor the refractive index and thickness values of the different layers. These sensor platforms were initially developed using a method previously developed in our research group based mainly on direct photolithography of each waveguide platform. This method of waveguide fabrication will be described in more detail in Section 7.3.3. It was found that these waveguide platforms were not suitable for fluorescence-based optical sensor platforms and a second fabrication method based on the soft-lithography technique micromoulding in capillaries (MIMIC) was developed which gave an improved performance as a sensor platform. This method of developing sensor platforms is described in Section 7.3.4. The initial waveguide platform was found to be unsuitable due to the thickness and refractive index parameters of the different layers achieved using the defined fabrication method. These parameters are listed below, in Table 6.3, for both ridge waveguide fabrication methods.

Layer	R.I.	t(μm)
Environment	1	inf
Sensor Layer	1.433	1
Waveguiding Layer	1.5004	10
Buffer Layer	1.488	12

Table 6.3: Method1 - Initial

Layer	R.I.	t(μm)
Environment	1	inf
Sensor Layer	1.433	1
Waveguiding Layer	1.51	75
Buffer Layer	1.49	12

Table 6.4: Method2 - MIMIC

The angular profile of fluorescence for both sets of parameters is shown in Figure 6.9. The key differences between methods 1 and 2 is the waveguide thickness achievable and the difference in refractive index between the buffer and waveguiding layers. The value of the peak intensity of all the guided modes from the parameters from the MIMIC method is much greater then that for the initial method and there are many more couple modes in the waveguide from the MIMIC method. The graphs are shown at a similar scale to compare with the less intense modes from the initial waveguide fabrication method. The MIMIC graph shows an increase in the intensity of the modes due to the increase in the refractive index difference between the layers. The number of guided modes is also increased due to the increase in waveguide layer thickness.

The model for investigation of the angular profile of fluorescence emission and

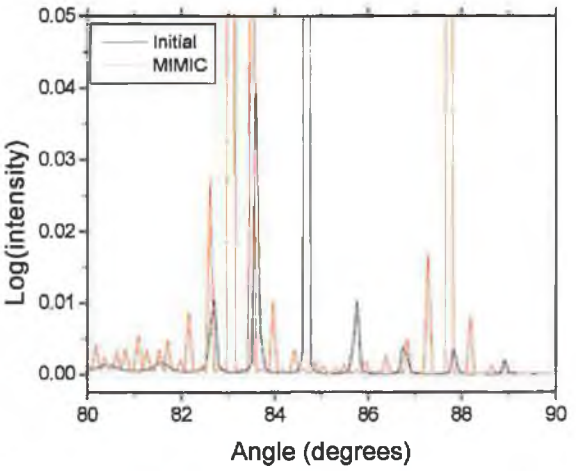

Figure 6.9: Angular profile of fluorescence intensity in substrate using both waveguide fabrication methods.

the intensity of that emission was adapted to investigate the effects of altering the refractive index and the thickness of the various layers present in the ridge waveguide sensor platform structure. The effect of changing the different parameters is summarised in Table 6.5. These parameters were changed within the limits of what is achievable with the current waveguide fabrication processes.

Layer	Parameter	Effect - Modes	Mode Intensity
Buffer	Refractive Index ⇓	Angle of modes decrease	Increase
Buffer	Thickness ⇑⇓	No Effect	No Effect
Waveguide	Refractive Index ⇑	Angle of modes decrease	Increase
Waveguide	Thickness ⇑	No. of modes increase	Increase
Sensor	Refractive Index ⇑	No Effect	Increase
Sensor	Thickness ⇑	No Effect	No Effect

Table 6.5: Effect of changing refractive index and thickness values for each of the layers.

Detection angles

As mentioned previously, The detection angle of the fluorescence from the endface of the waveguide in air can again be calculated using the Fresnel equations. These angles are calculated for both waveguide preparation methods using the angular position of the first and last guided mode in the waveguide to give a range of possible detection angles. These angular ranges for detection of fluorescence are shown in Table 6.6.

Substrate	Sensor	Angle of Detection in Air
UV Curable Waveguide - Initial	O_2	1.651° - 10.991°
UV Curable Waveguide - MIMIC	O_2	1.812° - 13.356°

Table 6.6: Angle of detection of fluorescence in air at endface from sensor layer deposited on UV curable waveguide.

These values can thus be incorporated into the experimental setup design for the different sensor platforms to gain optimum detection of the fluorescence captured into the waveguide.

6.4 Conclusion

This chapter describes the various sensor platforms used in this work. It describes how the fluorescence is emitted anisotropically from a sensor layer and how this is used to determine the optimal angle of detection from the endface of a waveguide platform. The effect of the differences in the two fabrication methods used for UV curable waveguides has been shown. The development of sensor platforms to suit the particular requirements of excitation and detection of fluorescence has also been described.

Bibliography

[1] L. Polerecky, J. Hamrle, and B. D. MacCraith. Theory of the radiation of dipoles placed within a multilayer system. *Applied Optics*, 39(22):3968–3977, 2000.

[2] L. Polerecky. *Optimisation of multimode waveguide platforms for optical chemical sensors.* Ph.D. Thesis, Dublin City University, 2002.

[3] B.D. MacCraith, M.J. Feldstein, and F.S. Ligler. Integrating multi-waveguide sensor. *US Patent No. US6137117*, US Navy, October 2000.

[4] J. Enderlein, T. Ruckstuhl, and S. Seeger. Highly efficient optical detection of surface-generated fluorescence. *Applied Optics*, 38(4):724–732, 1999.

Chapter 7

Sensor Platform Fabrication and Sensor Film Deposition

7.1 Introduction

Microfabrication is essential to much of modern science and technology. It can be found throughout society due to the large role it plays in optoelectronics and microelectronics. The patterning technology underpinning microfabrication is typically carried out using photolithography. While photolithography is the dominant and most developed technology, other micropatterning techniques can have advantages over it in particular situations. This chapter will deal with the range of microfabrication techniques used in the course of this work to develop sensor platforms and deposit sensor materials. Photolithography will be discussed along with soft lithography and a range of microfabrication techniques for polymer platform fabrication. The sensor platforms for this project were fabricated from two materials: UV curable sol-gel and polymers. The sensor platforms developed from these materials are described. Methods of depositing the sensor films onto the platforms were also developed and these methods are described in this chapter.

7.2 Soft Lithography

Soft lithography describes a range of microfabrication techniques developed primarily by George Whitesides and his group at Harvard University [1]. These techniques are based on the use of a patterned elastomer as a stamp, mould or mask to develop microstructures. The elastomer used is typically polydimethylsiloxane (PDMS),

which is commercially available as Sylgard 184 from Dow Corning. Soft lithography is a non-photolithographic approach which has the advantages of rapid prototyping and low-cost fabrication, thereby enabling mass-production. Soft lithography is suited to the patterning of non-planar substrates and has been developed as a range of methods to complement photolithography. Soft lithography can be used with any material which can become a solid through irradiation or thermal treatment. A wider range of materials can be used for this as photolithography is restricted to photoresists.

Three soft lithographic techniques have been used in the course of this work: microcontact printing, micromoulding in capillaries and microtransfer moulding. Each will now be described in detail. The range of applications for soft lithography in optoelectronics and microelectronics will also be discussed along with each particular technique.

7.2.1 Patterned elastomer fabrication

The basis of all of the soft lithographic techniques is the use of a patterned elastomer to make various stamps, moulds and masks. Taking any master made from a variety of techniques such as UV photolithography [2,3], UV laser writing [4], high-resolution printing [5] or direct machining [6], a liquid pre-polymer can be cast against it. The liquid pre-polymer is made up of a base and a curing agent. The pre-polymer is allowed to degas and both the master and pre-polymer are cured at an elevated temperature. The PDMS is allowed to reach ambient temperature and then can be removed from the master leaving the desired mould, mask or stamp structure fabricated. The fabrication of a PDMS mould is shown in Figure 7.1. The ratio of base to curing agent can be altered to change the rigidity of the film i.e. a larger amount of curing agent would lead to a less flexible film. The curing regime can be also be modified to suit the particular application. In the course of this work, the ratio of base to curing agent was maintained at 10:1 and the curing regime selected was 1 hour at 70°C. To enable easy removal of the PDMS mould from the master, a silanisation step can first be performed on the master to make it 'non-stick'. For silanisation, the template was placed in an atmosphere of the silane in a fumehood. The silane used in this work, when required, was trichloro(pefluorooctyl)silane. This was left for approximately 15 minutes and the template was then rinsed with acetone and dried at 70°C for 30 mins before use.

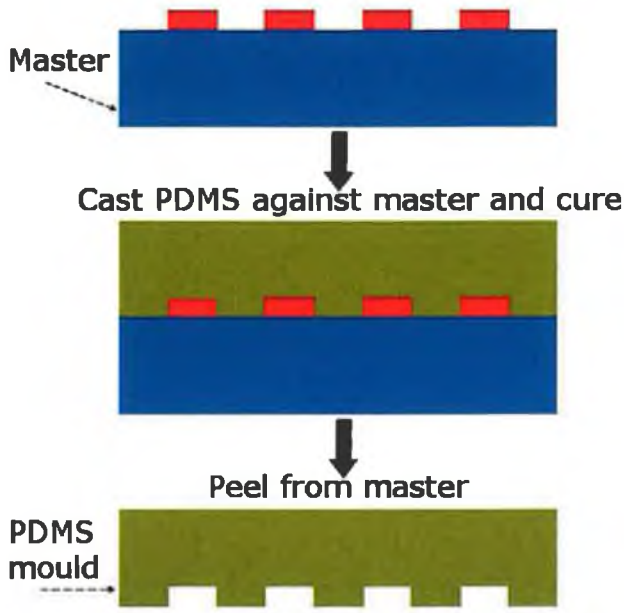

Figure 7.1: Fabrication of PDMS mould.

7.2.2 Microcontact printing - μCP

Microcontact printing (μCP), uses the relief pattern on a PDMS stamp to deposit molecules onto surfaces. The stamp is first placed in the solution to be deposited and then brought into contact with the substrate to be patterned. The PDMS stamp makes conformal contact with the surface and the molecules are directly transferred onto the surface from the stamp in a few seconds. PDMS also has chemical and physical properties important for the molecule transfer behaviour [7]. The principal of μCP is shown in Figure 7.2. μCP is a powerful deposition technique as patterns can be made on many substrates, with both flat and curved surfaces using a range of solutions. Repeated printing using the same or a combination of stamps can be used to produce multi-layer structures and complex patterns with different molecules.

Microcontact printing is currently being used extensively. Research is underway to develop μCP to a high resolution printing technique to rival photolithography [7]. Organic electronic devices such as transistors and inverter circuits have been fabricated in the drive for plastic electronic components [8–10]. Other work has been carried out on developing integrated optics using μCP [11].

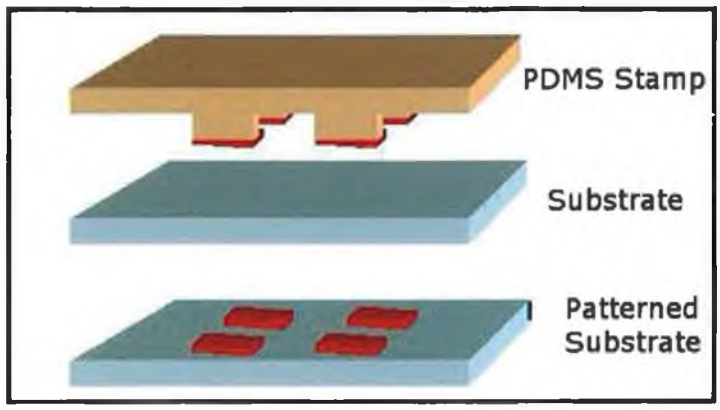

Figure 7.2: Principle of Microcontact Printing (μCP).

7.2.3 Micromoulding in capillaries - MIMIC

In MIMIC, a PDMS mould of a network of recessed channels is fabricated as described in Section 7.2.1. The ends of the moulds are cut off and it is placed on the surface of a substrate. A low-viscosity solution is placed at the entrance to the mould and fills the mould by capillary action. This process is illustrated in Figure 7.3. The solution can be any liquid which forms a solid using thermal treatment or irradiation. For example, in the case of the work described later in Section 7.3.4, a photopatternable sol-gel material was patterned using this technique. As PDMS is transparent in the UV and visible region, any material that can be polymerised in those spectral regions can be used. Once the structure has formed, the PDMS mould can then be removed from the support. This technique produces negative replicas of the patterns on the surface of the master with the resolution achieved in the fabricated structure determined by the PDMS mould. It is possible, using this technique, to manufacture free-standing structures. The structure can be formed on a solid support which is then removed by melting or dissolving or the structure can be manually removed from the master, for example by using tweezers.

The three constituent parts of the system used for MIMIC - the master, the support, and the liquid - must have certain characteristics. The master must be elastomeric, have a low surface free energy, and be unreactive towards the liquid. The master's elasticity is sufficient to allow its separation from the microstructures. As the PDMS master and the support adhere without applying external force, the process reproduces features in the surface of the master accurately. It is important

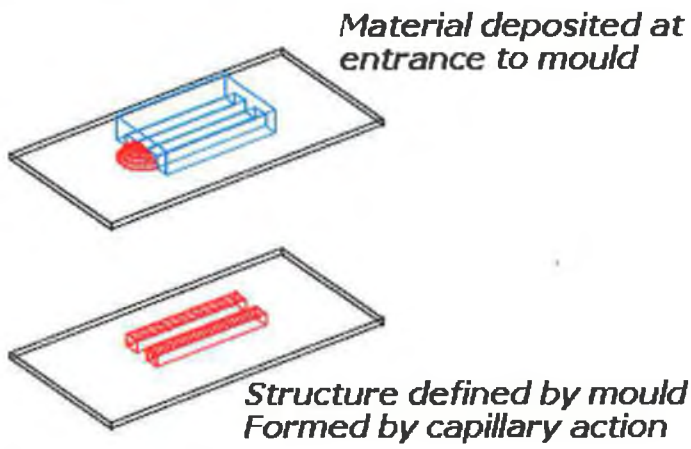

Figure 7.3: Principle of Micromoulding in Capillaries (MIMIC).

to ensure that the patterned structure adheres preferentially to the substrate rather than the mould. The liquid should have low viscosity, small volume changes on curing, and cross-link under achievable conditions [12].

Photolithography requires one exposure per structure; in MIMIC a single master can be produced (in many cases by a single photolithographic step) and used to make many PDMS moulds. Each mould can then be used repeatedly. This makes MIMIC an inexpensive, rapid production technique which can be carried out in any standard laboratory without the need for high-precision specialised instrumentation.

MIMIC has been used in both optics and electronics to fabricate field effect transistors [13]; ridge waveguides [14, 15]; and rectifier circuits [16].

7.2.4 Microtransfer moulding - μTM

In μTM, a thin layer of liquid is applied to the patterned surface of a PDMS mould. Any excess liquid is removed using a flat PDMS block or by blowing off with a stream of nitrogen. This filled mould is then brought into contact with the chosen substrate. The liquid is then cured to a solid using irradiation or heating. The PDMS mould is then carefully removed leaving the patterned structure on the substrate. This process is outlined in Figure 7.4. Unlike MIMIC, μTM can be used with any mould as the necessity to have interconnected channels is not required. Also as the moulds are not filled by capillary action, μTM is suitable

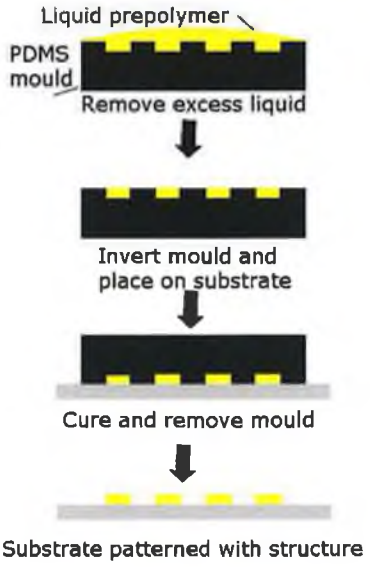

Figure 7.4: Principle of Microtransfer Moulding (μTM).

for the manufacture of larger devices. μTM can enables the production of three dimensional structures as microstructures can be formed layer by layer on nonplanar surfaces.

Microtransfer moulding can be used in a wide range of applications. Previous work has been carried out to fabricate optical waveguides [17], couplers [18], interferometers [19], diodes [20], and transistors [13,21].

7.3 Photocurable Sol-gel Waveguides

The first material used for sensor platform fabrication in this work was photocurable sol-gel. As described in Section 3.6, these are sols with a photoinitiator added. Two fabrication methods were used in the development of photocurable sol-gel ridge waveguide platforms - the first consisted mainly of photolithography and the second was a combination of photolithography and micromoulding in capillaries. UV-curable sol-gel was selected as the material due to several factors:

- Ability to create dense sol-gel structures of high optical quality
- Ease of refractive index modification of the material
- Relatively high film thickness obtainable

- High temperature annealing stage not necessary

Silicon is the usual choice of substrate for ridge waveguides as waveguides can be produced with optical quality endfaces due to the ability to cleave silicon cleanly eliminating the need for a polishing step. Silicon itself has a high refractive index (n≈3.4). In order to use silicon as a substrate for ridge waveguides, a buffer layer first needs to be deposited to enable the light propagate in the waveguide by total internal reflection. A schematic of the ridge waveguide structure is shown in Figure 7.5. Two sols were prepared in the fabrication of the platform, one to act as a buffer layer and the second to act as a (wave)guiding layer.

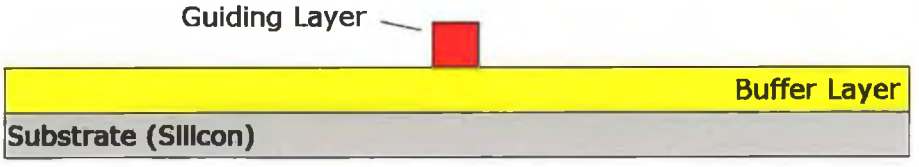

Figure 7.5: UV curable ridge waveguide sensor configuration.

7.3.1 Preparation of photocurable sol

The sol-gel waveguide fabrication procedure can be divided into five steps:

- Sol synthesis
- Deposition and stabilisation of buffer layer
- Deposition of guiding layer
- Waveguide structure printing
- Final stabilisation of structure

The sol synthesis has been described in detail elsewhere [15,22]. In summary, the guiding layer sol is synthesised by hydrolysis of methacryloxypropyltrimethoxysilane (MAPTMS). Methacrylic acid (MAA) and zirconium n-propoxide are mixed with the MAPTMS. Finally, a photoinitiator is added to enable photopolymerisation by UV irradiation at room temperature. The buffer layer is prepared in a similar manner without the addition of the zirconia complex, which is used in the

guiding layer to increase and tailor the refractive index. Both sols undergo the same process to stabilisation. They are first deposited and thermally treated. Next they are exposed to UV irradiation and a final thermal treatment is undergone. The deposition and UV irradation steps were particular to the fabrication method chosen.

7.3.2 Photolithography

Photolithography has been the chosen technique for microfabrication in optoelectronics and microelectronics [1]. Photolithography consists of transferring a pattern, described by a mask, onto a silicon wafer using a photoresist. A photoresist is a material which becomes polymerised when exposed to UV radiation, thus forming a cross-linked structure where exposed and leaving the unexposed parts to be removed. The photolithography process is illustrated in Figure 7.6.

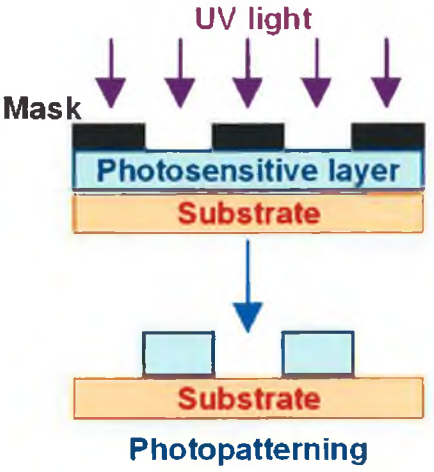

Figure 7.6: Photolithography.

7.3.3 Waveguide platform fabrication using photolithography

In this work, ridge waveguides were first fabricated using photolithography. The process undertaken is described in the flowchart in Figure 7.7. A buffer layer was deposited and processed. The deposition method of spin-coating is described in detail in Section 7.5.2. Both layers were deposited in a saturated isopropanol

atmosphere. Next the guiding layer was deposited and exposed to UV light, using a Karl Suss contact mask aligner, through a fixed mask which defined the waveguide structures. The unexposed parts of the guiding layer were washed away with IPA to give the waveguide structure which was then followed by a thermal treatment to harden the structure. A sample of the waveguide platforms produced in this way is shown in Figure 7.8. The waveguides developed using this method have a height of $\approx 12\mu$m and a width of $\approx 100\mu$m.

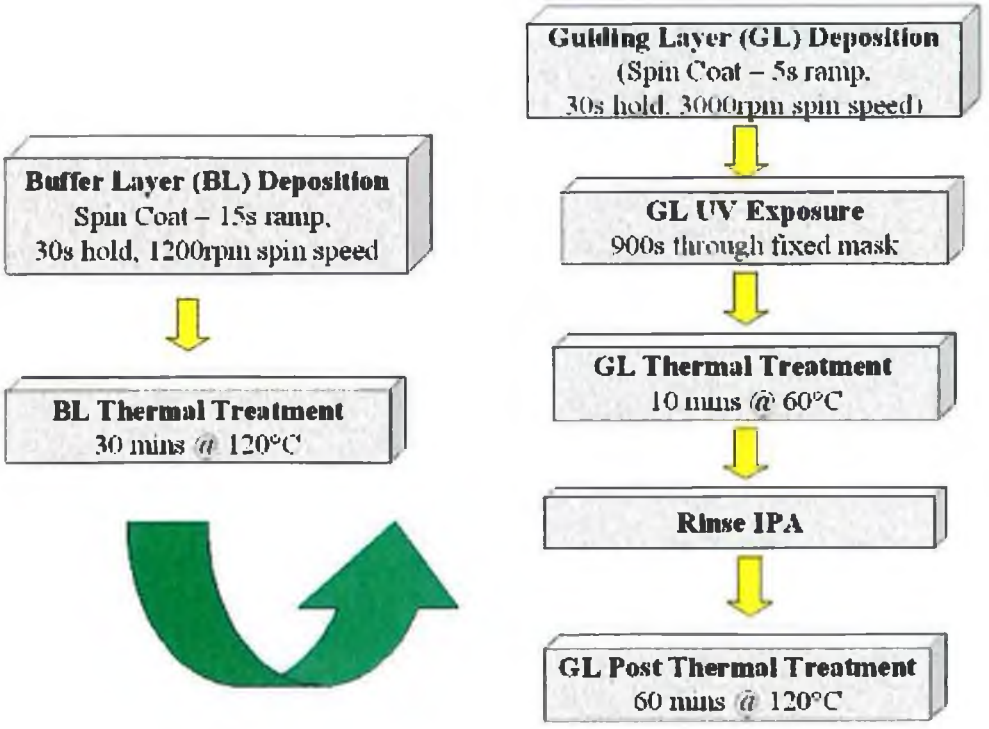

Figure 7.7: Photolithographic process for ridge waveguide fabrication.

7.3.4 Photocurable sol-gel waveguide fabrication using SU-8 photolithography and soft lithography

A problem encountered with the fabrication of UV-curable sol-gel waveguides with a combination of photolithography, thermal treatment and spin-coating was that the maximum thickness of the guiding layer achievable with this method was less than 15μm as this was the maximum thickness of the sol achieved using spin-coating. As the width of the waveguides, defined by the mask, was 100μm - this lead to coupling

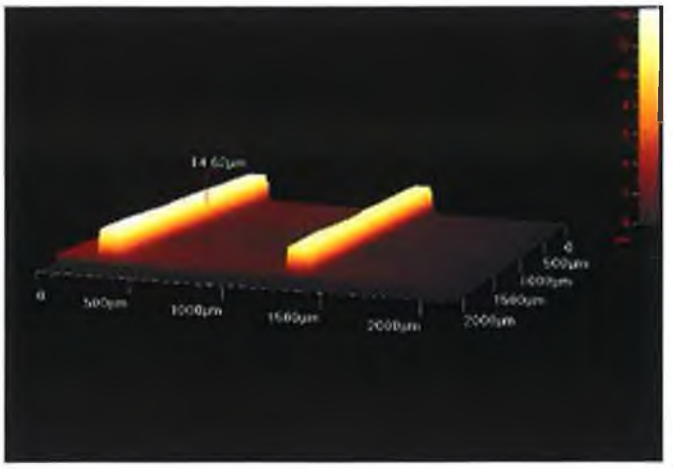

Figure 7.8: Sample of UV curable sol-gel ridge waveguides produced by photolithography.

losses in the waveguide as was described in Chapter 6. Other methods of fabrication of the waveguides were now investigated. The second chosen fabrication method involved the development of a waveguide master made from the photoresist SU-8 (Microchem, U.S.), which enabled the production of thicker layers. This master was used along with soft lithographic techniques to fabricate thicker waveguide structures. SU-8 is a photoresist which is now widely used for MEMS and μTAS applications. It has been applied to a broad range of areas including immobilisation of DNA [23], fabrication of embedded microchannels [24], optical waveguides for oxygen sensing [2] and as a mould for microelectroplating or a mask for plastic hot-embossing [3]. SU-8 is an epoxy-based photoresist designed for applications where a thick chemically and thermally stable master is required. Film thicknesses from 35μm to $<$ 200mm can be obtained, using the entire range of SU-8 resists, with a single deposition process [25].

An SU-8 layer, SU-8 2075 (Chestech, U.K.), was spin-coated onto a cleaned silicon wafer (Ramp Time 7s, Spin Speed 2200rpm, Hold Time 30s) and then a waveguide template was fabricated using a combination of thermal treatments and UV-exposure. The wafer was cleaned by immersing it in a sonicator which contained a solution of a standard widely available detergent and deionised water. The template was exposed to UV-irradiation through a fixed mask in a similar manner to before (Section 7.3.3). The unexposed SU-8 was removed through a development

step. The wafer was immersed in a sonicator containing a developer solution (EC Developer, Chestech, U.K.). The process parameters used in the fabrication of the SU-8 template are detailed in Table 7.1. These parameters were used to obtain a layer of approximately 100μm thickness. An image of a sample SU-8 waveguide template, taken by a Hitachi S-3000N scanning electron microscope, is shown in Figure 7.9. This waveguides template has waveguide features which have an average width of 100μm$\pm$1μm and a height of 95μm$\pm$2μm. Further modification and tailoring of the spin-coating parameters should enable a height of 100μm to be obtained.

Process	Temperature (°C)	Time
Soft Bake	95	20 mins
UV Exposure	n/a	90s
Hard Bake	95	15 mins
Development Time	n/a	10 mins

Table 7.1: Fabrication parameters for SU-8 master.

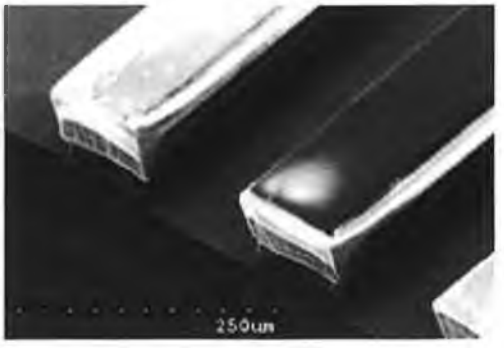

Figure 7.9: SEM image of sample SU-8 waveguide master.

This waveguide template was then used in conjunction with the soft lithography technique MIMIC (described in Section 7.2.3) to produce a waveguide-based sensor platform. An overview of the fabrication process is shown in Figure 7.10. A PDMS mould is made from the SU-8 master, which had undergone a silanisation step as described in Section 7.2.1. A buffer layer of UV-curable sol is deposited on a clean silicon wafer in a similar manner to that described in Section 7.3.3. The PDMS mould is cut open and placed in contact with the buffer layer and a drop

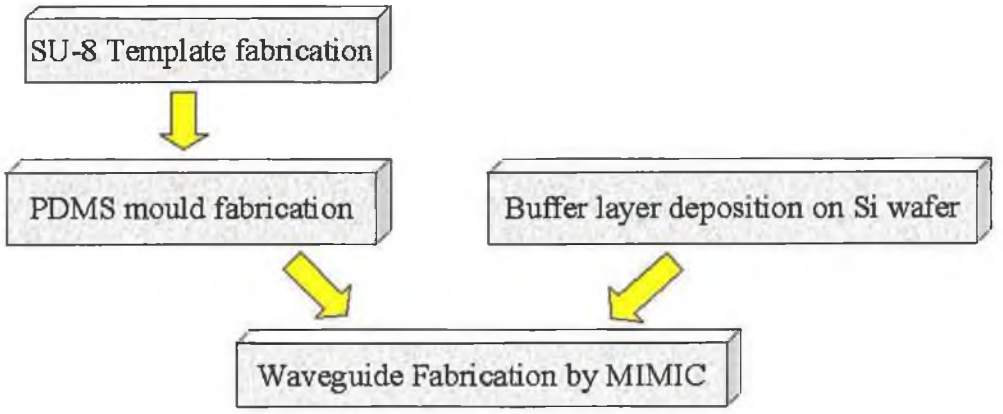

Figure 7.10: Overview of fabrication process of UV-curable sol-gel waveguides using an SU-8 waveguide master and micromoulding in capillaries.

of the guiding layer sol is placed at the entrance to the mould. It fills by capillary action and then the guiding layer is exposed to UV irradiation through the PDMS mould which is UV transparent. The sol is exposed overnight to radiation from a broadband UV source (UV Light Technology Ltd., U.K.). After exposure the structure undergoes a thermal cross-linking treatment (30 mins @ 80°C) before the PDMS mould is removed leaving the waveguide structure. The samples were then cleaved to give optical quality endfaces. To promote the filling of the mould by capillary action the mould is first soaked in the solvent, which is present in the sol, in this case 2-propanol and dried with nitrogen before filling. This process has many advantages over previous work to fabricate optical waveguides from SU-8 for oxygen sensing [2]. The fabrication procedure consists of fewer complex steps without the need for aggressive chemical treatments.

7.4 Plastic Platforms

The major trends driving optical chemical sensor technology are miniaturisation, multi-parameter sensing and mass-production of low-cost disposable sensors. Plastic platforms have been a major force in recent sensor development as they lend themselves to low-cost rapid-prototyping fabrication techniques. Plastic platforms are also suitable for multi-analyte sensing as they can easily be expanded to have multiple channels or layers. Plastic platforms can be used in place of glass platforms as they are easier, and therefore less expensive, to fabricate than glass. There is now a large range of optical quality plastics available with different properties and in particular different refractive indices. The surface properties of these plastic substrates - wettability; adhesion; surface adsorption; surface reactivity - can be altered using a variety of surface chemistries to optimise the plastic substrate for a specific chemical or biological application.

The initial polymer platform used is shown in Figure 7.11(a). This design was chosen to sense multiple analytes or multiple channels of the same analyte using a single detector. Initially the detector used was the linear image sensor and the channel separation was chosen to suit this. The second PMMA platform was designed for use with multiple photodiodes and had a larger channel separation. This platform is shown in Figure 7.11(b). The use of different detectors is discussed in more detail in Chapter 8.

(a) Single detector (b) Multiple detectors

Figure 7.11: Initial PMMA platform designs for use with both a single detector and multiple detectors.

The third PMMA sensor platform was designed to enable phase-based measurements of multiple channels using a single detector which will be described in Section 8.3.3. A platform was developed whereby two independent channels could be excited separately but be detected separately at the same point using a single

detector. The design of this platform is shown in Figure 7.12, including where the optical sensor films are deposited.

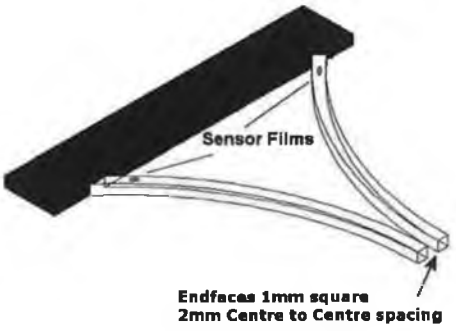

Figure 7.12: Curved PMMA sensor platform design.

Microfabrication technologies originate from the microelectronics industry, the devices are most widely made on silicon wafers even though glass, plastics and many other substrate are in use. Microfabricated devices include for example, integrated circuits, microsensors, inkjet nozzles and flat panel displays. The broad general term microfabrication encompasses many techniques including micromachining, semiconductor processessing, microelectronic fabrication, semiconductor fabrication, MEMS fabrication and integrated circuit technology.Traditional machining techniques have been scaled from the millimeter size range to micrometer range, for example the technique of laser ablation. Microfabrication is actually a collection of technologies which are utilized in making microdevices. Some of them were not originally connected to manufacturing including lithography, etching, stamping and embossing techniques [6].

The range of microfabrication techniques based on a rubber patterning element, called soft lithography, have previously been discussed in Section 7.2. These were discussed separately due to their large range of applications and the combination of them with photolithographic techniques. Some of the microfabrication techniques discussed in this section are direct machining techniques - therefore structures can be made directly or masks fabricated to make a range of structures. The polymer microfabrication techniques used in the course of this work for the development of our PMMA sensor platform are now described in turn.

7.4.1 Micro-milling

Micro-milling can be used to create U or square shaped channels in a range of polymers and metals. The tool sizes range from 100μm to 3mm diameter. Micro-milling is capable of directly machining pieces and can be used to directly fabricate a prototype or to create a master which can be used for replication techniques. Pieces to be fabricated can be designed using CAD software which can be inputted to control the micro-miller. This fabrication method did not produce platforms of sufficient optical quality to be used in this work due to it being a mechanical process and an imprint of the tool path is left in the piece being milled.

7.4.2 Laser ablation

Laser ablation can be used to create V shaped channels in polymers. The laser ablation system (Micromaster Turnkey System; Optec, Belgium), which was available for this work, can be used in conjunction with either a CO_2 laser or a KrF excimer laser. The choice of laser is dependent on the substrate being used. This method allows for rapid prototyping and is capable of creating points, lines and arcs on polymer substrates. The design patterned using the laser ablation can be imported from CAD software.

This technique was used for the fabrication of the majority of PMMA platforms in this work. The laser used in this case was the CO_2 laser. By varying the fabrication parameters, platforms of good optical quality could be obtained.

7.4.3 Micro-injection moulding

Injection moulding consists of heating polymer pellets until they melt and the liquid is then pushed into a mould. When the injection of the polymer into the mould is complete the polymer is allowed to cool and solidify. The mould is then opened and the polymer chip is ejected from the machine. This process can be cycled to produce a large volume of polymer chips. This tool injects molten polymer into a master to create a negative of that master. The depth of various structures is then volume dependent. For the micro-injection moulder (Babyplast 6/10; Chronoplast, Spain.), which was available for this work, the maximum footprint of any piece was 40mm x 40mm.

This technique was found not to be suitable for the majority of the early PMMA

platform designs. This was due to the length of the narrow channels on the platforms which could not be pushed out successfully using the ejector pins.

7.4.4 Hot embossing

Hot embossing is used for planar polymer replication. The system available for this work (HEX02; Jenoptik, Germany) is used to stamp print a master into a polymer. The polymer is heated to its glass transition temperature and the master pressed to create its negative on the polymer. In contrast to the injection moulder, the hot embosser is only suited to planar master replication due to the stress induced by the displaced polymer on the tool. Lithographic techniques are normally used for master creation for embossing with feature sizes documented in the sub micron range.

Hot embossing was not used in the chip development process as direct fabrication techniques, which did not require the use of a mask, were used while the chip design was being modified and improved.

7.5 Thin Film Deposition

Several methods of depositing thin films onto the various substrates used in the course of this work were investigated. While some of the standard techniques were used successfully and reproducibly when standard planar substrates were used, these were not suitable for coating the other substrates used in the course of this work. Thin films were deposited in the course of this work for both sensor platform fabrication and also for sensor film deposition.

7.5.1 Dip-coating

Dip-coating is an often used deposition method which involves vertical withdrawal of a substrate from a reservoir of the solution to be deposited at a constant speed. Film thickness is governed by the competition of several forces including gravity and capillary forces. The final thickness of the film and its uniformity are influenced by environmental factors such as the atmosphere surrounding the sample and flow conditions in the solution. A typical dip-coating apparatus, which was used in this work, consists of a holder for the solution to be deposited, usually a vial or a beaker, and a holder to hold the substrate vertically. One of these holders remains

stationary while the other is moved at a constant speed under either computer or mechanical control.

The dip-coating process can be divided into five distinct stages - immersion, start-up, deposition and drainage, drainage, and finally evaporation, as shown in Figure 7.13. The first three stages occur in sequence, the third and fourth occur simultaneously while the fifth stage, the evaporation, occurs throughout the whole process.

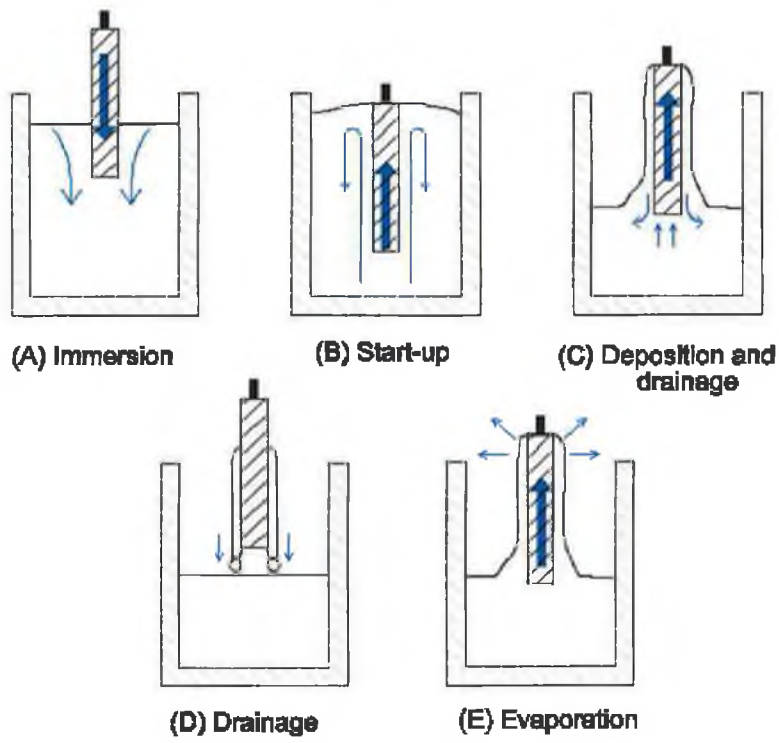

Figure 7.13: Steps involved in the dip-coating process [26].

As the sample is immersed in the liquid and withdrawn, the inner layer of deposited liquid moves in tandem with the substrate while the outer layer returns to the container. The film thickness is related to the position of the dividing border between the upward and the downward moving layers. The position of this border is determined by a number of competing forces. These are [27]:

1. Viscous drag upward on the liquid by the relative movement of the substrate and solution

2. Force of gravity
3. Resultant force of surface tension in the concavely curved meniscus
4. Inertial force of the boundary layer liquid arriving at the deposition region
5. Surface tension gradient
6. The disjoining or conjoining pressure

The relationship between all these forces and the film thickness is shown below in Equation 7.1

$$t = 0.94\left[\frac{\eta U}{\gamma}\right]^{1/6}\left[\frac{\eta U}{\rho g}\right]^{1/2} \tag{7.1}$$

where

- t is the film thickness
- η is the viscosity of the liquid
- U is the substrate withdrawal speed
- γ is the liquid-vapour surface tension
- ρ is the density of the liquid
- g is the acceleration due to gravity

From Equation 7.1, it can clearly be seen that, for a fixed set of parameters, as the speed of withdrawal of the substrate is increased, the thickness of the film also increases. In the course of this work, sol-gel sensor films for oxygen, carbon dioxide and relative humidity along with a polymer-based humidity sensor film were deposited onto planar glass, silicon and PMMA substrates using dip-coating. The substrate withdrawal speed was maintained at 3mm/s for all samples. Dip-coating in a dry environment (saturated with dry nitrogen) leads to the production of more uniform sensor films. Dip-coating is a successful method for reproducibly depositing thin films on planar substrates. If the deposition is only required on one side of the substrate, the second side can be masked before coating. The dip-coating process is not suitable for non-planar substrates or for selective deposition at a precise location on a substrate.

7.5.2 Spin-coating

Spin-coating is a method of reproducibly depositing thin films of a liquid onto a substrate. It is an economical deposition method as it only requires a small volume to be dropped in the centre of the substrate initially. This deposition method is most suited to circular substrates. It also allows for coating on a single side of a substrate without having to mask off the other side. During the course of this work, spin-coating was used to deposit layers of UV-curable sols onto silicon substrates and also in the fabrication of SU-8 masters for soft lithography.

Spin-coating can be broken down into four distinct stages [28]:

1. Deposition
2. Spin-up
3. Spin-off
4. Evaporation

The first three stages can be seen to happen sequentially with the coating solution first being deposited on the substrate and then being spread across and off the substrate due to the centrifugal force, while the evaporation stage occurs throughout the process as the solvent evaporates from the solution [29]. The first stage involves the deposition of the solution onto the substrate to be coated. For many solutions, including the UV curable sols used in the course of this work, the solution is deposited onto the substrate after being passed through a micron-sized filter to eliminate any particles that may be present in solution and cause non-uniformity in the final spin-coated layer. The spin-coating process is programmed by setting a final speed, a ramp time to get to that speed and a hold time when the maximum speed is reached. This set of parameters can be repeated. The second stage, spin-up, is when the substrate is reaching its maximum speed. During this time the centrifugal forces present force the liquid to flow radially outwards. In the spin-off stage, the substrate is spinning at a constant speed and the viscous forces dominate the fluid thinning behaviour. Any excess of solution flows to the edge of the substrate and leaves as droplets. As the film begins to thin, the rate of exit of the solution from the substrate as droplets decreases as the non-volatile components increase which in turn increase the viscosity. The fourth stage, evaporation - which has been going on throughout the process - dominates as the main source of thinning.

After these stages the film can undergo a heat treatment to evaporate any remaining solvent (used in the case of the UV curable sols, Section 7.3.3) or the film may go on to other processing steps such as UV-exposure and development (as used in the case of the SU-8 photoresist, Section 7.3.4.) The spin-coating process is mainly influenced by two factors: 1) the physics of fluid flow on a planar spinning substrate, and 2) the airflow above the substrate as this most influences the rate of evaporation of the solution. Spin-coating is a method for producing uniform films as the film tends to become uniform during spin-off and then remain uniform due to the balancing of the two main forces affecting fluid flow on the planar substrate. The viscous force which acts radially inwards balances the centrifugal force which acts radially outwards spreading the solution over the substrate [30]. This process is illustrated in Figure 7.14.

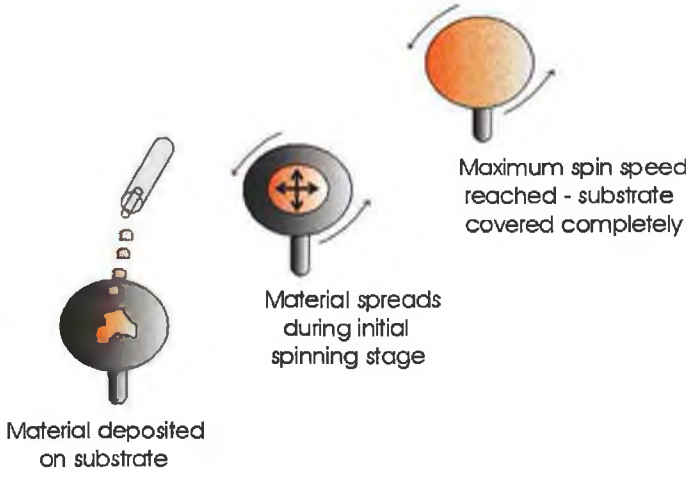

Figure 7.14: Steps involved in the spin-coating process [4].

Spin-coating was used in the course of this work for sensor platform development. It was not used as a method for sensor film deposition as it was unsuitable for non-planar substrates and all planar substrates had sensor films deposited on them by dip-coating.

7.5.3 Microcontact printing

Microcontact printing is a rapid prototyping technique that has been employed extensively in this work for the deposition of sensor films on non-planar substrates.

The technique of microcontact printing was described in detail in Section 7.2.2. In brief, a PDMS stamp - fabricated to suitable dimensions for the particular substrate being printed - was inked with the sensor solution. This was then brought into contact with the substrate leaving the sensor film deposited on top of the substrate. This technique was used for printing the various sensor films on PMMA sensor platforms and on top of UV-curable sol-gel ridge waveguides.

7.5.4 Pin-printing

The final sensor film deposition technique used in the course of this work was pin-printing. This involved the used of an array printing system (Omnigrid Micro; Genomic Solutions, U.K.) to deposit precisely defined small volumes of the sensor solution onto a range of substrates. The printer is shown in Figure 7.15. The printer is designed to fill a pin with the solution from a well in either a 96 or 384 well microtitre plate and print an array of spots on a substrate using this solution. These printers were designed for, and initially used in, the area of DNA microarraying for printing large arrays on planar glass substrates [31–33]. Recent work has shown they can also successfully be used in the field of sensor development to print on a range of non-planar substrates [15, 34, 35].

Figure 7.15: Genomic Solutions array printing system used for deposition of sensor films.

The pins used were "stealth pins" (SMP3; Telechem, U.S) which contained a narrow uptake channel in the middle of the pin which held the solution before

Figure 7.16: Pin printing mechanism.

printing. The printing mechanism used is shown in Figure 7.16. The pins have flat tips which allow the formation of a drop of printing solution on the bottom of the pin from the uptake channel. The pin is then brought close to the substrate so the the drop from the end of the pin is transferred to the substrate. The pin does not come into direct contact with the substrate. Each step in the printing process, including the washing and drying steps, are user programmable which enables the setting of a range of parameters for reproducible spot deposition. This allows automated printing for a pre-defined programme. Printing parameters such as time in well while filling pin, speed of pin movement, length of time for pin in contact with substrate, and humidity, influence the final dimensions of the printed sensor film and the number of spots that can be achieved from each fill of the pin.

Pin-printing was used as a deposition technique as it enabled selective printing at precise locations on a sensor platform. Both planar and non-planar substrates can be used as the arraying system has z-axis control as well as x- and y-axis control. It was used to print on the UV-curable sol-gel waveguides and also to deposit different sensor films on a series of polymer sensor channels.

7.6 Conclusion

The broad range of microfabrication techniques used in the course of this work for the fabrication of sensor platforms have been described in detail. Photolithography, soft lithography and other polymer processing techniques have been outlined and their used described in platform fabrication. The various methods of depositing sensor films onto sensor platforms have also been described.

Bibliography

[1] Y. N. Xia and G. M. Whitesides. Soft lithography. *Angewandte Chemie-International Edition*, 37(5):551–575, 1998.

[2] D. A. Chang-Yen and B. K. Gale. An integrated optical oxygen sensor fabricated using rapid prototyping techniques. *Lab On A Chip*, 3:297–301, 2003.

[3] J. Zhang, K. L. Tan, and H. Q. Gong. Characterization of the polymerization of SU-8 photoresist and its applications in micro-electro-mechanical systems (MEMS). *Polymer Testing*, 20(6):693–701, 2001.

[4] C.S. Burke. *Development of microfabricated optical chemical sensor platforms using polymer processing technology.* Ph.D. Thesis, Dublin City University, 2004.

[5] D. C. Duffy, J. C. McDonald, O. J. A. Schueller, and G. M. Whitesides. Rapid prototyping of microfluidic systems in poly(dimethylsiloxane). *Analytical Chemistry*, 70(23):4974–4984, 1998.

[6] M. Madou. *Fundamentals of microfabrication.* CRC Press, Florida, 1997.

[7] B. Michel, A. Bernard, A. Bietsch, E. Delamarche, M. Geissler, D. Juncker, H. Kind, J. P. Renault, H. Rothuizen, H. Schmid, P. Schmidt-Winkel, R. Stutz, and H. Wolf. Printing meets lithography: Soft approaches to high-resolution printing. *Ibm Journal of Research and Development*, 45(5):697–719, 2001.

[8] Z. N. Bao, V. Kuck, J. A. Rogers, and M. A. Paczkowski. Silsesquioxane resins as high-performance solution processible dielectric materials for organic transistor applications. *Advanced Functional Materials*, 12(8):526–531, 2002.

[9] J. Tate, J. A. Rogers, C. D. W. Jones, B. Vyas, D. W. Murphy, W. J. Li, Z. A. Bao, R. E. Slusher, A. Dodabalapur, and H. E. Katz. Anodization and microcontact printing on electroless silver: Solution-based fabrication procedures

for low-voltage electronic systems with organic active components. *Langmuir*, 16(14):6054–6060, 2000.

[10] J. A. Rogers, Z. N. Bao, A. Dodabalapur, and A. Makhija. Organic smart pixels and complementary inverter circuits formed on plastic substrates by casting and rubber stamping. *IEEE Electron Device Letters*, 21(3):100–103, 2000.

[11] J. A. Rogers, Z. Bao, M. Meier, A. Dodabalapur, O. J. A. Schueller, and G. M. Whitesides. Printing, molding, and near-field photolithographic methods for patterning organic lasers, smart pixels and simple circuits. *Synthetic Metals*, 115(1-3):5–11, 2000.

[12] E. Kim, Y. N. Xia, and G. M. Whitesides. Micromolding in capillaries: Applications in materials science. *Journal of the American Chemical Society*, 118(24):5722–5731, 1996.

[13] J. M. Hu, R. G. Beck, T. Deng, R. M. Westervelt, K. D. Maranowski, A. C. Gossard, and G. M. Whitesides. Using soft lithography to fabricate GaAs/AlGaAs heterostructure field effect transistors. *Applied Physics Letters*, 71(14):2020–2022, 1997.

[14] X. M. Zhao, A. Stoddart, S. P. Smith, E. Kim, Y. Xia, M. Prentiss, and G. M. Whitesides. Fabrication of single-mode polymeric waveguides using micromolding in capillaries. *Advanced Materials*, 8(5):420, 1996.

[15] C. S. Burke, O. McGaughey, J. M. Sabattié, H. Barry, A. K. McEvoy, C. McDonagh, and B. D. MacCraith. Development of an integrated optic oxygen sensor using a novel, generic platform. *Analyst*, 130(1):41–45, 2005.

[16] T. Deng, L. B. Goetting, J. M. Hu, and G. M. Whitesides. Microfabrication of half-wave rectifier circuits using soft lithography. *Sensors and Actuators A: Physical*, 75(1):60–64, 1999.

[17] T. Matsui, K. Komatsu, O. Sugihara, and T. Kaino. Simple process for fabricating a monolithic polymer optical waveguide. *Optics Letters*, 30(9):970–972, 2005.

[18] X. M. Zhao, S. P. Smith, S. J. Wadman, G. M. Whitesides, and M. Prentiss. Demonstration of waveguide couplers fabricated using microtransfer molding. *Applied Physics Letters*, 71(8):1017–1019, 1997.

[19] Y. N. Xia and G. M. Whitesides. Soft lithography. *Annual Review of Materials Science*, 28:153–184, 1998.

[20] J. M. Hu, T. Deng, R. G. Beck, R. M. Westervelt, and G. M. Whitesides. Fabrication of arrays of schottky diodes using microtransfer molding. *Sensors and Actuators A: Physical*, 75(1):65–69, 1999.

[21] N. L. Jeon, J. M. Hu, G. M. Whitesides, M. K. Erhardt, and R. G. Nuzzo. Fabrication of silicon mosfets using soft lithography. *Advanced Materials*, 10(17):1466–1469, 1998.

[22] M. Oubaha, M. Smaihi, P. Etienne, P. Coudray, and Y. Moreau. Spectroscopic characterization of intrinsic losses in an organic-inorganic hybrid waveguide synthesized by the sol-gel process. *Journal of Non-Crystalline Solids*, 318(3):305–313, 2003.

[23] R. Marie, S. Schmid, A. Johansson, L. Ejsing, M. Nordstrom, D. Hafliger, C. B. Christensen, A. Boisen, and M. Dufva. Immobilisation of DNA to polymerised SU-8 photoresist. *Biosensors and Bioelectronics*, 21(7):1327–1332, 2006.

[24] Y.-J. Chuang, F.-G. Tseng, J.-H. Cheng, and W.-K. Lin. A novel fabrication method of embedded micro-channels by using SU-8 thick-film photoresists. *Sensors and Actuators A: Physical*, 103(1-2):64–69, 2003.

[25] http://www.chestech.co.uk/2035-2100datasheet.pdf. 2006.

[26] L. E. Scriven. Physics and applications of dip coating and spin coating. *Material Research Sociey Symposium Proceedings*, 121:717–729, 1988.

[27] C.J. Brinker and G.W. Scherer. *Sol-gel science : the physics and chemistry of sol-gel processing*. Academic Press, New York, 1990.

[28] D. E. Bornside, C. W. Macosko, and L. E. Scriven. On the modeling of spin coating. *Journal of Imaging Technology*, 13(4):122–130, 1987.

[29] R. K. Yonkoski and D. S. Soane. Model for spin coating in microelectronic applications. *Journal of Applied Physics*, 72(2):725–740, 1992.

[30] B. G. Higgins. Film flow on a rotating-disk. *Physics of Fluids*, 29(11):3522–3529, 1986.

[31] B. Lemieux, A. Aharoni, and M. Schena. Overview of DNA chip technology. *Molecular Breeding*, 4(4):277–289, 1998.

[32] V. G. Cheung, M. Morley, F. Aguilar, A. Massimi, R. Kucherlapati, and G. Childs. Making and reading microarrays. *Nature Genetics*, 21:15–19, 1999.

[33] J. Ziauddin and D. M. Sabatini. Microarrays of cells expressing defined cDNAs. *Nature*, 411(6833):107–110, 2001.

[34] E. J. Cho and F. V. Bright. Integrated chemical sensor array platform based on a light emitting diode, xerogel-derived sensor elements, and high-speed pin printing. *Analytica Chimica Acta*, 470(1):101–110, 2002.

[35] W. G. Holthoff, E. C. Tehan, R. M. Bukowski, N. Kent, B. D. MacCraith, and F. V. Bright. Radioluminescent light source for the development of optical sensor arrays. *Analytical Chemistry*, 77(2):718–723, 2005.

Chapter 8

Experimental Characterisation Systems

8.1 Introduction

The sensors developed in this work are based on the changes in fluorescence of an indicator dye when exposed to a particular analyte. In this chapter, the various systems used to monitor the sensor response as a function of fluorescence intensity, fluorescence lifetime (or the related phase angle) are described and illustrated. The basic components of one such system include an excitation source, sensor film deposited on a substrate, optical filters and a detector. Both the excitation source and detector are operated using control electronics. An example configuration for monitoring changes in fluorescence is shown in Figure 8.1. This configuration is described in more detail in Section 6.2.

The excitation source is selected so that its emission spectrum overlaps with the excitation spectrum of the indicator dye and the excitation induces fluorescence in the sensor material. It is important to prevent any excitation light from reaching the detector, and this is achieved by optical filtering. Thus it is desirable for the excitation source to be sufficiently spectrally separated from the sensor emission so that the excitation light can be filtered out and prevented from reaching the detector without reducing the amount of fluorescence detected. Due to the multi-analyte nature of the work involved in this project the choice of excitation source and indicator dye for each sensor was made to ensure compatibility with the other sensors developed. The operation of a commercial spectrofluorometer used to measure both excitation and emission spectra of the indicator dyes is described. To

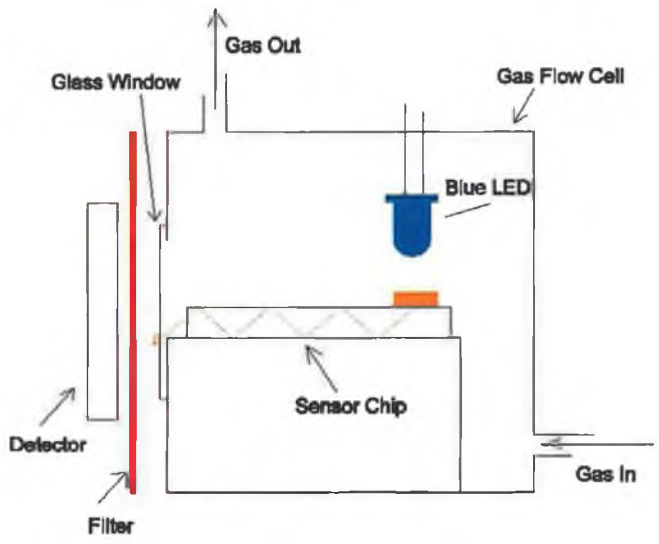

Figure 8.1: Sample configuration for detection of fluorescence.

characterise the response of any sensor film to a particular analyte gas, the film must be enclosed in a sealed gas flow cell into which precise gas concentrations of the analyte can be delivered. The development of characterisation systems for the various sensors developed is also described in this chapter.

This chapter describes the development of the fluorescence detection system from an initial intensity-based to a lifetime-based system along with the associated experimental systems to measure the fluorescent properties of a material. Systems for lab-based characterisation of the sensor films are also discussed.

8.2 Intensity-based Systems

For both the intensity-based systems and the lifetime-based systems, (Section 8.3), used in the course of this work a flow cell with the configuration shown in Figure 8.1 has been used for sensor characterisation. The flow cell also contains a thermistor and relative humidity meter (not shown in figure) and was used to enclose the sensor platform in an environment of a set gas and relative humidity concentration as well as a acting as a mount for the excitation and detection optoelectronic components. The detection filter used for elimination of excitation light for all sensors was a red gel filter (LEE 135; LEE Filters, U.K.). In the course of the work, for both the intensity and lifetime-based different LEDs and photodiodes were used in

different setups. The blue LED used initially (λ_{max}=467nm, NSPB500S; Nichia, Japan) had a tail in the red region of the spectrum which was eliminated by the use of a bandpass filter (Schott Glass BG12; UQG Filters, U.K.). This LED was later replaced by a another blue LED (λ_{max}=450nm, LED 450-01U; Roithner LaserTechnik, Austria) which did not have a tail in the red region of the spectrum and could be used without the need for a band-pass filter. Two photodiodes were used in the course of this work, which will be described later in this chapter, one had in-built amplification but did not have its peak sensitivity at the modulation frequency used in this work, while the other need separate pre-amplification circuitry but was more sensitive at the required modulation frequency.

8.2.1 Spectrofluorometer

In order to determine the optoelectronic components required for use with a particular indicator dye, the fluorescent properties of the material need first to be determined. The emission spectrum of an indicator dye is the wavelength distribution of the emission measured at a single constant excitation wavelength. Conversely, an excitation spectrum plots the dependence of emission intensity, measured at a single emission wavelength, upon the excitation wavelength [1]. A spectrofluorometer is used to measure both types of spectrum. A block diagram of the various components that make up a spectrofluorometer is shown in Figure 8.2.

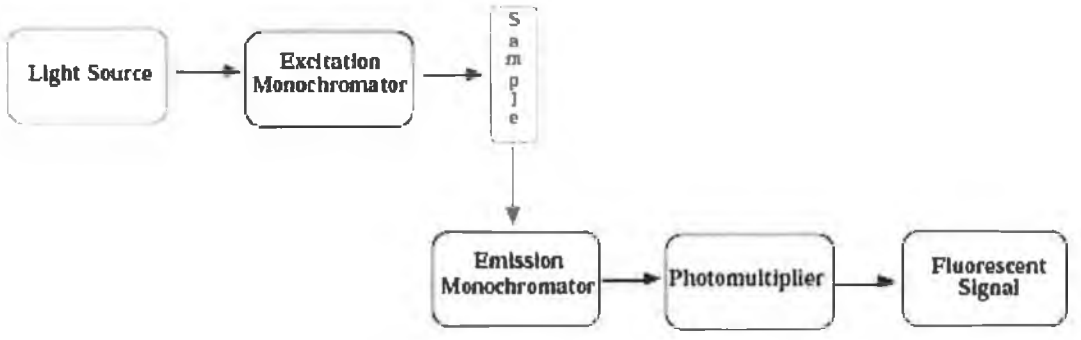

Figure 8.2: Block diagram of the main components of a spectrofluorometer.

A broadband light source is used to cover a large range of excitation wavelengths. The excitation monochromator is pc-controlled to enable the selection of a precise excitation wavelength to illuminate the sample in the sample chamber.

The emission monochromator is also pc-controlled and the slits can be adjusted to select a range of emission wavelengths to be detected from the sample and detected at the photomultiplier tube. From analysis of the spectra produced, an excitation light source can be chosen to match the peak of the excitation spectra. The emission spectrum aids the selection of suitable optical filters to eliminate any excitation light from reaching the detector, while also detecting the peak fluorescence which is found at the peak of the emission spectrum. The spectrofluorometer used in the course of this work is commercially available from Jobin Yvon Ltd. (Fluoromax2, Jobin Yvon, U.K.)

8.2.2 Linear image sensor system for fluorescence intensity measurements

Early experimental work was carried out using a UV-curable sol-gel waveguide platform as an oxygen sensor. The changes in fluorescence intensity from the sensor, when excited with a blue LED, with changing oxygen concentration was monitored. The signal levels in this case were too low to be detected with a simple photodiode and the detector chosen for this work was a cooled linear image sensor (Model S8383-1024; Hamamatsu, U.K.). The linear image sensor is made up of a self-scanning photodiode array of 1024 individual detectors and the output gives the intensity value at each detector. This detector was chosen to detect low signal levels as the cooling eliminates a large portion of the noise. This detector was also chosen as its array of detectors make it suitable for detecting the output from a linear array of sensors. This setup was then used to test the changes in fluorescence intensity from an array of sensors deposited on a UV curable sol-gel waveguide and on a multi-channel PMMA chip.

The linear image sensor was pc-controlled so that the intensity of each detector could be recorded for a specified integration time. For the linear image sensor to be used in the calibration of sensors, data capture was automated. The specific gas concentrations were supplied to the flow cell using a gas characterisation system as described in Section 8.4. The gas concentrations were controlled using a Labview program. As there were no Labview drivers available for use with the linear image sensor, software that simulated windows keystrokes was used to automate the data collection. A range of programs was written to take an average value of the fluorescence intensity of each detector at a pre-defined point at each gas concentration.

This enabled the generation of a calibration curve for the sensor.

8.2.3 CCD Camera for fluorescence intensity measurements

Charged coupled device (CCD) cameras are widely used for 2D detection. These are metal oxide semiconductor-based devices comprising rows and columns of pixels, each of which converts photons into electrons. At room temperature, thermally generated noise, referred to as dark current, can result in the generation of thousands of electrons per pixel per second. This can interfere greatly with the detection of low light levels and thus CCD cameras are often cooled to eliminate much of this noise. The CCD camera used in the course of this work, Sensicam (PCO; Germany), is a cooled CCD camera. This camera is more sensitive than the linear image sensor described in the previous section and was used for intensity-based sensing with very low levels of fluorescence present.

8.2.4 Modulated LED and lock-in amplifier system for fluorescence intensity measurements

After initial work was carried out using the linear image sensor, a system was developed which comprised a blue excitation LED which was modulated at a known frequency, f, and the resultant fluorescence intensity was detected at this frequency using a photodiode (10530DAL; IPL, U.K.) and a dual phase lock-in amplifier (Model 7265; Signal Recovery, U.K.). The photodiode used contained an in-built amplifier which eliminated the need for a separate pre-amplification circuit; thus the photodiode output can be connected directly to the lock-in amplifier. This method of detection was an improvement on the previous setup, Section 8.2.2, because, by incorporating a lock-in amplifier, the sensitivity to ambient and background light at different frequencies was reduced. In this system, the program to control the gas concentrations was modified to incorporate the output signal from the lock-in amplifier. While this method improved the stability of the results from an intensity-based detection system it did not fully remove the problems with intensity-based detection. For this reason, a decision was made to develop a system based on fluorescence lifetime rather than intensity.

8.3 Lifetime-based Systems

As discussed in Section 5.4.2, a more reliable way of measuring changes in fluorescence is to measure the fluorescence lifetime which is an intrinsic property of the analyte-sensitive molecule (fluorophore) at different analyte concentrations. Direct lifetime measurements were carried out to determine the absolute lifetime of a sensor film. Direct measurement of the lifetime necessitates the use of expensive laboratory instrumentation and a complex optical set-up which renders it unsuitable for low-cost miniaturised sensor platforms. To overcome some of these drawbacks, another detection method called phase fluorometry can be used. Both of these methods will be described in turn.

8.3.1 Direct lifetime system

A laser pulse photolysis system was used to directly measure the fluorescence lifetime of a sensor film. This apparatus consists of a Nd YAG laser (SL801; Spectron Laser Systems, U.K.) which excites the sensor film at λ_{ex} =355nm and a monitoring system, arranged in a cross-beam configuration. This monitoring system contained a monochromator and a photomultiplier tube. More details on this system can be found in [2]. The signal was captured using a digital oscilloscope (54510A; Philips, Ireland) and processed using software developed in house.

8.3.2 Phase fluorometry systems

As discussed in Section 5.4.2, a lower cost, less complex method of measuring fluorescence lifetime is phase fluorometry. In this approach one measures the phase shift between the excitation signal and the emitted fluorescence signal. This phase shift is proportional to the fluorescence lifetime as shown in Section 5.4.2, Equation 5.7. For phase fluorometric detection, a modulated LED, a photodiode and phase-sensitive detection electronics are used. These detection electronics measure the phase shift between the modulated excitation light and the resultant modulated fluorescence emission. A lab-based system for preliminary measurements and a portable prototype system were developed as part of this work.

Modulated LED and lock-in amplifier system for phase angle measurements

The lab-based system for measuring the phase angle of fluorescence emission from a sensor film consisted of a modulated blue LED and a dual phase lock-in amplifier. The LED was initially modulated directly from the lock-in amplifier which provided a sine-wave centered on 0V to modulate the LED. It was found that the LED does not turn on until approximately 2.5V is passed across it, thus a buffer circuit was required. This buffer circuit was developed to shift the applied voltage so that the LED remained on constantly. A circuit diagram for the buffer circuit is shown in Figure 8.3.

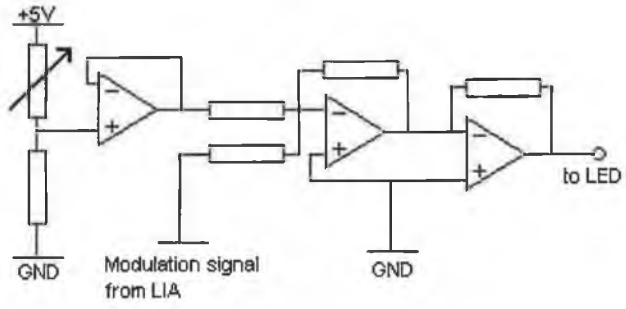

Figure 8.3: LED buffer circuit.

During the course of this work, two photodiodes were used. Initially the aforementioned photodiode with integrated amplifier was used and subsequently a PIN photodiode without in-built amplification was used (S1223; Hamamatsu, U.K.). The S1223 photodiode was more sensitive at the required modulation frequencies than the IPL 10530DAL, and its smaller size facilitated its use for multi-analyte detection. However as the S1223 photodiode has no amplification included, a custom-built pre-amplification circuit was developed. This circuit formed part of the electronics described later in this section and a circuit diagram of the pre-amplification circuit can be found in Appendix D, Section D.1.

Custom-built electronics with wireless communication for phase angle measurements

To have a truly portable sensor system, all large pieces of laboratory equipment need to be replaced by dedicated control electronics on compact circuit boards.

From previous work done in the Optical Sensors Laboratory, new custom-designed electronics for phase-sensitive detection were developed by John Moore [3]. The electronics control the excitation source, a blue LED, and monitor the resulting fluorescence emission from the sensor films using low cost Si-PIN photodiodes (Hamamatsu S1223). The circuit is a mixed signal board that consists of a combination of analog sensing circuitry and digital microcontroller-based circuitry. The digital circuitry performs data processing, waveform synthesis, PC interfacing and provides the user with real-time control of the circuits operating parameters. The circuit has been miniaturised by moving to surface mount components. The phase measurement is carried out using the exclusive-OR or XOR technique. This work is based on previous phase measurement electronics developed in the research group [4] and the main improvements have been the use of digital generation of the LED modulation waveform, current modulation of the LED, on-board signal processing and temperature compensation.

A block diagram of these electronics is shown in Figure 8.4. The area in red comprises the temperature compensation channel. In normal operation, light from the LED is detected by the reference photodiode and the corresponding phase angle is subtracted from the value detected by the signal photodiode. This serves to eliminate the effect of changes in LED output from the final sensor signal. A full circuit diagram is shown in Appendix D, Section D.3.

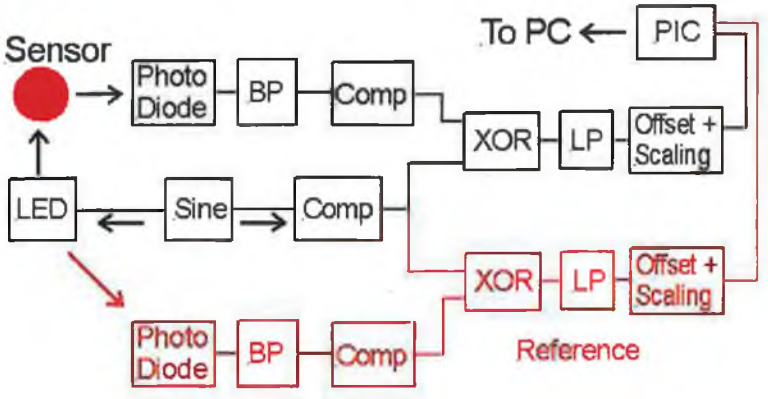

Figure 8.4: Block diagram illustrating the principle of the phase measurement electronics employed in this work. The reference channel is shown in red. BP - band pass filter, COMP - comparator, LP - low pass filter, Sine - sinewave synthesis, μC - PIC microcontroller.

The circuit developed was initially controlled and all data was collected via an RS232 link. The circuit also has the capability to link to an in-house designed RF module where the transmitter unit is connected to the circuit and the RF transceiver unit is connected to a remote pc thus enabling remote sensing and the development of a portable sensor [5]. The transceiver unit is shown in Figure 8.5. The transmitter unit is of similar dimensions.

Figure 8.5: RF transceiver unit.

This board was used to gain multi-channel data using an oxygen sensor. From the preliminary testing it was found that there were problems with crosstalk between the different channels on the board.

The LED control section of the circuit was also used separately to modulate LEDs for detection with a lock-in amplifier. The light output of the LED has a more linear relationship when the current is modulated compared to that of a modulated voltage. By modulating the current to the LED, it is possible to use active feedback in order to compensate for any fluctuations. A circuit diagram of the current modulation board used, which is an element of the overall custom-built electronics described earlier in this section, is shown in Appendix D, Section D.2. This modulation was employed in the dual reference phase lock-in detection which is described in Section 8.3.3.

8.3.3 Phase fluorometry using dual reference phase lock-in detection

An alternative method used for phase fluorometry measurements was dual reference phase lock-in detection (DRP). This technique involves the use of two optical sources, each modulated at a different frequency, to excite fluorescence from sensor films deposited on two separate waveguide channels. The use of different modulation frequencies for each channel facilitates the use of a single photodetector, which can discriminate between the two sensor signals on the basis of their modulation frequencies. This detection technique is available with the lock-in amplifier used

in this work. The sensor platform that was designed to exploit this detection principle is shown in Figure 8.6. The sensor chip consists of two curved waveguides, which are supported by a rectangular base. This base is coated with black paint to prevent optical crosstalk between waveguides. Sensor films are deposited on the waveguides at the positions indicated in Figure 8.6.

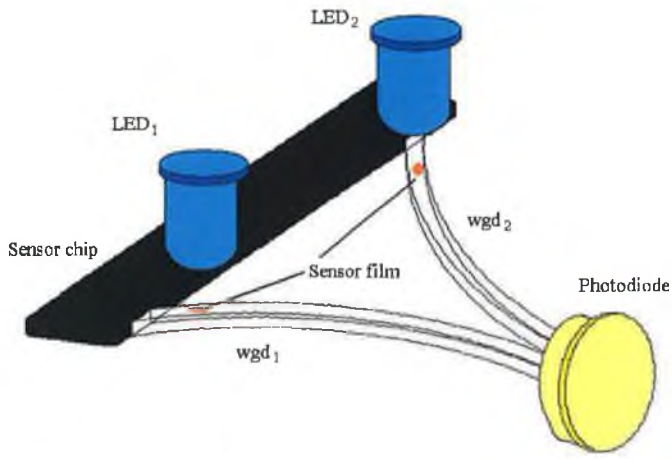

Figure 8.6: Curved PMMA sensor platform for dual reference phase lock-in detection (LED apertures not shown).

The spatial separation of the waveguides at this position enables discrete LED excitation of the individual sensor films. The light from the LED passes through an aperture and excites the single sensor film. The waveguides then curve inwards so that the fluorescence output can be detected at the endface with a single photodiode using DRP. This is accomplished by using the lock-in amplifier to resolve the input signal into two distinct components by performing a Fourier transform at each of the different frequencies. This eliminates the use of multiple photodiodes and, therefore, multiple lock-in amplifiers, and can be used for both multi-analyte or referenced sensing strategies. In addition to the internal reference derived from the lock-in amplifier, an external reference signal is needed to provide the second modulation frequency. In order to match the LED excitation on both channels, the LEDs were modulated using a reference signal and a current modulation board.

The curved sensor platform was designed in order to prevent optical crosstalk

between the sensor waveguides. While this worked successfully, a problem was noted with selective LED excitation of an individual waveguide. Despite the fact that the two LEDs were directed on a single spot, a small amount of excitation light was found to excite the spot on the other channel.

A Matlab model was developed to investigate the effect of the background fluorescence emission on the total measured fluorescence and is listed in Appendix C (Section C.2). This background fluorescence emission resulted from the LED exciting both sensor channels simultaneously. For example, if LED_1 modulated at f_1 was used to excite the sensor film on waveguide 1, wgd_1, the fluorescence signal emission would be accompanied by a second component of fluorescence at the detector at the same frequency, f_1. This second component results from LED_1 indirectly exciting the sensor film on waveguide 2, wgd_2, at the frequency, f_1. This component will be described as background fluorescence emission. Conversely, there will also be two other components present at the detector when LED_2 is used at the frequency, f_2. This model investigates the effect when only one LED is used and the configuration is shown in Figure 8.7. The effect of this background emission which is present in parallel with the signal emission is examined to determine whether this will influence the measured fluorescence signal.

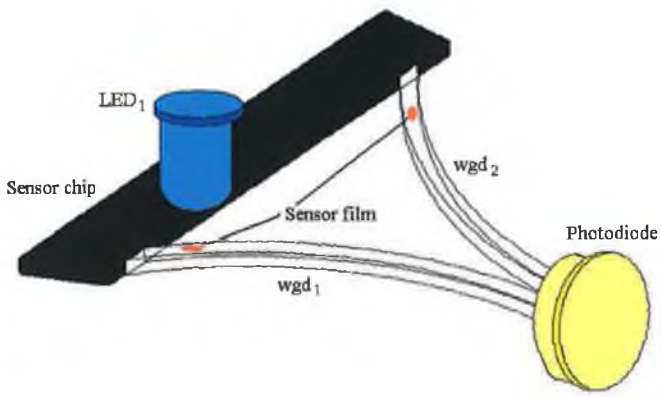

Figure 8.7: Optical configuration of curved sensor platform being investigated. Fluorescence signal modelled when one LED is used to excite the sensor platform.

This model is developed in a similar manner to that for phase fluorometry (Section 5.4.2). In this case, there are two emission signals, the signal emission and the background emission. The excitation and resultant fluorescent emission is given by

$$E = A\sin(\omega t) \tag{8.1}$$

$$R_1 = a_1\sin(\omega t - \phi_1) \tag{8.2}$$

$$R_2 = a_2\sin(\omega t - \phi_2) \tag{8.3}$$

where E is the excitation, R_1 and R_2 are the signal and background emissions respectively (with amplitudes a_1 and a_2 and phase angles ϕ_1 and ϕ_2). The term $\omega = 2\pi f$, where the modulation frequency, f, is the same for all signals. The total emission is calculated by adding R_1 and R_2, with the phase angle being found by measuring the difference between the total emission and the excitation signal. The values of the parameters used in this model were determined experimentally, from oxygen sensor films deposited on the platform. These values are shown in Appendix C (Section C.2). The amplitude of the background emission, a_2, was varied from 0-10 while the fluorescence emission signal amplitude, a_1, was set to 200. A graph of the phase angle versus the background amplitude is shown in Figure 8.8.

Figure 8.8 shows that, at low amplitudes ($\leq$ threshold amplitude), the background has no influence on the measured phase angle. As the amplitude increases, the measured phase angle changes. The threshold amplitude, a_t, beyond which the background influences the measured phase angle occurs for an amplitude ratio (a_1:a_2) of 213. If $a_1 < 213a_2$ the background signal will effect the measured phase.

The effect of background emission on measured signal emission was quantified experimentally using a sensor chip which only supported a single oxygen sensor film. The remaining waveguide channel had no sensor film deposited upon it. This effect was determined experimentally by measuring the fluorescence when the sensor film is excited directly i.e. only LED_1 exciting the sensor film on wgd_1 and then measuring the fluorescence when only LED_2 was used to excite the uncoated waveguide, wgd_2. The ratio of fluorescence from the directly excited channel, wgd_1 excited by LED_1, to fluorescence when the waveguide was excited by stray excitation light, coming from LED_1 but exciting wgd_2, was found to be 1000:1. This ratio is assumed to be true for the background emission and signal emission found at

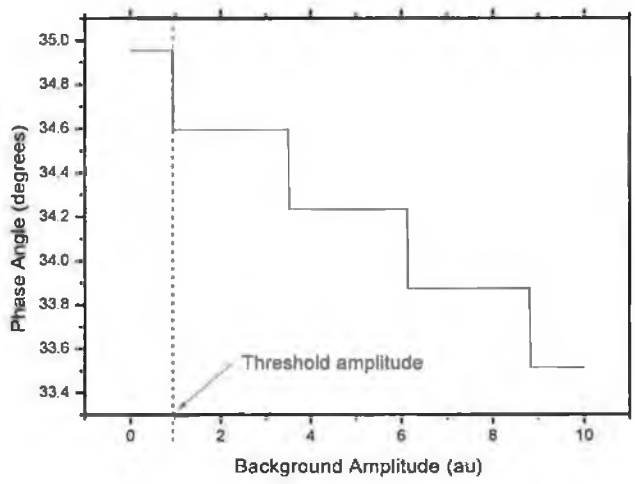

Figure 8.8: Effect of background emission from stray excitation light on final measured phase angle from curved sensor platform.

a single modulation frequency. From the experimentally collected data the background amplitude is much greater than the signal amplitude (a_1=1000a_2) which means that the background emission should have no effect on the sensor response.

The next stage in the development of this model was to determine the effect on the threshold amplitude, a_t, caused by all of the parameters listed in Equations 8.1-8.3. The parameters investigated were:

1. Emission Phase Angle, ϕ_1
2. Background Phase Angle, ϕ_2
3. Excitation Amplitude, A
4. Modulation Frequency, f
5. Amplitude Ratio

1. Emission Phase Angle, ϕ_1

   The effect of the emission phase angle, ϕ_1 was investigated. The emission phase angle was varied between the extremes of phase angle values found for

all of the sensor films used in the course of this work (i.e. $0° < \phi_1 < 35°$). The threshold position for the background emission signal to affect the measured phase angle was found to vary with emission phase angle. As the phase angle decreases, this threshold occurs at a much larger background signal amplitude. This is shown in Figure 8.9 where the phase angle versus background signal amplitude is plotted for the case where $\phi = 15°$ and $\phi = 35°$. At the maximum phase angle obtained for the sensors developed, the background does not effect the measured phase when $a_1 \geq 213a_2$.

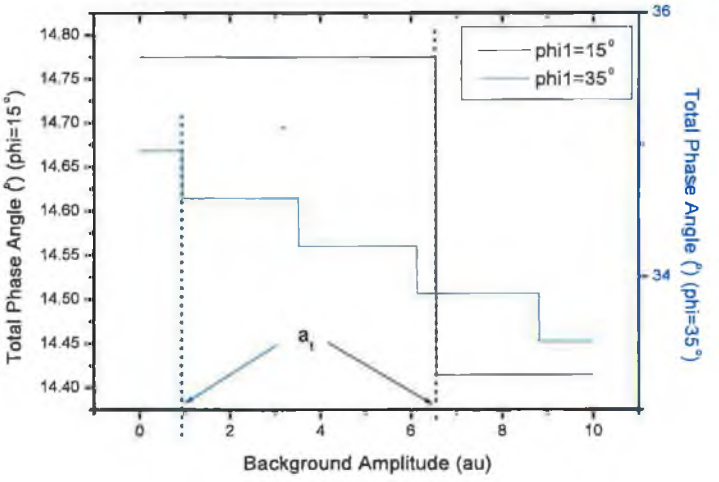

Figure 8.9: Effect of emission phase angle on threshold position for background amplitude from stray excitation light to affect final measured phase angle from curved sensor platform.

2. Background Phase Angle, ϕ_2

   The effect of altering the background phase angle was also investigated by testing the model between $\phi_2 = 0°$ and $\phi_2 = 180°$. In a similar manner to the effect of the emission phase angle, altering the background phase angle changes the threshold point, a_t. A sample result is shown for $\phi_2 = 45°$ and $\phi_2 = 90°$ in Figure 8.10. The earliest point at which the background signal influences the measured phase again occurs when $a_1 \geq 213a_2$.

3. Excitation Amplitude, A

   Altering the excitation amplitude, A, has no effect on the measured phase

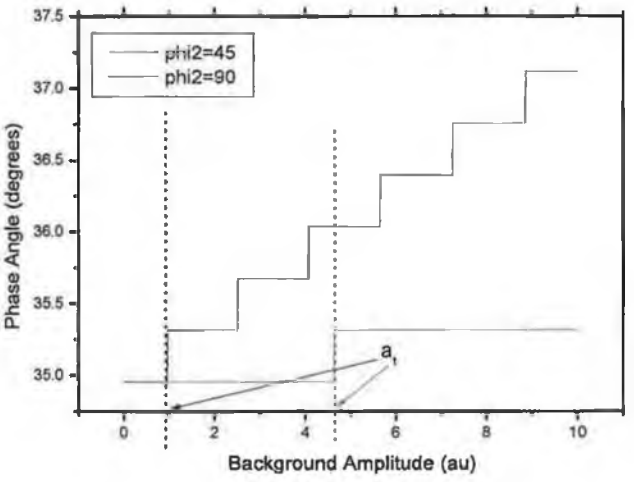

Figure 8.10: Effect of background phase angle on threshold position for background amplitude from stray excitation light to affect final measured phase angle from curved sensor platform.

angle. This is shown for two values of excitation amplitude in Figure 8.11

4. Modulation Frequency, f
   The influence of modulation frequency was tested at a range of modulation frequencies between 5kHz and 20kHz. The modulation frequency does not affect the point, a_t, where the background signal amplitude has an effect on the measured phase angle. This is shown in Figure 8.12 for f=17kHz and 20kHz.

5. Amplitude Ratio
   The ratio of the emission and background signals determines the phase angle. When the ratio of the amplitudes is altered, a_t is also altered. This is shown in Figure 8.13, where the amplitude ratio is halved from 200:0.2 to 100:0.2, with the result that a_t also halved.

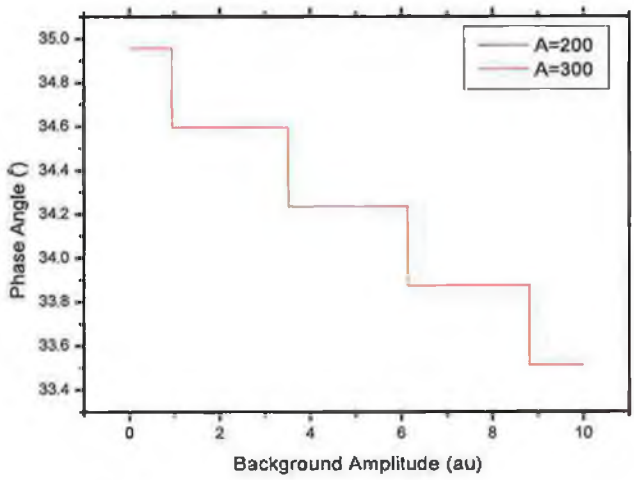

Figure 8.11: Effect of excitation amplitude on threshold position for background amplitude from stray excitation light to affect final measured phase angle from curved sensor platform.

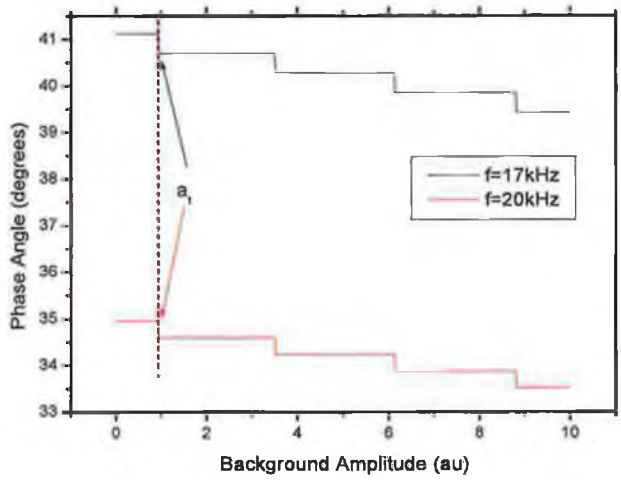

Figure 8.12: Effect of modulation frequency on threshold position for background amplitude from stray excitation light to affect final measured phase angle from curved sensor platform.

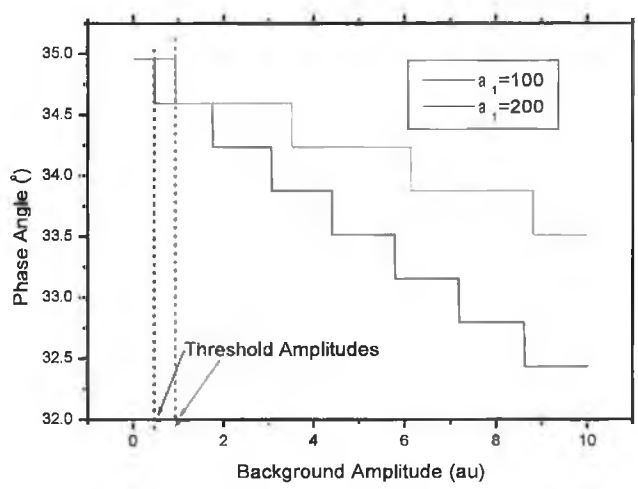

Figure 8.13: Effect of emission amplitude ratio on threshold position for background amplitude from stray excitation light to effect final measured phase angle from curved sensor platform.

8.4 Calibration Systems

In order to calibrate the sensor films, each sensor needed to be exposed to specific concentrations of the analyte to be sensed. This was done by enclosing the sensor in a sealed gas flow cell and using combinations of mass flow controllers (MFC) (UFC 7300; Celerity, Ireland) and gas wash bottles to regulate the gas mixture and its relative humidity. Each mass flow controller has an internal sensor which measures the gas concentration actually flowing. In the case of oxygen, carbon dioxide and nitrogen concentrations this measured value is used in all data analysis. As the aim of this work was to develop a multi-analyte sensor chip, the effect of cross-sensitivity to the other analytes being sensed was also studied for each sensor and this required a more complex calibration system. The gas flow cell, as shown in Figure 8.1, contained a thermistor (30K6A3091; Betatherm, Ireland) and a relative humidity meter (HIH 3610-002; Honeywell, UK). The output of these calibration systems was monitored and recorded using a Labview program which also controlled the gas flow. The final calibration system used when characterising the dual referenced chip, described in Section 8.3.3, used a combined digital relative humidity and

temperature meter (SHT75; Sensirion, UK) which outputted digital readings to the PC serial port. This was also incorporated into the Labview program. A diagram of the control circuit used for the SHT75 is shown in Appendix D, Section D.4.

8.4.1 Oxygen and carbon dioxide sensor calibration system

Initial work involving the calibration of the oxygen sensor film used two MFCs to control the gas mixture entering the flow cell. An oxygen mass flow controller regulated the amount of the analyte gas (i.e. oxygen) to be tested and the carrier gas used was nitrogen. A diagram of this gas calibration system is shown in Figure 8.14. As mentioned previously, the MFCs are controlled using a Labview program which enables the automatic setting and cycling of specific gas concentrations. This program can step through a range of gas concentrations and can also continually record the temperature and the relative humidity in the flow cell. This system enabled the calibration of the oxygen sensor film in dry air.

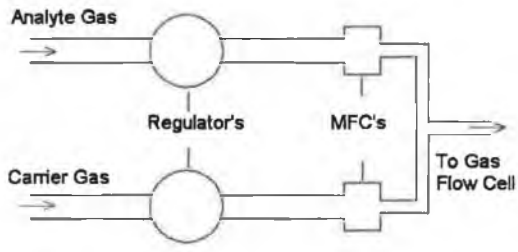

Figure 8.14: Oxygen sensor gas calibration system.

For calibration of the carbon dioxide sensor films, a humid environment was required as in a dry environment the sensor films dried out and were no longer sensitive. The process of achieving a specific relative humidity concentration is non-trivial and this will be described in detail in Section 8.4.2. The relative humidity concentration reached the highest value obtainable and remained constant at this value to provide a humid environment when cycling through the carbon dioxide concentrations. The gas was humidified by passing it through a series of gas wash bottles, each containing water. A diagram of the carbon dioxide sensor gas characterisation setup is shown in Figure 8.15.

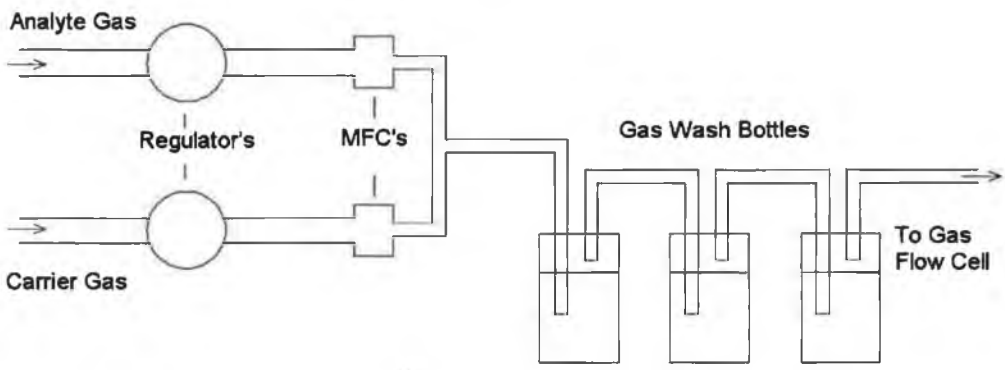

Figure 8.15: Carbon dioxide sensor gas calibration system.

8.4.2 Relative humidity gas characterisation system

As mentioned in Section 8.4.1, achieving specific stable relative humidity concentrations is non-trivial. Different relative humidity concentrations are obtained by mixing wet and dry gas in different ratios. The wet gas is obtained by flowing the gas through a series of gas wash bottles. In the case of relative humidity, the proportion of wet gas to dry gas alone is not sufficient to accurately determine the relative humidity in the flow cell. Factors such as temperature and the quality of sealing of the various components in the flow cell effect the relative humidity in the flow cell as does, the volume of the flow cell itself. Because of this, a thermistor and relative humidity meter are incorporated into the flow cell and their outputs are used to calculate the relative humidity concentration in the flow cell. This recorded value of relative humidity is used in all subsequent calculations. The quality of the gas flow cell will also play a large part in determining the maximum relative humidity concentration that can be achieved. If the flow cell is not sealed adequately the maximum relative humidity concentration obtainable will be limited. 0% relative humidity concentration is extremely difficult to obtain in this type of setup due to factors such as the external temperature, ambient relative humidity and pressure. In this thesis, reference to 0% relative humidity implies the lowest relative humidity concentration achievable under ambient conditions. This was typically between 0.1 and 2% relative humidity.

In the case of testing a sensor the relative humidity sensitivity of a relative humidity sensor film, wet and dry streams of nitrogen gas are used to mixed different

relative humidity values. A schematic of a relative humidity sensor gas characterisation setup is shown in Figure 8.16.

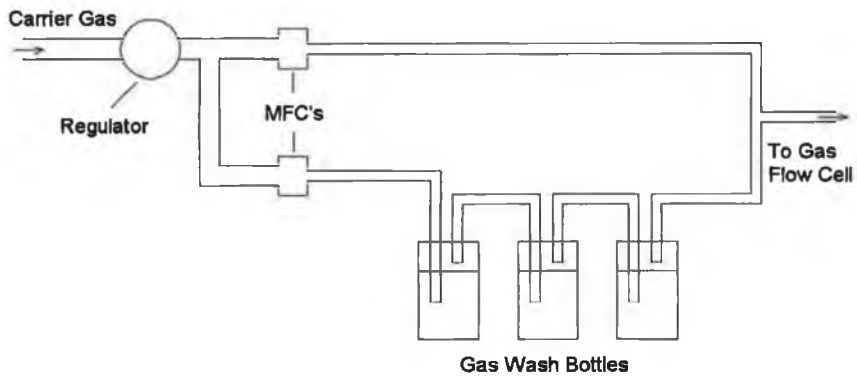

Figure 8.16: Relative humidity sensor gas calibration system.

8.4.3 Interference test system

As the sensors developed are interrogated simultaneously, cross-sensitivity to the other analytes being sensed was tested. For example, the oxygen sensitivity of both the oxygen sensor or the relative humidity sensor at different relative humidities needs to be investigated. To test the sensitivity of a sensor film at low relative humidity concentrations, typically $< 50\%$ relative humidity, the gas characterisation setup used can be seen in Figure 8.17.

This setup can be used in the same manner for different analytes, i.e. carbon dioxide, at a range of low relative humidity concentrations. If high relative humidity concentrations are to be tested the analyte gas and carrier gas can be interchanged to humidify the analyte gas and flow dry carrier gas. To cater for the full range of analyte and relative humidity values a fourth mass flow controller can be added.

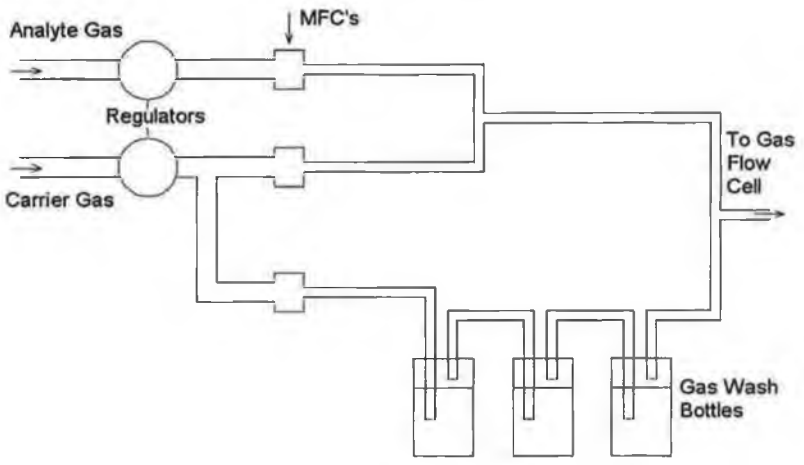

Figure 8.17: Interference test gas calibration system.

8.5 Summary

The various systems developed to monitor changes in fluorescence from the developed sensors has been described. The progression of the system from an intensity-based system to a phase-fluorometry based system with portable electronics and wireless communication was discussed. The characterisation systems to calibrate the sensor films for the selected analytes as well as cross-sensitivity to other analytes was also outlined.

Bibliography

[1] J. Lakowicz. *Principles of Fluorescence Spectroscopy.* Plenum Press, New York, 2nd edition, 1999.

[2] B. S. Creaven, M. W. George, A. G. Ginzburg, C. Hughes, J. M. Kelly, C. Long, I. M. McGrath, and M. T. Pryce. Laser-pulse photolysis and transient infrared investigation into the effect of solvent or substituents (X) on the reactivity of $(\eta^6\text{-}C_6H_{6-y}X_y)Cr(CO)_2$ photogenerated intermediates. *Organometallics*, 12(8):3127–3131, 1993.

[3] John Moore. Optical Sensors Laboratory, Dublin City University, Personal communication, 2005.

[4] L. Polerecky. *Optimisation of multimode waveguide platforms for optical chemical sensors.* Ph.D. Thesis, Dublin City University, 2002.

[5] Innovada. ComLink RF user guide, Internal Report, 2004.

Chapter 9

Results and Analysis

The results from the various stages of development of the multi-analyte sensor platform and the sol-gel optical sensor films for oxygen, relative humidity and carbon dioxide are be described in detail in this chapter along with the different variations of experimental systems used to characterise the sensor films. As oxygen sensing was the most developed optical sensor within the laboratory, all initial testing of sensor platforms or detection methods were first carried out with oxygen. This chapter describes the progression of the sensor platform from a planar substrate into a structured polymer chip. The application chosen to demonstrate the capabilities of the multi-analyte sensor platform was indoor air-quality monitoring. To this end, the sensor films have been designed to be sensitive within a particular range of concentrations for the analytes being sensed i.e. 0-50% oxygen (in particular 18-22%), 0-50% relative humidity and 0-20% carbon dioxide.

9.1 Oxygen Sensing

The first optical sensor film developed was for oxygen sensing. All initial work was carried out using a sol-gel film derived from the precursor MTEOS. The sensor film preparation is described in Section 5.3.1.

9.1.1 UV curable sol-gel waveguides

A sensor platform fabricated from UV-curable sol-gel was used. This platform was developed using two methods as described in Section 7.3. The development of sol-gel waveguide-based oxygen sensor platforms will be described for each waveguide

fabrication method.

Method 1

A sol-gel waveguide platform for oxygen sensing was developed using a purely photolithographic method to fabricate the waveguides. This fabrication method is described in Section 7.3.3. The sensor platform consisted of four waveguides each 100μm wide, approximately 15μm high, with 1mm spacing between adjacent sensor channels. MTEOS-based oxygen sensor films were deposited on the sensor platform using micro-contact printing. The sensors were interrogated using an intensity-based detection method. A blue LED was used to excite the sensor spots and the fluorescence intensity was detected using a cooled CCD Camera. An image of the fluorescence intensity from each sensor channel at 0% oxygen is shown in Figure 9.1. This image was analysed using an internally developed DOS-based software, CCDImage, to extract an intensity profile of the intensity across the waveguides. These profiles are shown in Figure 9.2 for the full range of oxygen concentrations. It can be seen that there is a large variation in intensity across the waveguides on the sensor platform. This is due to the sensor films being deposited using micro-contact printing which does not reproducibly deposit sensor film on each waveguide. As this measurement of fluorescence is an intensity-based method, the variation in sensor film volume deposited on each waveguide leads to a large variation in intensity being detected.

Figure 9.1: Image of fluorescence from a 4-channel UV curable sol-gel waveguide platform at 0% oxygen.

As discussed in Section 6.3.2, this method of fabricating waveguides leads to a high amount of losses in the waveguides. The fluorescence output of this platform was very low and was very difficult to detect using the cooled linear image sensor. The results presented here were detected using a cooled CCD camera which was more sensitive than the linear image sensor. The fabrication process for the UV

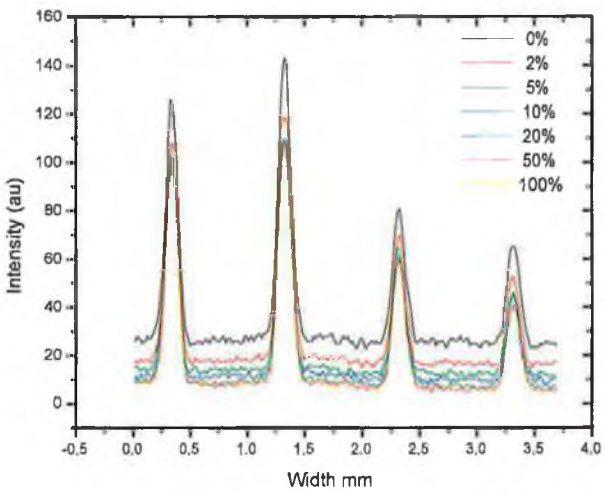

Figure 9.2: Oxygen sensitivity of UV curable waveguide using CCD camera.

curable waveguide platform was improved upon and will be discussed in the next section.

MIMIC

The waveguides developed and described in Section 9.1.1 suffered from optical losses. The fluorescence from these waveguides could only be detected using a cooled CCD camera. Low-cost detectors could not be used as they were not sufficiently sensitive to detect the fluorescence output from the waveguides. Also, the small waveguide height achieved using this process resulted in difficulties in optical alignment. A new method of developing sol-gel waveguides was investigated. This method was based on the soft-lithography technique of micro-moulding in capillaries (MIMIC) as described in Section 7.3.4. This technique enabled the fabrication of waveguide structures with larger heights which increased the number of modes that could be guided in the waveguide (Section 4.2). The sol-gel process used in the platform fabrication was altered to introduce a greater refractive index difference between the buffer and guiding layers than what was achieved in the previous process (Section 6.3.2). It is shown in Section 6.3.2 how these modifications improve the amount of fluorescence signal in the waveguide. This waveguide

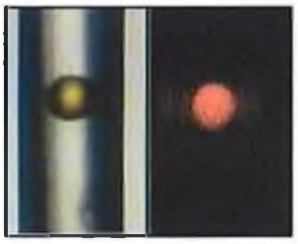

Figure 9.3: Oxygen sensor film deposited on UV-curable waveguide by pin-printing under both white light and optical excitation from a blue LED.

platform could then be used with the standard photodetectors. The waveguide platform consisted of a set of 100μm wide, ~80μm high waveguides each separated by 200μm. MTEOS-based oxygen sensor films were deposited on the waveguides by both micro-contact printing and pin printing. The platform was placed in a sealed gas flow cell and the sensor films were excited using a blue LED and the fluorescence intensity detected using the linear image sensor [1]. Figure 9.3 shows a sensor film pin printed on a single waveguide under both white light excitation and when excited by a blue LED. These images were obtained using a video microscope (BX51M; Olympus, U.K.). A resulting Stern Volmer plot of the oxygen sensitivity of two films is shown in Figure 9.4. The non-linearity of the Stern-Volmer plot comes from the non-homogeneity of the film and the presence of different lifetime components.

Deposition	Resolution (0-20% Oxygen)	Limit of Detection
Micro-contact	0.53	0.29
Pin	0.63	0.98

Table 9.1: Limit of detection and resolution of micro-contact and pin printed oxygen sensor.

It can be seen in Table 9.1 and Figure 9.4 that the micro-contact printed sensor has more sensitivity and a lower limit of detection than the pin-printed sensor. This is thought to be due to increased porosity of the thicker film, deposited by micro-contact printing, which makes the dye more accessible for the analyte and leads to higher sensitivity. The micro-contact printed signal also gives much a higher signal to noise ratio due to the large volume of sensor film deposited. This

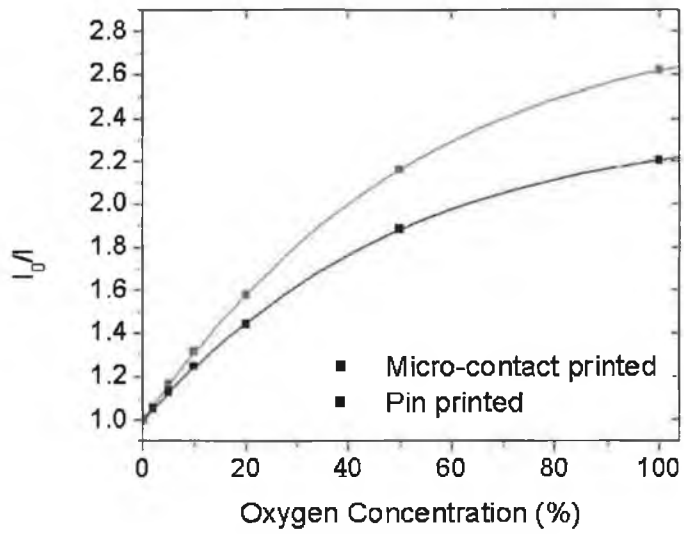

Figure 9.4: Stern Volmer plots for both micro-contact and pin printed oxygen sensor using a MIMIC-based UV curable sol-gel waveguide.

printing method cannot be used on a miniaturised multi-analyte sensor chip, as the sensor spot spreads and cannot be selectively printed on different waveguides in the same accurate way as the pin printed spots. While the fluorescence output could be easily detected using the linear image sensor it was not sufficient to be detected using the photodiode with in-built amplification and hence lifetime-based detection could not be undertaken.

When the photodiode with integrated amplifier (IPL10530DAL) was replaced with a photodiode which was more sensitive at the modulation frequency of interest (S1223), a set of sensor platforms was developed using the MIMIC-based technique. The platform consisted of a set of four waveguides which were 100μm wide, ~80μm high, with a separation of 1mm between adjacent waveguides. Oxygen sensor films were deposited on the waveguides using micro-contact printing. In this case, a blue LED was modulated using a lock-in amplifier and the phase-shifted fluorescence was recorded. A plot of phase angle versus oxygen concentration for the sensor is shown in Figure 9.5. This figure shows that the response time of the sensor is less than 30s and this response is more than satisfactory for measurements in the area of indoor air quality monitoring. The carbon dioxide sensor presents a similar response time

while a clear quantification of the response time of the relative humidity sensor is not possible due to the time taken to produce a specific relative humidity level in the flow cell. The overall response time including that taken to set the humidity level is in the order of 2 minutes and this is also suitable for indoor air quality monitoring. The limit of detection and resolution are calculated for the sensor and shown in Table 9.2. These are a considerable improvement on those obtained using the intensity-based detection system. This improvement is mainly due to the incorporation of a more sensitive photodetector in the detection system.

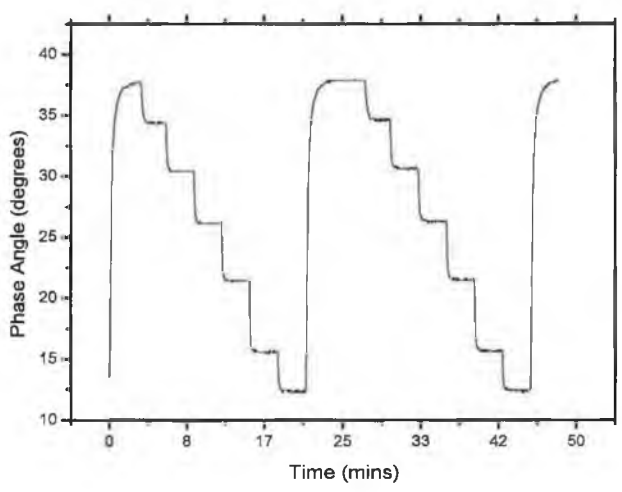

Figure 9.5: Phase angle response of UV-curable sol-gel waveguide, fabricated using MIMIC technique, to changing oxygen concentrations.

Deposition	Resolution (0-20% Oxygen)	Limit of Detection
Micro-contact	0.20	0.10

Table 9.2: Limit of detection and resolution of phase-angle based oxygen sensor.

9.1.2 PMMA platform

Intensity-based Sensing

As an alternative to the UV curable sol-gel waveguides, a plastic chip was fabricated in PMMA, as described in Section 7.4, and a typical example of this platform for use with the linear image sensor is shown in Figure 9.6. This chip had much larger dimensions than the UV curable sol-gel waveguides described in Section 9.1.1; each channel was 1mm wide. This enabled less complex detection of the output of the sensor channels. Preliminary work with this platform evaluated its use as a multi-channel oxygen sensor. MTEOS-based oxygen sensor films were deposited on each of the four channels using micro-contact printing. The platform was enclosed in a flow cell and the sensor spots were excited by a blue LED and the outputs from these channels were detected on the linear image sensor. The linear image sensor was a suitable detector to use as its large range of pixels are suited to the spatially resolved detection of the output from each channel. To further ensure that the spatial resolution was maintained a unit magnification planar lens (UMPL) was used to focus the fluorescence output onto the detector. Figure 9.7 shows the actual intensity data across all the channels for a range of oxygen concentrations and Figure 9.8 shows the corresponding Stern Volmer plot for the four channels.

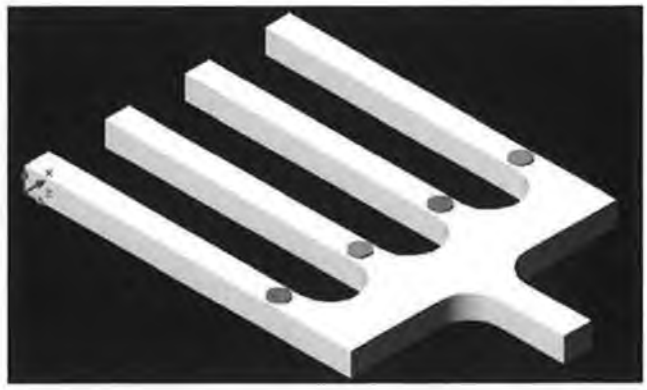

Figure 9.6: PMMA chip.

The differences in the intensity values for each peak are due to the fact that the sensor films were deposited using micro-contact printing. This method does not lead to the deposition of a repeatable volume of sensor film on each channel and as the sensor is intensity-based this leads to a large variation in the response

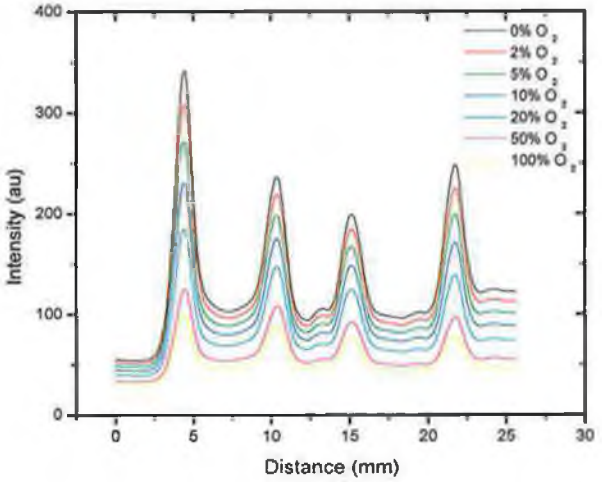

Figure 9.7: PMMA oxygen sensor chip scan data.

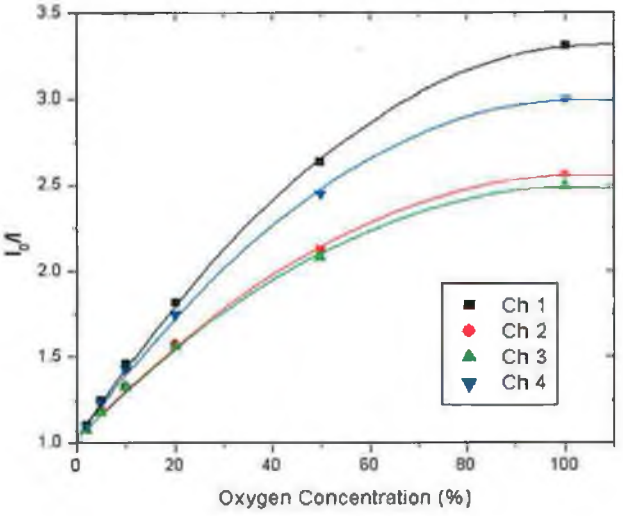

Figure 9.8: PMMA Oxygen sensor chip Stern-Volmer plot.

between the various sensor channels. The limit of detection (LOD) and resolution were calculated for channel 1 of this sensor. The LOD is are 0.50% oxygen while the resolution for the range 0-20% oxygen is 0.34% oxygen. Figure 9.7 shows good spatial resolution between the different channels. This demonstrates the ability to deposit a different analyte-sensitive film on each sensor channel, and detect each channel separately which would enable multi-analyte detection.

Lifetime-based sensing

As intensity-based sensing is not capable of providing a long-term repeatable sensor response, (Section 5.4.1), lifetime-based fluorescence detection sensors were developed. To enable the detection of the phase shift between the modulated excitation signal and fluorescence emission the linear image sensor was replaced by photodiodes and a lock-in amplifier. An individual photodiode was used to detect the fluorescence emission from each sensor channel. The polymer platforms were enclosed in a flow cell which was able to house the polymer platforms and wide enough to have a photodiode placed at the endface of each channel. The photodiode which showed the best performance, of those tested, was the S1223. This photodiode and its corresponding pre-amplification circuit were used for this work. The LED was modulated from the lock-in amplifier and shifted using an LED buffer circuit, as described in Section 8.3.2, to ensure the LED was maintained on and the oxygen-sensitive phase-shift was measured using a lock-in amplifier. It was found that the MTEOS-based oxygen sensor films showed a cross-sensitivity to relative humidity so an ETEOS-based oxygen sensor film was developed. This will be described in more detail later. The ETEOS-based sensor film was deposited on a PMMA chip by micro-contact printing and its phase angle response to changing oxygen concentrations is shown in Figure 9.9.

In addition to the development of a lab-based detection system for lifetime-based measurements a portable system was also developed using custom-built electronics as described in Section 8.3.2. The ETEOS-based oxygen sensor film was again tested using these dedicated control electronics and the phase-shift was transmitted from the electronics board to a remote PC using RF transmission. The sensor response obtained via the RF transceiver is shown in Figure 9.10. These electronics enable the development of a portable sensor for remote detection. It should be noted that the output of the control electronics is inverted and therefore appears to increase with increasing oxygen concentration.

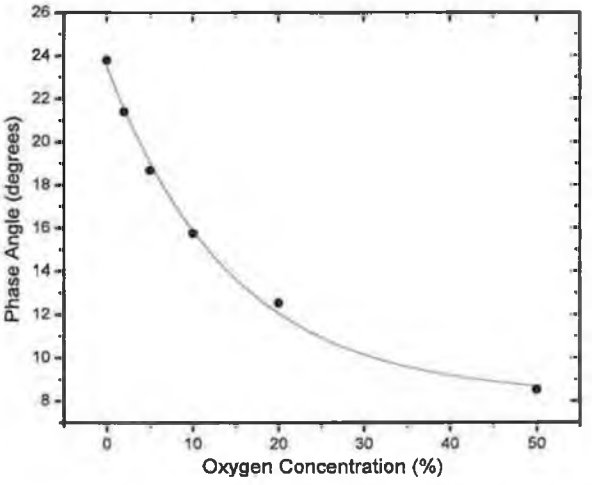

Figure 9.9: Phase angle response of ETEOS-based oxygen sensor film to changing oxygen concentrations.

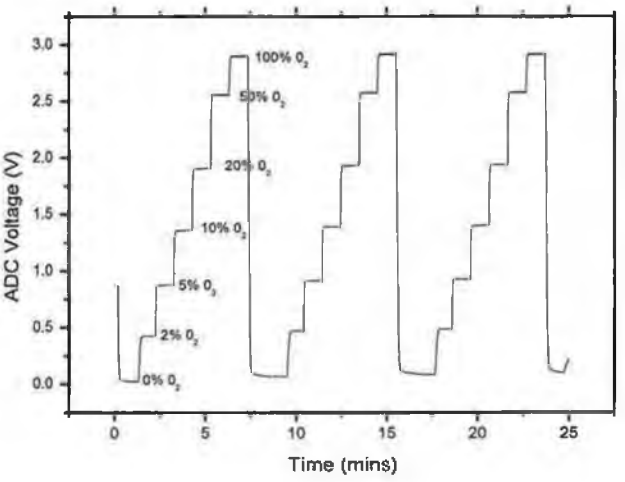

Figure 9.10: Phase angle response of ETEOS-based oxygen sensor film to changing oxygen concentrations with data collected via an RF transceiver.

Cross-sensitivity

As discussed previously, sensor films were optimised to minimise cross-sensitivity between sensors and to enable simultaneous multi-analyte detection. The oxygen-sensitive dye was encapsulated in a humidity-insensitive ETEOS-based sol-gel matrix to minimise cross-sensitivity to moisture as described in Section 5.3.1 [2]. The oxygen sensitivity of the oxygen sensor film was tested from 0-50% oxygen for relative humidity values from 0-50% RH, the range of interest for this application. The oxygen sensor response to oxygen over the relative humidity range of interest is shown in Figure 9.11. For a typical humidity concentration of 30-40% RH, the oxygen sensor shows an average limit of detection, (LOD), of 0.04% oxygen and a sensor resolution of 0.16% oxygen for the concentration range of oxygen tested i.e. 0% to 50% oxygen [3]. It can clearly be seen, in Figure 9.11, that the response curve for all humidity values overlap with an error of $\pm 0.3°$. Therefore there is minimal cross-sensitivity to moisture. The oxygen sensor was found not to be cross-sensitive to carbon dioxide. The phase angle response to changing carbon dioxide concentrations over time is shown in Figure 9.12, also plotted is the actual carbon dioxide concentration.

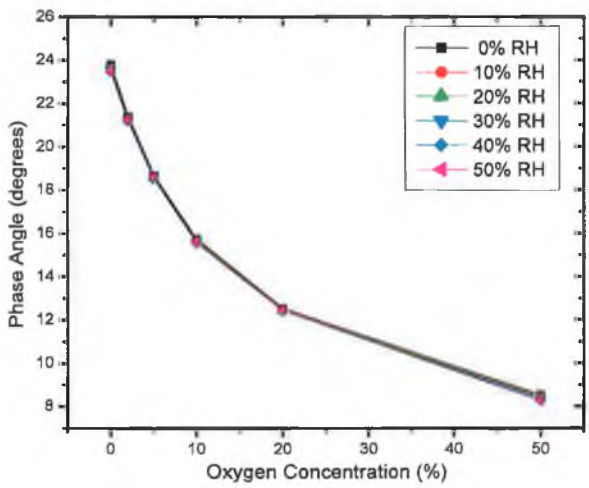

Figure 9.11: Humidity insensitivity of oxygen sensor.

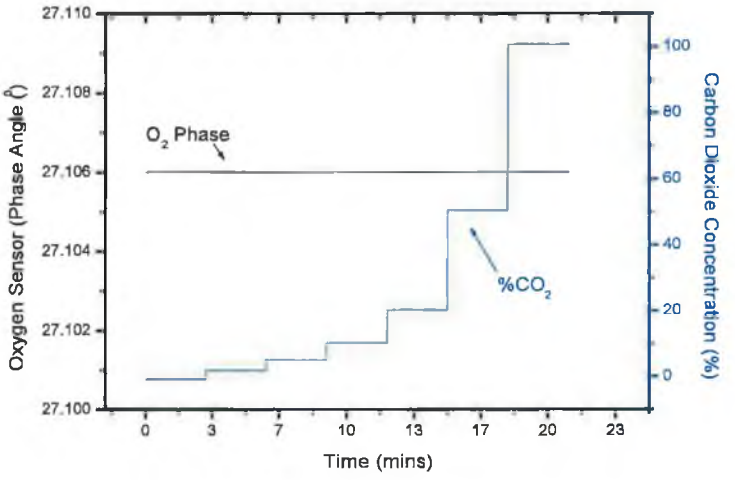

Figure 9.12: Carbon dioxide insensitivity of oxygen sensor.

9.2 Relative Humidity Sensing

An optical sensor film for relative humidity was developed based on the ruthenium complex, Ru(dppz), immobilised in a sol-gel matrix [4]. The sensor film preparation and operation is described in detail in Section 5.3.2. The fluorescence intensity and lifetime is quenched with increasing relative humidity. As the sensor film was being developed it was dip-coated onto a planar glass substrate for characterisation. The sensor was first investigated using an intensity-based detection system but, after when a sensor film recipe had been optimised, a lifetime-based detection system was employed.

9.2.1 Intensity-based sensor detection

Excitation of the sensor spots was accomplished using a blue LED and the output fluorescence was detected using a photodiode. The planar glass platform was enclosed in a flow cell and was characterised. The effect of aging time on the sensor response along with oxygen cross-sensitivity of the sensor was investigated. The response of the relative humidity sensors, aged for 30min, 1 and 6h, respectively, to different relative humidity concentrations is shown in Figure 9.13. For all relative humidity concentrations an increase in relative humidity leads to a proportional

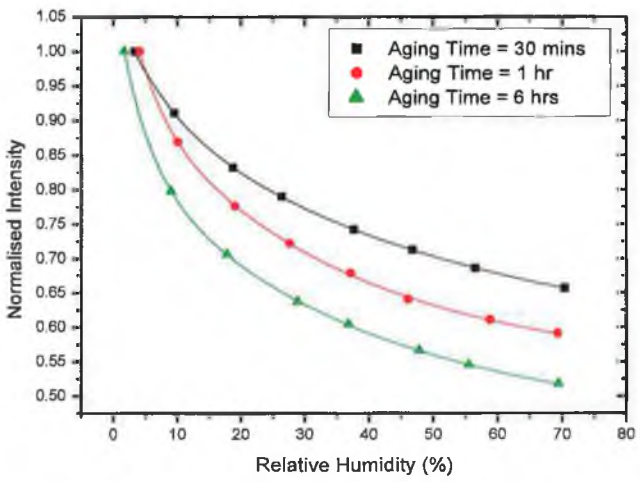

Figure 9.13: Fluorescence intensity from relative humidity sensors at different aging times.

decrease in the fluorescence intensity. Aging of the sols prior to coating leads to structural changes, which provides higher porosity, and this gives rise to higher sensitivity as can be seen by the increase in sensitivity with aging time.

The sensors developed are based on the changes in fluorescence from a ruthenium dye complex which have been used extensively in the development of optical oxygen sensors. Therefore the cross-sensitivity of the sensor to oxygen must be quantified. The effect of increasing aging time on the response of the relative humidity sensor to varying oxygen concentrations is shown in Figure 9.14. Again the sensitivity increases with increasing aging time in a similar fashion to the sensor response to relative humidity. It can be seen from the oxygen sensitivity that the effect of changing oxygen concentrations in the environment needs to be monitored and compensated for with the relative humidity sensor.

9.2.2 Lifetime-based sensor detection

From the data obtained using the intensity-based set-up, it was decided that the best relative humidity sensor film to use, of those tested, was the sensor with an aging time of 1 hour. This sensor was selected as a compromise between good

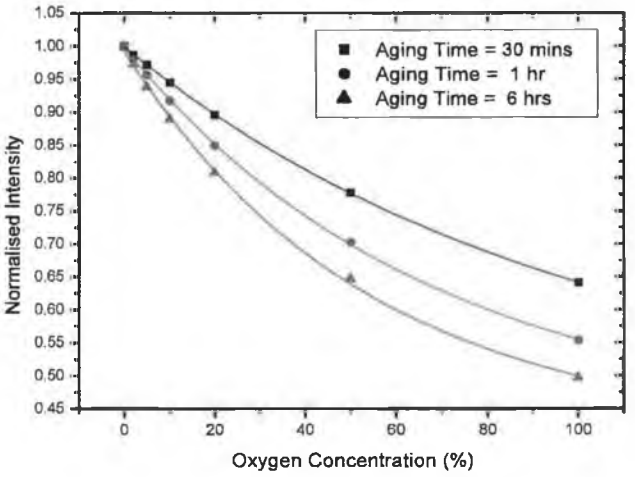

Figure 9.14: Oxygen cross-sensitivity of relative humidity sensors with different aging times.

relative humidity sensitivity and minimal cross-sensitivity to oxygen. A lifetime-based system was developed as described in Section 8.3.2. The sensor film was placed in a sealed flow cell and was excited using a blue LED, while the phase-shifted fluorescence emission was detected by a photodiode . As the principal application intended is in the area of indoor air-quality monitoring, the relative humidity concentration range of interest which was investigated in this work is 0-50% RH. The response of the selected sensor to changes in relative humidity is shown in Figure 9.15. A second order exponential decay fit was performed on the data and this was used to extrapolate the value of the phase angle over the entire range of relative humidity concentrations.

The percentage quenching, $\%Q_{RH}$, as defined in Equation 9.1, is a measure of the humidity sensitivity, and is calculated from the phase angle values at 0% ($\phi_{0\%RH}$) and ($\phi_{x\%RH}$) [where x=50 or 100% RH].

$$\%Q_{RH} = \frac{\phi_{0\%RH} - \phi_{x\%RH}}{\phi_{0\%RH}} \times 100 \tag{9.1}$$

The percentage quenching ($\%Q_{RH}$) is calculated using Equation 9.1 for both 0-50% and 0-100% relative humidity. From 0 to 50% relative humidity the %Q is

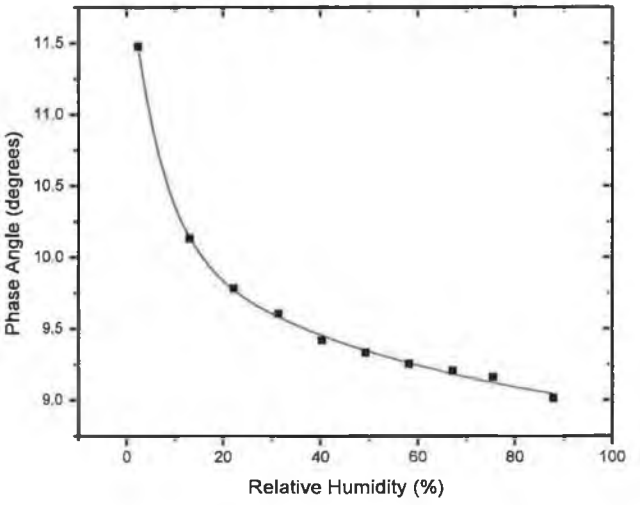

Figure 9.15: Phase angle plot of relative humidity sensitivity of relative humidity sensor.

24.12% and from 0 to 100% relative humidity this figure only rises to 25.92%. It can clearly be seen that the main region of sensitivity is in the concentration range of interest for the chosen application (i.e. 0 - 50% relative humidity). Only approximately 2% additional quenching takes place from 50 to 100%. This is probably due to moisture forming on the surface of the sensor film and blocking the mechanism for quenching taking place. The result is a decrease of the film sensitivity to relative humidity. The sensor has a limit of detection of 0.35% relative humidity and an average sensor resolution of 1.13% relative humidity, both measured as three times the standard deviation of the noise.

The selected sensor was tested for oxygen cross-sensitivity using the lifetime-based set-up and at a range of relative humidity concentrations from 0 to 50% RH. A plot of the phase angle versus the oxygen concentration for different relative humidity values is shown in Figure 9.16. It can be clearly seen that while the sensor has a significant sensitivity to oxygen at 0% RH, its sensitivity rapidly drops off with increasing relative humidity. This is most likely caused by the blocking of the pores due to the increasing amount of moisture present at higher relative humidity value. The main application of this sensor is in the area of air-quality monitoring

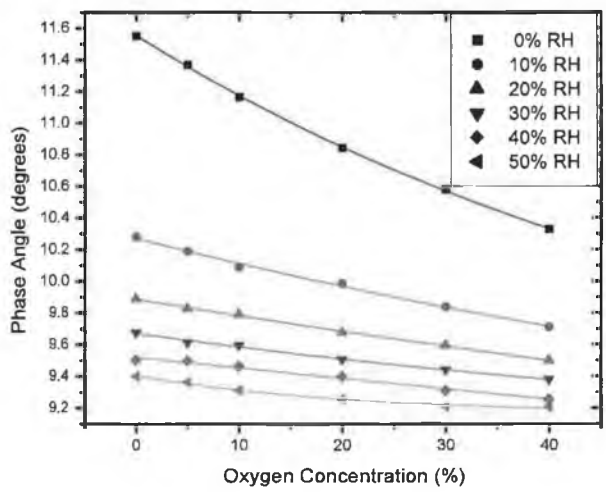

Figure 9.16: Oxygen cross-sensitivity of relative humidity sensor, over full range of oxygen and relative humidity concentrations.

using a multi-channel platform with sensors for oxygen and carbon dioxide [3]. The humidity levels encountered in this application will typically be greater than 30%. In this range, the cross-sensitivity to oxygen is quite small. Figure 9.17 shows the cross-sensitivity to oxygen at the typically encountered humidity and oxygen concentrations. On average there is a change in phase angle of approximately 0.02° from 18 to 22% oxygen for the typical relative humidity values which corresponds to a sensitivity of approximately 0.3% oxygen. These data can be plotted as a 3D plot and a curve fit obtained. A calibration function can then be obtained to enable the measurement of the exact relative humidity level at a particular oxygen concentration.

The relative humidity sensor was also tested as a micro-contact printed spot on a PMMA sensor platform. Its phase angle response was measured, in this case using the S1223 photodiode, and it was found to have a limit of detection of 0.21% RH and a sensor resolution of 0.92% RH from 0-50% RH [5]. Again, the sensor films oxygen cross-sensitivity was approximately 0.02°. The cross-sensitivity of the sensor to carbon dioxide was also tested. As the carbon dioxide concentration is changed, the relative humidity, measured by the independent RH sensor, varies. It can be shown that while the relative humidity sensor response changes with varying

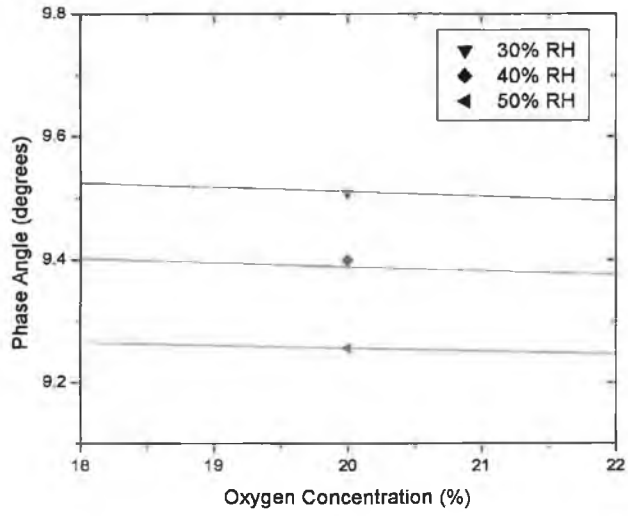

Figure 9.17: Oxygen cross-sensitivity of relative humidity sensor at most common oxygen and relative humidity concentrations.

carbon dioxide concentration this is not due to cross-sensitivity to carbon dioxide itself but rather the change in relative humidity caused by the carbon dioxide.

9.3 Carbon Dioxide Sensing

9.3.1 Intensity-based sensor detection

Carbon dioxide sensing films were tested after they were dip-coated onto a glass substrate. Intensity-based carbon dioxide sensors were first developed as described in Section 5.3.3. While two types of sensor film were developed, the results shown are for the ion-paired HPTS-based sensor. This sensor showed a better response to carbon dioxide than the TMOS-based sensor and also maintained water in the matrix for the reaction to proceed over a prolonged period. The sensor film was tested using a lock-in system with excitation provided by a blue LED. The detection was carried out through a red gel filter and a photodiode. A typical example of the intensity values for three cycles of gas concentrations is shown in Figure 9.18. The carbon dioxide concentration was varied from 0% to 100% with 2%, 5%, 10%, 20% and 50% as the intermediate steps. A corresponding calibration plot is shown in

Figure 9.19. It can also be seen that the largest changes in intensity correspond to low carbon dioxide concentrations, in particular from 0-2% carbon dioxide. As this sensor is to be applied to air quality monitoring, this range suits the application.

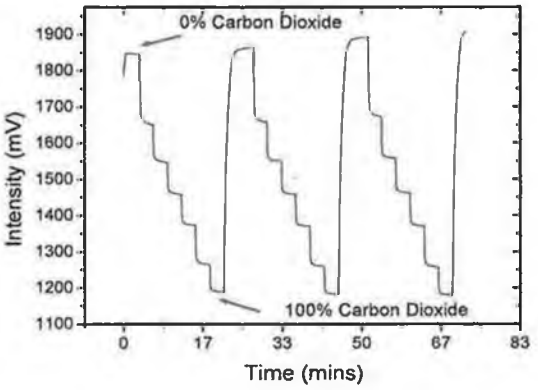

Figure 9.18: Scan data for intensity-based carbon dioxide sensor.

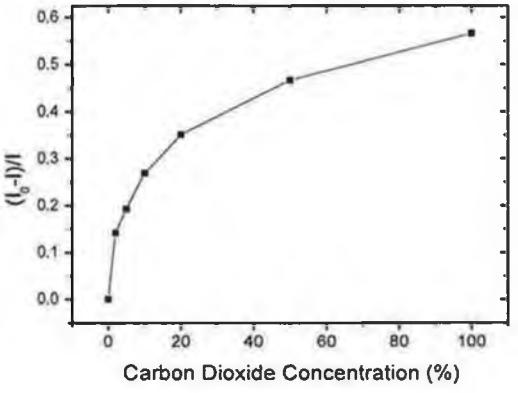

Figure 9.19: Calibration plot for intensity-based carbon dioxide sensor.

9.3.2 Lifetime-based sensor detection

A DLR-based sensor film was then developed using a reference dye incorporated into the sensor matrix along with the HPTS as described in Section 5.3.3. This

sensor film was tested in a similar manner to the intensity-based CO_2 sensors described above and its phase angle was measured using the lock-in amplifier. The carbon dioxide concentration was varied from 0% to 100% with 2%, 5%, 10%, 20% and 50% as the intermediate steps. The sensor scan data is shown in Figure 9.20 and the corresponding calibration plot is shown in Figure 9.21. Using the dual luminophore referencing technique, the total phase angle increases with increasing carbon dioxide concentration. Therefore, as the carbon dioxide concentration increases, the intensity from the indicator dye decreases and the total phase angle increases. This is unlike the pure HPTS intensity based sensors where increasing carbon dioxide leads to a decrease in fluorescence intensity. As was the case for the intensity based sensors, the peak sensitivity of this sensing film is at low carbon dioxide concentrations, as seen in Figure 9.21. The DLR-based carbon dioxide sensor has a limit of detection of 0.32% CO_2 and a sensor resolution of 0.39% CO_2 in the concentration range of interest for the application (i.e. 0-20% CO_2).

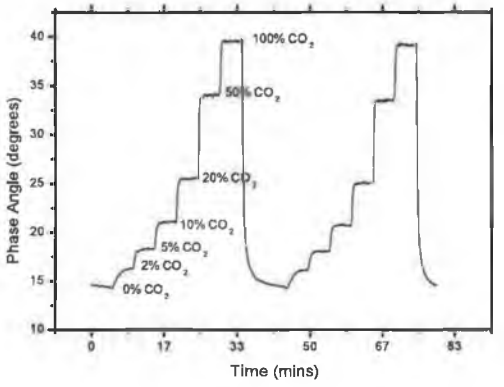

Figure 9.20: Scan data for DLR-Based carbon dioxide sensor.

9.3.3 Cross-sensitivity

The DLR-based carbon dioxide sensor films show negligible cross-sensitivity to oxygen as can be seen in Figure 9.22 whereas it has been shown previously that this sensor film is sensitive to relative humidity [6]. This cross-sensitivity could possibly be eliminated by using a dual layer structure in the fabrication of the sensor film i.e. covering the sensor film with a hydrophobic layer to prevent both

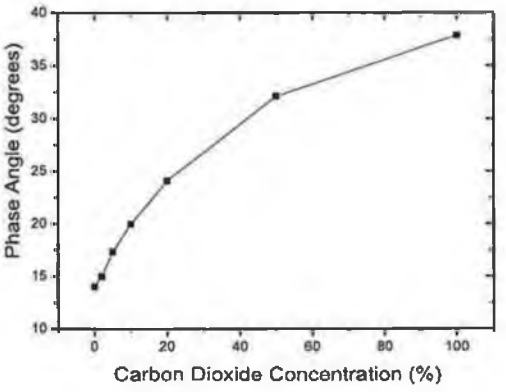

Figure 9.21: Calibration plot for DLR-Based carbon dioxide sensor.

moisture entering and water exiting the sensor matrix. This sensor fabrication method has not been investigated.

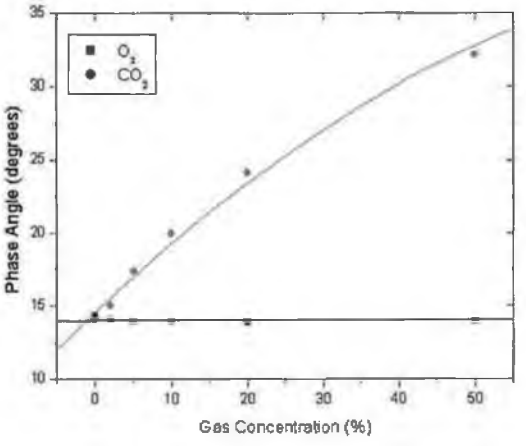

Figure 9.22: Oxygen cross-sensitivity of DLR-based carbon dioxide sensor.

9.4 Multi-analyte Sensing

9.4.1 Oxygen and carbon dioxide

When both oxygen and carbon dioxide sensors had been shown to work separately they were combined on a single chip. For this work a PMMA substrate was used. The 4-channel sensor had an oxygen-sensitive film on two channels and a carbon dioxide sensitive film on the two remaining channels.

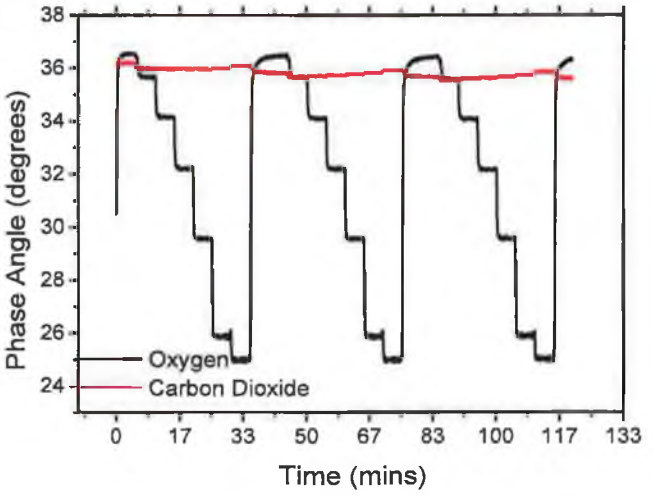

Figure 9.23: Oxygen sensor channel - sensitivity to both oxygen and carbon dioxide.

Each channel was tested individually using the lifetime-based detection set-up. Scans for both gases were carried out on each channel to test both sensitivity and cross sensitivity. In both cases, the gas concentrations were varied from 0% to 100% with 2%, 5%, 10%, 20% and 50% as the intermediate steps. Figure 9.23 shows both the sensitivity to both oxygen and carbon dioxide of an oxygen sensor. Similarly, Figure 9.24 shows the response of the carbon dioxide sensor. Figures 9.23 and 9.24, shows sensitivity to the chosen analyte and the minimal cross-sensitivity to the other analyte for both sensors.

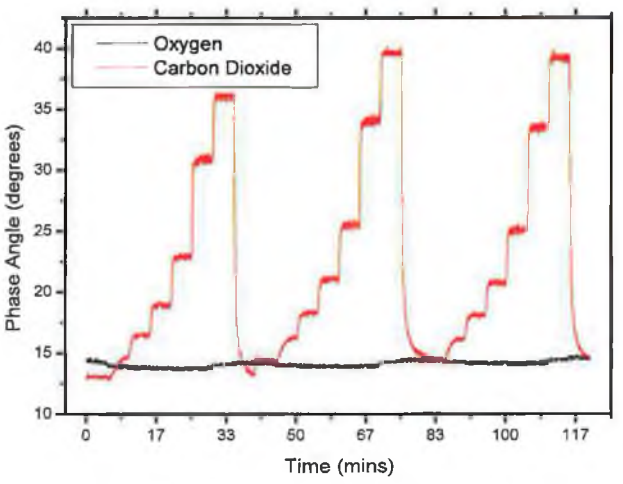

Figure 9.24: Carbon dioxide sensor channel - sensitivity to both oxygen and carbon dioxide.

9.4.2 Oxygen and relative humidity

While data in the previous section show the ability to have sensor channels for two different analytes on a single sensor platform, the fluorescence from each channel was detected individually. The existing lock-in-based fluorescence detection set-up was extended to monitor three separate sensor channels simultaneously. This required the use of three lock-in amplifiers. Figure 9.25 shows the detection system which contains a photodiode and LED for each sensor channel and a single detection filter. This set-up was used to simultaneously measure the output of both an oxygen sensor and a relative humidity sensor. The dual-analyte sensor data are shown in Figures 9.26 and 9.27.

Figure 9.26 shows the response of the humidity sensor as well as the humidity insensitivity of the adjacent oxygen channel. The oxygen response is shown in Figure 9.27. It is clear from this figure that the relative humidity sensor is slightly oxygen sensitive ($\approx$ 1.5° Phase Angle from 0-50% O_2). This effect can either be compensated for in a calibration equation for the sensor or eliminated with the improvement in the sensor dye complex immobilisation chemistry.

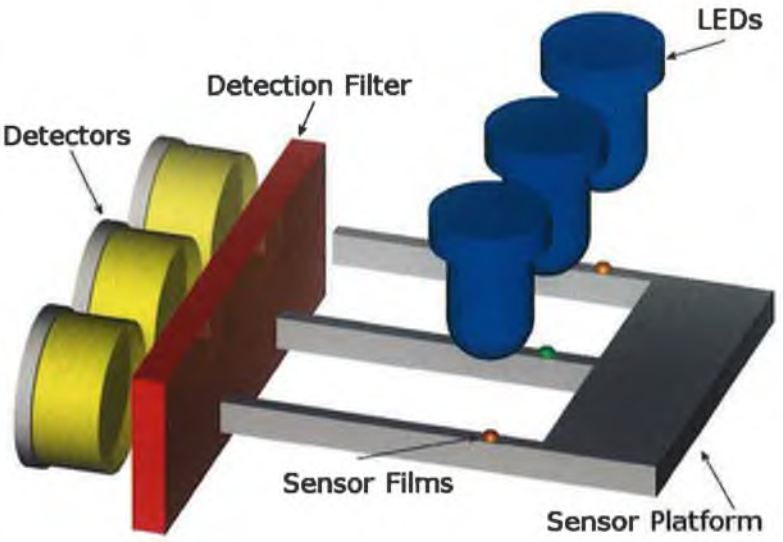

Figure 9.25: Fluorescence detection system to simultaneously monitor three individual sensor channels.

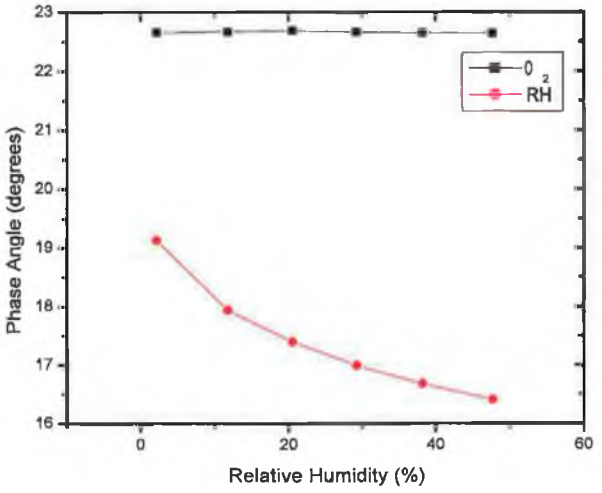

Figure 9.26: Simultaneous multi-analyte response (oxygen and relative humidity) of sensor chip to variations in relative humidity.

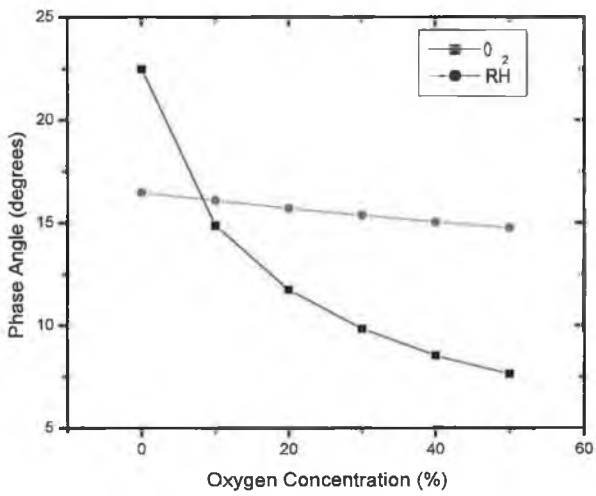

Figure 9.27: Simultaneous multi-analyte response (oxygen and relative humidity) of sensor chip to variations in oxygen.

Curved sensor platform

A final sensor platform based on the use of dual reference phase detection and a curved PMMA platform was developed as described in Section 8.3.3. Oxygen and relative humidity sensor films were deposited on the channels of the chip using micro-contact printing. The fluorescence from both of the sensor films was detected simultaneously using a single photodiode (S1223). A sample of the data collected from both sensors is shown in Figure 9.28.

This scan was performed at 0% oxygen for relative humidity concentrations varied from 0-50% RH. The response from the oxygen sensor is noisy and the signal varies within this noise level for the entire scan and the sensor is therefore either not cross-sensitive to relative humidity or this sensitivity is less than the noise obtained on the data. The relative humidity sensor performance was analysed after a third order exponential fit had been performed on the data. This yielded the resolution and limit of detection values shown in Table 9.3.

The sensitivity of the sensor chip to oxygen was then tested. The cross-sensitivity of the relative humidity sensor to oxygen decreases as the relative humidity increases. This is shown by the resolution and limit of detection increasing

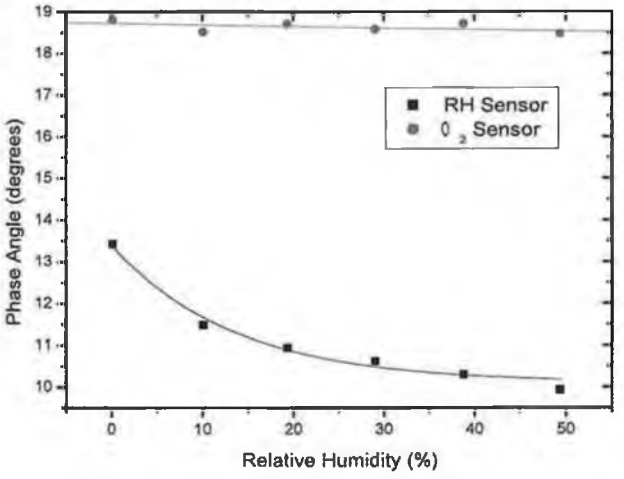

Figure 9.28: Response of oxygen and relative humidity sensor to changing relative humidity measured simultaneously using dual reference phase lock-in detection.

Resolution 0-50% RH	1.15% RH
Limit of Detection	0.32% RH

Table 9.3: Relative humidity sensor performance at 0% oxygen.

(i.e. reduced sensor performance) as the relative humidity increases. This is shown in Table 9.4 where the resolution is calculated from 0-40% oxygen. This effect can also be shown by calculating the change in phase angle, $\Delta\phi$, from 0-40% oxygen at a range of relative humidity concentrations. This is shown in Figure 9.29. As the relative humidity increases the sensitivity to oxygen decreases.

	0% RH	50% RH	100% RH
Resolution (%O_2)	0.42	1.82	3.44
Limit of Detection (%O_2)	0.15	1.10	1.99

Table 9.4: Relative humidity sensor - oxygen cross-sensitivity. Limit of detection and resolution calculated for RH sensor in response to changing oxygen concentrations.

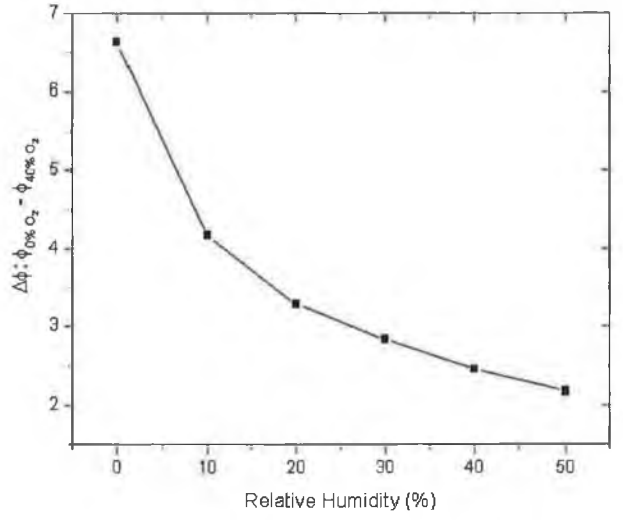

Figure 9.29: Change in phase angle, $\Delta\phi$, for oxygen sensitivity for different relative humidity concentrations.

The performance of the oxygen sensor was also evaluated, in this case at 50% RH. The sensor showed a resolution of 0.12% O_2 from 0-40% O_2 and a limit of detection of 0.04% O_2. This sensor thus performs in a similar manner to the lifetime-based sensor on the earlier PMMA platform using single phase reference

detection as described above in Section 9.1.2.

The use of a dual reference phase lock-in detection method has been successfully demonstrated. While the sensor performance matched that achieved previously for oxygen sensing, the resolution of the relative humidity sensor was not as low as that achieved previously. This was due to noise in both the detection circuitry and also in the reference source which was giving a noisier data signal. For the dual reference phase method to be used successfully, the electronic design would need to be improved. This method of detection could also be extended to multiple channels by replacing the lock-in amplifier with custom-built circuitry to modulate a number of LEDs at different frequencies and to extract each individual signal from the photodiode by using a fourier transform at the required frequency.

9.5 Conclusion

The various sensor platforms that have been developed, as described in Chapter 7, and the evolution of the experimental characterisation systems, as described in Chapter 8, have been applied to the detection of the fluorescence from optical sensors used to measure oxygen, relative humidity and carbon dioxide for indoor air-quality monitoring as described in Chapter 5. The performance of these platforms have been analysed in turn and then extended to detect multiple analytes simultaneously.

A sensor platform was developed based on UV-curable sol-gel waveguides and applied to oxygen sensing. The refractive index of the waveguide layers were altered and the sensor developed from an intensity-based sensor to a lifetime-based sensor with an improved performance.

The second platform material chosen was the polymer PMMA. This platform was developed from requiring separate detectors for each channel or analyte to having a single detector This not only simplifies the platform and decreases the cost, but also eliminates the problem of different response characteristics of the detectors on different channels.

The experimental characterisation system was developed from having an expensive detector, which required cooling and could not be used to measure fluorescence lifetime, to low-cost photodiodes. Intensity-based detection was first used and then the system developed to enable lifetime-based detection. An RF link was also demonstrated which was capable of remote monitoring of data.

The optical sensors were demonstrated for the field of indoor air-quality monitoring. The required analytes detected were oxygen, relative humidity and carbon dioxide. The oxygen sensor performance had a limit of detection of 0.04% O_2 and a resolution of 0.16% O_2 in the range of interest from 0 - 50% O_2. It showed no cross-sensitivity to CO_2 and minimal cross-sensitivity to humidity. The relative humidity sensor gave a limit of detection of 0.62% RH and a resolution of 0.21% RH in the range from 0-50% RH. It showed cross-sensitivity to oxygen but this sensitivity decreases rapidly with increasing relative humidity. This is a small effect ($\approx 0.3\%O_2$) at the more relevant %RH values for this application and can be compensated for in the sensor calibration or further reduced or eliminated by improvement of the immobilisation matrix. Its cross-sensitivity to carbon dioxide itself was negligible but altering the CO_2 concentration also alters the humidity level and thus the sensor response. The carbon dioxide sensor showed a limit of detection of 0.32% CO_2 and a resolution of 0.39% CO_2 in the concentration range of interest i.e. 0-20% CO_2. It showed no cross-sensitivity to oxygen but was extremely moisture sensitive. While the carbon dioxide sensor gives a response at the full range of relative humidity values, repeated testing or storing in non-humid conditions greatly reduces the sensitivity. Again the sensor chemistry needs to be optimised as discussed above to prevent humidity sensitivity. A brief summary of the LOD and resolution obtained for the different sensor films and sensor platforms is shown in Table 9.5

Sensor Platform	Analyte	Range	Resolution	LOD
MIMIC	O_2	0→20%	0.20%	0.10%
Straight PMMA	O_2	0→50%	0.16%	0.04%
Curved PMMA	O_2	0→40%	0.12%	0.04%
Straight PMMA	RH	0→50%	0.92%	0.21%
Curved PMMA	RH	0→50%	1.15%	0.32%
Straight PMMA	CO_2	0→20%	0.39%	0.32%

Table 9.5: Summary of LOD and resolution values for phase-based detection of fluorescence from the different sensor films and sensor platforms.

From this summary, it can be seen that the PMMA sensor platforms give a better performance than the UV curable sol-gel waveguide platforms. While the PMMA platforms are on average 10 times larger than the sol-gel waveguide plat-

forms, the sol-gel waveguides still perform well as optical oxygen sensors. These platforms could be used where the platforms need to be miniaturised to the order of less than 1mm. The PMMA-based sensor platforms give a good sensor performance with the ability of being mass-produced at low-cost and the ability to use less complex optical detectors. The optimum sensor configuration to be used would be the curved PMMA platform and single detector with dual reference phase lock-in detection. Custom-built electronics could be used to monitor multiple analytes at different modulation frequencies when the noise present when using the lock-in amplifier for DRP detection is removed. With improvement of the carbon dioxide sensor, a portable sensor for indoor air-quality sensing can be developed incorporating RF communication of data and sensing all three analytes simultaneously.

Bibliography

[1] C. S. Burke, O. McGaughey, J. M. Sabattié, H. Barry, A. K. McEvoy, C. McDonagh, and B. D. MacCraith. Development of an integrated optic oxygen sensor using a novel, generic platform. *Analyst*, 130(1):41–45, 2005.

[2] D. Wencel, C. Higgins, A. Guckian, C. McDonagh, and B.D. MacCraith. Novel hybrid sol-gel materials for smart sensor windows. *Proc. SPIE*, 5826:696–705, 2005.

[3] O. McGaughey, R. Nooney, A.K. McEvoy, C. McDonagh, and B.D. MacCraith. Development of a multi-analyte integrated optical sensor platform for indoor air-quality monitoring. *Proc. SPIE*, 5993:172–183, 2005.

[4] O. McGaughey, J.V. Ros-Lis, A. Guckian, A.K. McEvoy, C. McDonagh, and B. D. MacCraith. Development of a fluorescence lifetime-based sol-gel humidity sensor. *Analytica Chimica Acta*, 570:15–20, 2006.

[5] O. McGaughey, A.K. McEvoy, and B. D. MacCraith. Development of a multi-analyte optical sensor platform for fluorescence-based sensing. *Paper in preparation.*

[6] C. von Bültzingslöwen. *Development of optical sensors ("optodes") for carbon dioxide and their applications to Modified Atmosphere Packaging (MAP).* Ph.D. Thesis, University of Regensburg, 2003.

Chapter 10

Conclusions

The main objectives of this work were the development of a generic multi-analyte optical sensor platform for fluorescence-based sensing and the development of an absorbance-based portable nitrate sensor capable of real-time in-situ measurements of nitrate concentrations in ground water.

The development of a portable nitrate sensor capable of real-time continuous in-situ measurement of nitrate in ground water was reported in this thesis. The use of recently developed optoelectronic components has enabled the development of a portable sensor prototype for nitrate sensing, alleviating the current necessity for lab-based measurement and enabling real-time in-situ continuous monitoring of nitrate concentrations. An absorption-based optical sensor has been demonstrated which is capable of determining the nitrate concentration in the range 0-100ppm nitrate in clean water samples. A chemometric model was used to calibrate the sensor in the presence of interferences found in ground water and to remove the need for filtering or pre-cleaning of samples. The nitrate sensor was capable of determining nitrate concentration in the range 0-40ppm nitrate with a limit of detection of 1ppm nitrate in the presence of interfering species. This sensor shows improved performance over many commercially available sensors and obviates the need for pre-treatment steps which enables the deployment of the sensor in the field. Further work in this sensor development would necessitate the redevelopment of the prototype sensor probe head to decrease the path length and thus increase the working range of the sensor which is currently limited at higher nitrate concentrations due to saturation effects.

The work presented in this thesis has demonstrated the operation of a fluorescence-based multi-analyte optical sensor platform. This platform has been

designed based on methods for efficient capture of fluorescence and the considerations of a low-cost, disposable, mass-producible sensor platform have also been maintained. Sensor platforms have been fabricated using both polymer and silicon and have been demonstrated as efficient sensor platforms. A range of microfabrication techniques have been used to develop the low-cost sensors. The multi-analyte sensor system was tested for the area of indoor air-quality monitoring and to this end optical chemical sensor films were developed for oxygen, relative humidity and carbon dioxide. All of the sensors were based on the fluorescence of an indicator dye immobilised in a sol-gel matrix. These sensors were developed in such a way as to minimise, where possible, any cross-sensitivity to the other analytes being sensed. Different methods of detecting the optical signal from the sensor and relating it to the analyte concentration have been investigated. A fluorescence lifetime-based sensor has been demonstrated using custom-built electronics and an RF transmitter enabling remote detection of analyte concentration.

The main achievements in this thesis were in the development of an efficient sensor platform for fluorescence capture and an efficient excitation and detection system for fluorescence measurement. Optical chemical sensors for relative humidity and carbon dioxide were developed and then integrated into a multi-analyte sensor with the oxygen sensor and the effect of possible cross-sensitivity between the sensors to be measured studied. Methods of depositing the sensor films onto the sensor platforms were investigated and developed. It was found that different deposition methods best suited the different sensor platforms. The work presented in this thesis demonstrates the ability to simultaneously detect multiple analytes using a single platform and different methods of fluorescence lifetime-based detection. The overall sensor performance reported in Table 9.5 out performs the sensor requirements, as stated in Section 1.2.4, for the chosen application of indoor air quality monitoring. The sensor displays an improved sensitivity and resolution above what is required for the chosen application in addition to having minimal cross-sensitivity to the other analytes being sensed. The sensor platform can thus be used in further applications which require an improved sensor performance relative to indoor air-quality monitoring including, for example, blood gas analysis, food packaging and bioprocess monitoring.

Future work to be undertaken on this project should include the further development of the optical carbon dioxide sensor film with the goal of removing the moisture sensitivity of the sensor. The method of phase-detection with each chan-

nel having a separate modulation frequency to be detected with a single detector should be adopted as the chosen phase measurement technique. The custom-built electronics could thus be modified to include this and detect the fluorescence from multiple sensor films to enable the simultaneous detection of multiple analytes with a single detector as well as incorporating RF communication to enable remote sensing. The final optical sensor platform design should be fabricated using hot embossing enabling the production of higher optical quality sensor platforms capable of efficient detection of fluorescence from multiple optical sensor films.

Appendix A

List of Publications and Conference Presentations

Peer Reviewed Publications

- *"Development of a fluorescence lifetime-based optical relative humidity sensor"* Orla McGaughey, Jose Vincente Ross, Adrian Guckian, Aisling K. McEvoy, Colette McDonagh and Brian D. MacCraith. *Analytica Chimica Acta*, 2006, **570**, 15-20.

- *"Development of an integrated optic oxygen sensor using a novel, generic platform"* Conor S. Burke, Orla McGaughey, Jean-Marc Sabattié, Henry Barry, Aisling K. McEvoy, Colette McDonagh and Brian D. MacCraith. *Analyst*, 2005, **130**, 41-45.

Conference Papers

- *"Development of a multi-analyte integrated optical sensor platform for indoor air-quality monitoring."* Orla McGaughey, Robert Nooney, Aisling K. McEvoy, Colette McDonagh and Brian D. MacCraith, *Optics East: Advanced Environmental, Chemical, and Biological Sensing Technologies III, Proc. SPIE,* Vol 5993, p172-184, 2005.

Conference Presentations

- *"Development of a multi-analyte integrated optical sensor platform for indoor air-quality monitoring."* **Orla McGaughey**, Dorota Wencel, Aisling K. McEvoy, Colette McDonagh and Brian D. MacCraith, Institute of Physics

in Ireland, Spring Weekend, Bundoran, Co. Donegal, April 2006. (*Poster Presentation*)

- *"Development of a multi-analyte integrated optical sensor platform for indoor air-quality monitoring."* **Orla McGaughey**, Robert Nooney, Aisling K. McEvoy, Colette McDonagh and Brian D. MacCraith, Optics East, Boston, September 2005. (*Oral Presentation*)

- *"Development of a sol-gel based integrated optical oxygen sensor using a novel, generic platform."* **Orla McGaughey**, Conor S. Burke, Henry Barry, Jean-Marc Sabattié, Aisling K. McEvoy, Colette McDonagh and Brian D. MacCraith, Opto-Ireland, Dublin, April 2005. (*Oral Presentation*)

- *"Development of a Sol-Gel Based Integrated Optical Oxygen Sensor using Rapid Prototyping Technology"* **Orla McGaughey**, Conor S. Burke, Henry Barry, Jean-Marc Sabattié, Aisling K. McEvoy, Colette McDonagh and Brian D. MacCraith, Institute of Physics in Ireland, Spring Weekend, Newbridge, Co. Kildare, March 2005. (*Poster Presentation*)

- *"Multi-Analyte Optical Sensor Chip"* Orla McGaughey, Aisling K. McEvoy, **Brian D. MacCraith**, Jean-Marc Sabattié, Jérôme Charmet. Europt(r)ode VII, Madrid, April 2004.(*Oral Presentation*)

- *"Multi-Analyte Optical Sensor Chip Based on Photo-Patternable Hybrid Sol-Gel Integrated Optics"* **Jean-Marc Sabattié**, Orla McGaughey, Aisling K. McEvoy, Jérôme Charmet and Brian D. MacCraith. Euromat 2003, Lausanne, September 2003. (*Oral Presentation*)

- *"Multi-Analyte Sensor Chip (MASC)"* **Orla McGaughey**, Aisling K. McEvoy Brian D. MacCraith, Jean-Marc Sabattié, Jérôme Charmet. 4th UK Ireland Sol-Gel Meeting, Cranfield University, May 2003. (*Poster Presentation*)

Appendix B

Evanescent Field Derivation

This derivation of the exponential decline in the cladding region or the evanescent field is a modified version of that found in Optoelectronics by Wilson and Hawkes [3] and is used in Chapter 4

The process of total internal reflection leads to the Fresnel's equations. Figure B.1 shows the situation where light is incident on the boundary between two interfaces. The angles of incidence, transmission and reflection are θ_i, θ_t and θ_r respectively.

These equations describe the magnitude of the transmitted and reflected electric fields relative to the incident field. Two cases need to be considered - one where the electric field vector is parallel to the plane of incidence known as $\varepsilon^{\parallel}$ also known as Transverse Magnetic (TM) polarisation and the second where the electric field vector is perpendicular to the plane of incidence known as $\varepsilon^{\perp}$ also known as Transverse Electric (TE) polarisation. Fresnel's equations can thus be written as:

$$\frac{\varepsilon_r^{\perp}}{\varepsilon_i^{\perp}} = \frac{n_1 \cos\theta_i - n_2 \cos\theta_t}{n_1 \cos\theta_i + n_2 \cos\theta_t} \tag{B.1}$$

$$\frac{\varepsilon_r^{\parallel}}{\varepsilon_i^{\parallel}} = \frac{n_1 \cos\theta_t - n_2 \cos\theta_i}{n_1 \cos\theta_t + n_2 \cos\theta_i} \tag{B.2}$$

and

$$\frac{\varepsilon_t^{\perp}}{\varepsilon_i^{\perp}} = \frac{2n_1 \cos\theta_i}{n_1 \cos\theta_i + n_2 \cos\theta_t} \tag{B.3}$$

$$\frac{\varepsilon_t^{\parallel}}{\varepsilon_i^{\parallel}} = \frac{2n_1 \cos\theta_i}{n_1 \cos\theta_t + n_2 \cos\theta_i} \tag{B.4}$$

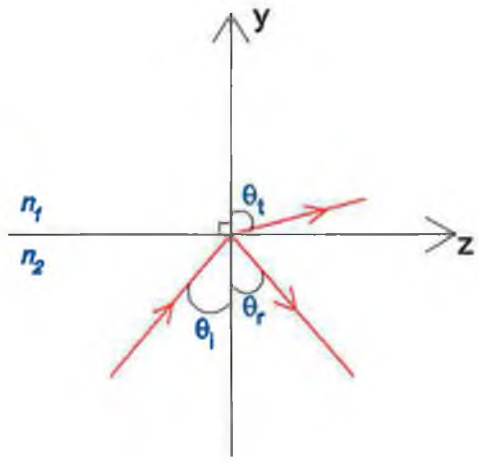

Figure B.1: Light incident on a boundary between two media of different refractive indices.

When $n_1 > n_2$ it is possible to have total internal reflection; that is when $\theta_i > \theta_c$ where

$$\theta_c = \sin^{-1}\left(\frac{n_2}{n_1}\right) \tag{B.5}$$

At the critical angle, θ_c, there is no transmitted wave in the second medium. This can be shown by looking at θ_t,

$$\cos\theta_t = (1 - \sin^2\theta_t)^{\frac{1}{2}} \tag{B.6}$$

And from using Snell's law ($\frac{n_1}{n_2} = \frac{\sin\theta_t}{\sin\theta_i}$) and substituting this in gives

$$\cos\theta_t = \left[1 - \left(\frac{n_1}{n_2}\right)^2 \sin^2\theta_i\right]^{\frac{1}{2}} \tag{B.7}$$

When $\theta_i < \theta_c$, $\sin\theta_i < \frac{n_2}{n_1}$ and $\cos\theta_t$ then becomes wholly imaginary. Therefore,

$$\cos\theta_t = \pm iB \quad (\theta_i > \theta_c) \tag{B.8}$$

where

$$B = \left[\left(\frac{n_1}{n_2}\right)^2 \sin^2\theta_i - 1\right]^{\frac{1}{2}} \tag{B.9}$$

The negative sign solution must be taken as in later discussion of the phase factor, Equation B.17, the positive solution leads to a non-physical solution. The variable A is now defined as

$$A = \left(\frac{n_1}{n_2}\right)\cos\theta_i \tag{B.10}$$

and substituting these variables into Equation B.1,

$$\frac{\varepsilon_r^{\perp}}{\varepsilon_i^{\perp}} = \frac{A + \imath B}{A - \imath B} \tag{B.11}$$

The right hand side of this equation has a modulus of unity which shows that when $\theta_i > \theta_c$ the intensity of the incident and reflected rays are equal confirming there is no transmitted ray and total internal reflection has taken place. Since the electric fields are now complex there is a phase shift present between the incident and reflected beams, which can be calculated by rewriting Equation B.11 as

$$\frac{\varepsilon_r^{\perp}}{\varepsilon_i^{\perp}} = \frac{\cos\psi + \imath\sin\psi}{\cos\psi - \imath\sin\psi} = \frac{\exp(\imath\psi)}{\exp(-\imath\psi)} = \exp(2\imath\psi) \tag{B.12}$$

where

$$\tan\psi = \frac{B}{A} = \frac{n_2\left[\left(\frac{n_1}{n_2}\right)^2\sin^2\theta_i - 1\right]^{\frac{1}{2}}}{n_1\cos\theta_i} \tag{B.13}$$

or

$$\tan\psi = \frac{\left[\sin^2\theta_i - \left(\frac{n_2}{n_1}\right)^2\right]^{\frac{1}{2}}}{\cos\theta_i} \tag{B.14}$$

In a similar manner it can be shown that, Equation B.2, can be rewritten as

$$\frac{\varepsilon_r^{\parallel}}{\varepsilon_i^{\parallel}} = \exp 2\imath\delta \tag{B.15}$$

where

$$\tan\delta = \left(\frac{n_1}{n_2}\right)^2\tan\psi \tag{B.16}$$

The phase changes on reflection for $\varepsilon^{\perp}$ and $\varepsilon^{\parallel}$ are therefore given be 2ψ and 2δ respectively.

Although all the energy in the beam is reflected when $\theta_i > \theta_c$ there is still a disturbance in the second medium whose electric field amplitude decays exponentially with distance away from the boundary. To derive an expression for this decay, the phase factor, P, of the transmitted wave at the point $\boldsymbol{r}$ is

$$P = \exp[\imath(\omega t - \mathbf{k}_t \cdot \mathbf{r})] \tag{B.17}$$

where $\boldsymbol{k}_t$ is the wavevector associated with the transmitted wave and $\boldsymbol{r}$ can be written as $z\sin\theta_t + y\cos\theta_t$ and therefore we have

$$P = \exp(\imath[\omega t - k_t(z\sin\theta_t + y\cos\theta_t)]) \tag{B.18}$$

$$= \exp\left[\imath\left(\omega t - \frac{2\pi n_2}{\lambda_0}(z\sin\theta_t + y\cos\theta_t)\right)\right] \tag{B.19}$$

where λ_0 is the wavelength of the radiation in a vacuum. Substituting in expressions for $\sin\theta_t$ and $\cos\theta_t$ from Equations B.1 and B.6 respectively,

$$P = \exp\left(\imath\left[\omega t - \frac{2\pi n_2}{\lambda_0}\left(z\frac{n_1}{n_2}\sin\theta_i + (\pm\imath B)y\right)\right]\right) \tag{B.20}$$

$$= \exp\left(\pm B\frac{2\pi n_2}{\lambda_0}y\right)\exp\left[\imath\left(\omega t - \frac{2\pi n_1\sin\theta_i}{\lambda_0}z\right)\right] \tag{B.21}$$

Therefore in the y-direction the wave either grows or decays exponentially with distance. The former situation is a non-physical situation and the reason the negative solution should be taken for Equation B.6. The decay with distance in the second medium is given by the factor F(y) where:

$$F(y) = \exp\left(-\frac{2\pi n_2}{\lambda_0}By\right) \tag{B.22}$$

$$F(y) = \exp\left(-\frac{2\pi n_2}{\lambda_0}\left[\left(\frac{n_1}{n_2}\right)^2\sin^2\theta_i - 1\right]^{\frac{1}{2}}y\right) \tag{B.23}$$

The part of the field that is present in the second medium is known as the evanescent field. When θ_i is very different to θ_c the disturbance in the second medium is minimal. But in the other case when $\theta_i \to \theta_c$ than the disturbance will expand a distance into the second medium.

Appendix C

Matlab Scripts for modelling fluorescence

C.1 Dual Luminophore Referencing, DLR

```
% Dlr modelling 6th December 05
% Plotting excitation waveform along with Ru emission,
% HPTS emission and total emission
% Calculating phase shift between Excitation and total emission

phi=30*(pi/180);                              %phi ruthenium
phi2=1*(pi/180);                              %phi HPTS
A=15;                                         %excitation amplitude
a1=10;                                        %ru emission amplitude
%a2=input('Enter indicator amplitude '); %hpts amplitude
a2=1;
%B=10;                                        %excitation dc offset
%b=5;                                         %emission dc offset
f=20000;                                      %modulation frequency
%string=['cmax=',num2str(cmax)];

maxt=1*(1/f);
%no=input('Enter number of points ');
t=linspace(0,maxt,10000);
w=2*pi*f;
```

```
E=A*sin(w*t);                          %excitation
R1=a1*sin((w*t-phi));                  %ru emission
R2=a2*sin((w*t-phi2));                 %hpts emission
R3=R1+R2;                              %total emission


string1=['HPTS Amplitude=',num2str(a2)];
string2=[', Ru Amplitude= ',num2str(a1)];
string3=[', Modulation Frequency= ',num2str(f)];

[emax,no1]=max(E);          %finding max of E and corresponding time
E_t=t(no1);
[r3max,no2]=max(R3);
R_t=t(no2);    %finding max of total emission and corresponding time
dt=R_t-E_t;
deltaphi=dt*(360/5e-5);
string4=[', Phase Shift= ',num2str(deltaphi)];
string=[string1,string2,string3,string4];

subplot(4,1,1)
title(string);
hold on                                %plot ex and ru em
plot(t,E,'b')                          %ex - blue, ru em - red
plot(t,R1,'r')
subplot(4,1,2)
hold on
plot(t,E,'b')                          %plot ex and hpts em
plot(t,R2,'g')                         %ex -blue hpts em - green
subplot(4,1,3)
hold on
plot(t,R1,'r')                         %plot ru em, hpts em and total em
plot(t,R2,'g')                         %total em -black
plot(t,R3,'k')
subplot(4,1,4)
hold on
```

```
plot(t,E,'b')                          %plot ex and total em
plot(t,R3,'k')

outputvalues=[A,a1,a2,phi,phi2,deltaphi];
dlmwrite('outputvalues1.dat',outputvalues,'\t')
output=[transpose(t),transpose(E),transpose(R1),transpose(R2),transpose(R3)];
dlmwrite('aind1.dat',output,'\t')
```

C.2 Effect of Background Fluorescence in Curved Chip Platform

Driver File:

```
global f t phideg phi2deg A a1 a2;

phideg=35;              %phi emission
phi2deg=5;              %phi background
A=200;                  %Excitation Amplitude
a1=200;                 %Emission Amplitude
f=20000;                %Modulation Frequency

phi=phideg*(pi/180);  %Converting phase angles to radians
phi2=phi2deg*(pi/180);

no=1000;                %No. of points
maxt=1*(1/f);
t=linspace(0,maxt,no);

N=length(t);
dphi_save=zeros(1,N);
a2_save=zeros(1,N);

for i=1:N,
a2=i/100;
a2_save(i)=a2;
```

```
dphi=deltaphi(f,t,phideg,phi2deg,A,a1,a2);
%Calculating phi for each value of background amplitude
dphi_save(i)=dphi;
end

output=[transpose(a2_save),transpose(dphi_save)];
dlmwrite('deltaphi.dat',output,'\t')        %Outputting to data file
```

Function File:

```
function dphi=deltaphi(f,t,phideg,phi2deg,A,a1,a2)

phi=phideg*(pi/180);            %phi emission
phi2=phi2deg*(pi/180);          %phi background


w=2*pi*f;
E=A*sin(w*t);                   %excitation
R1=a1*sin((w*t-phi));           %Emission
R2=a2*sin((w*t-phi2));          %Background
R3=R1+R2;                       %total emission

[emax,no1]=max(E);   %finding max of E and corresponding time
E_t=t(no1);
[r3max,no2]=max(R3);
R_t=t(no2);          %finding max of total emission and corresponding time
dt=R_t-E_t;
dphi=dt*(360/5e-5);
%Calculating dphi phase diff between excitation and total emission
```

Appendix D

Electronic Circuit Diagrams

This appendix shows the electronic circuit diagrams for the various circuits used in the course of this work. All circuits were designed and fabricated by John Moore.

D.1 Photodiode Pre-Amplification Circuit

Figure D.1 shows the pre-amplification circuit used in conjunction with the Hamamatsu S1223 photodiode for fluorescence measurements.

D.2 LED Current Modulation Circuit

The circuit used for current modulation of the LED is shown in Figure D.2. This was used for the curved chip measurements.

D.3 MASC 4-Channel PCB for Phase Fluorometry

The circuit diagrams which form the MASC 4-channel PCB for phase fluorometry are shown. The circuit diagram is split into four parts. The first section, Figure D.3, shows the power and thermistor connections for the board. The LED current modulation circuitry and the photodiode control circuitry are shown in Figure D.4 and Figure D.5 respectively. While only one channel is displayed there are also three other identical channels making up the four channel board. The main control calculation part of the board including the PIC and RF output is shown in Figure D.6.

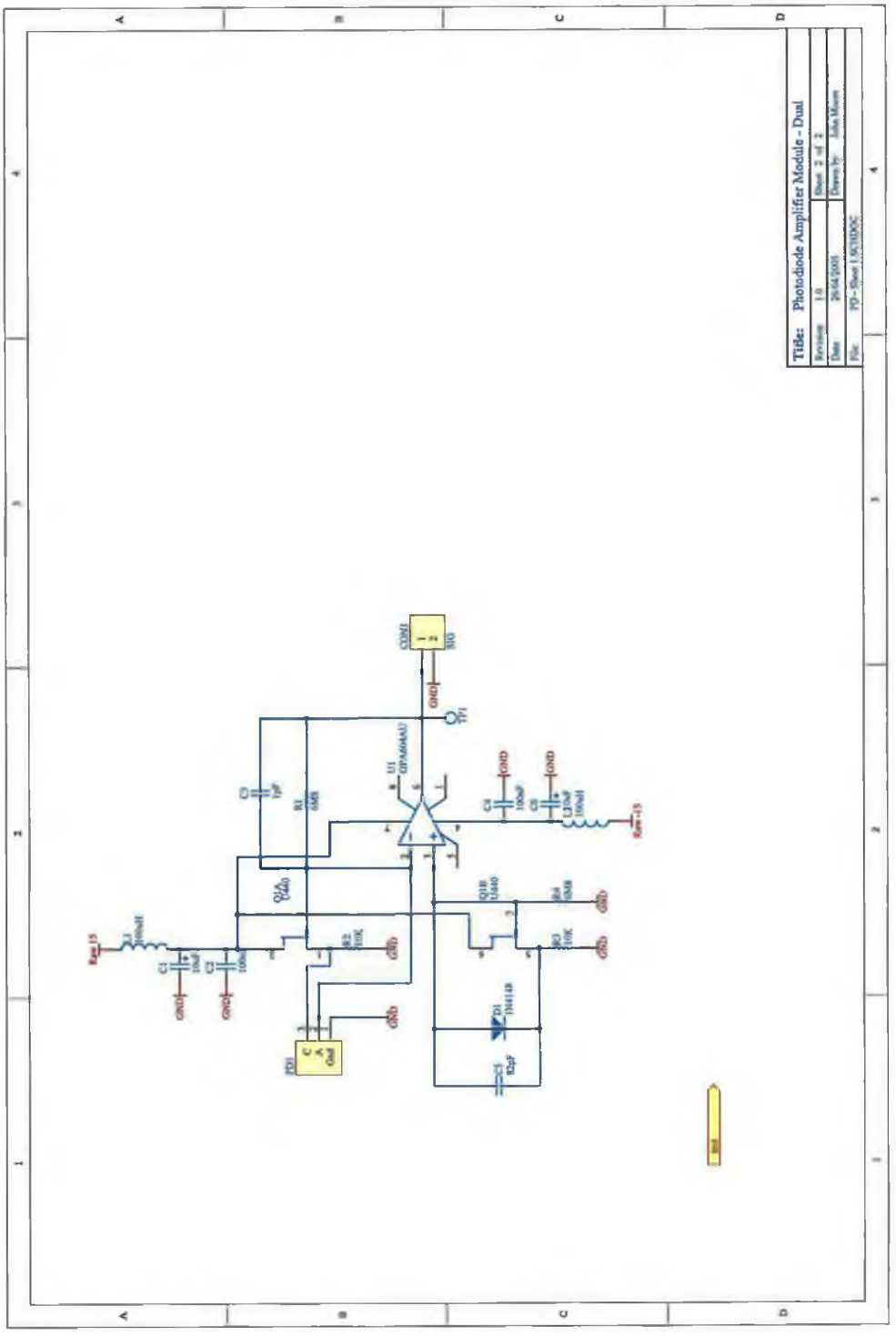

Figure D.1: Photodiode pre-amplification circuit diagram.

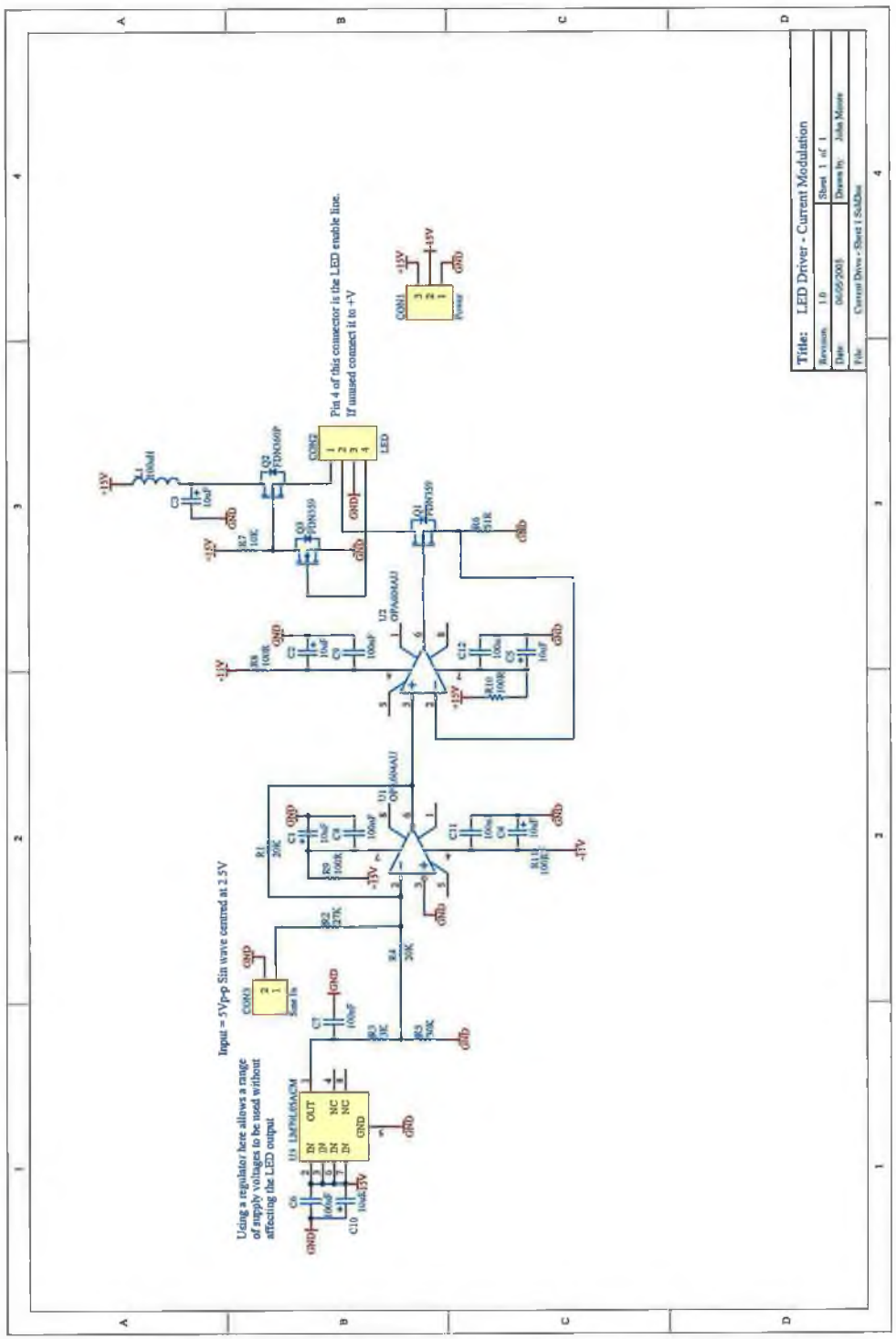

Figure D.2: LED current modulation circuit diagram.

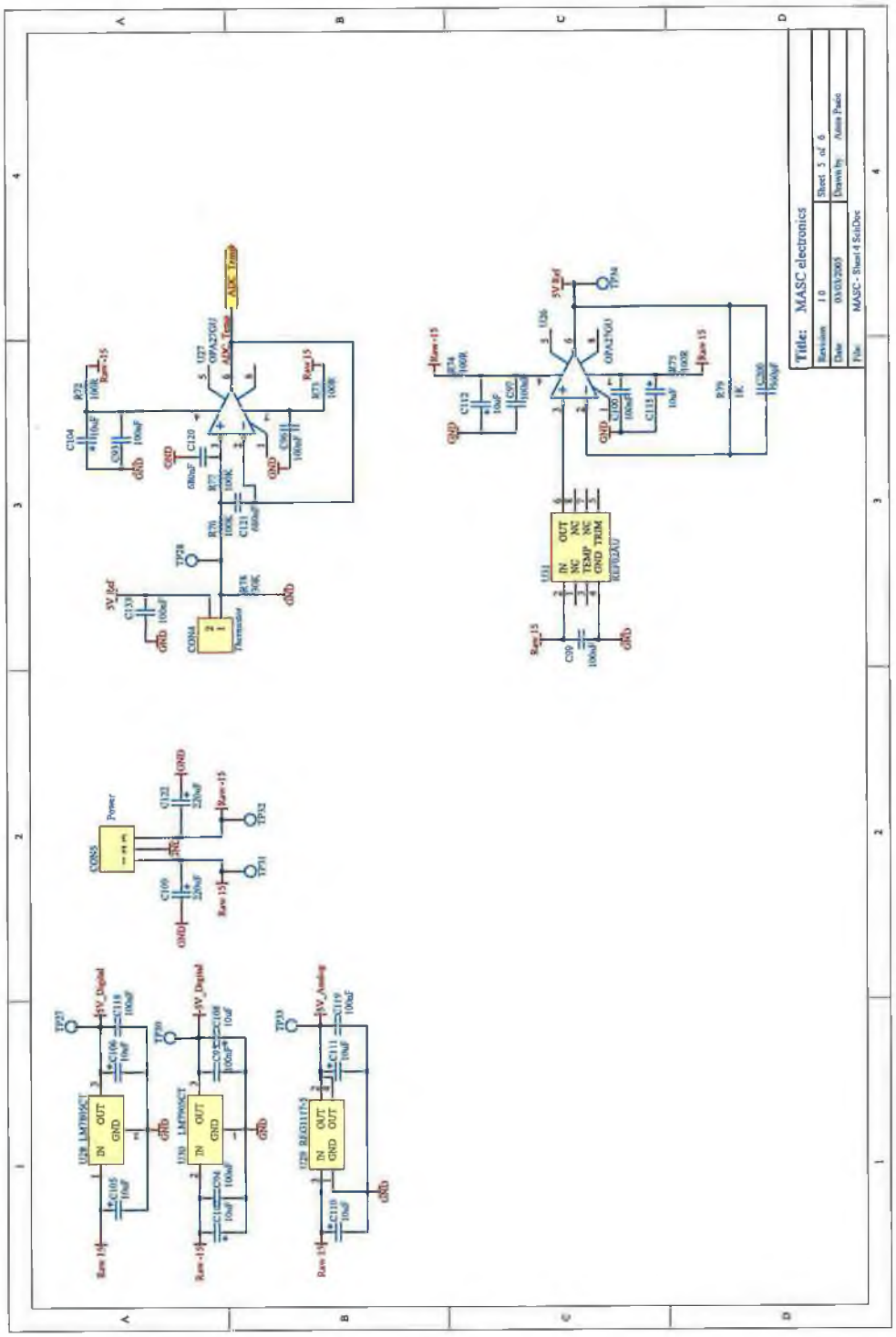

Figure D.3: MASC 4-channel PCB power and thermistor circuit diagrams.

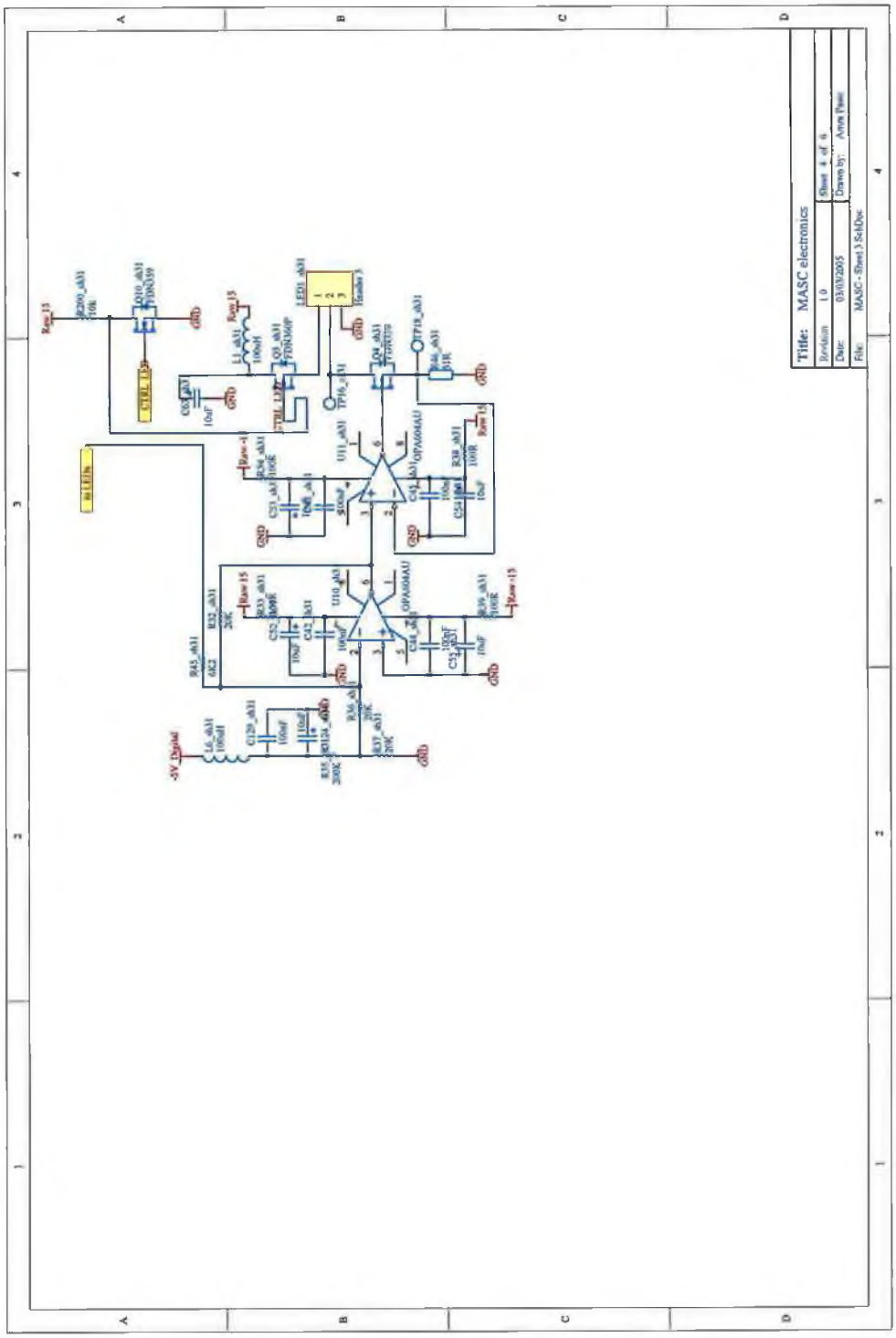

Figure D.4: LED current modulation circuit diagram from MASC 4-channel PCB.

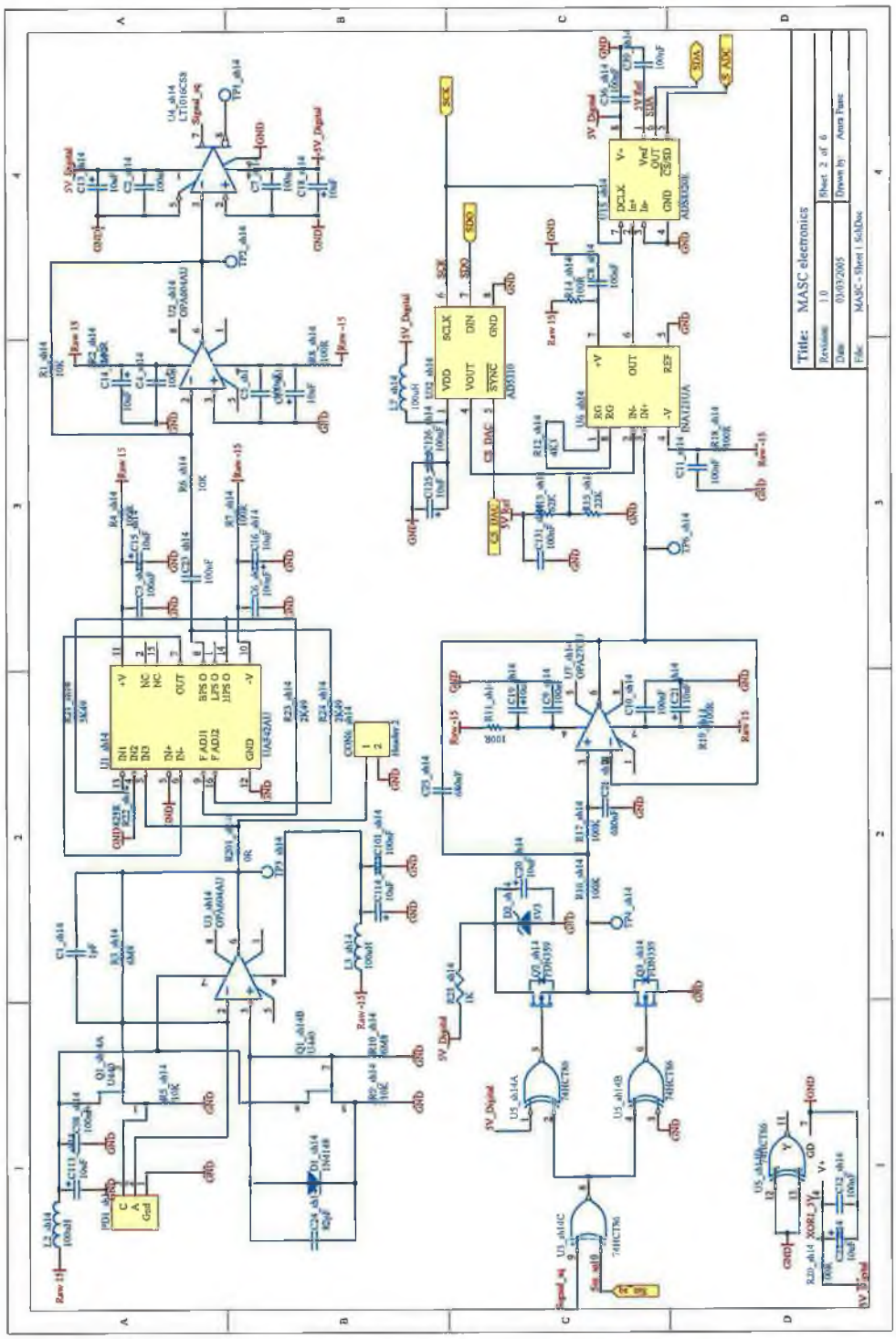

Figure D.5: Photodiode control circuit diagram from MASC 4-channel PCB.

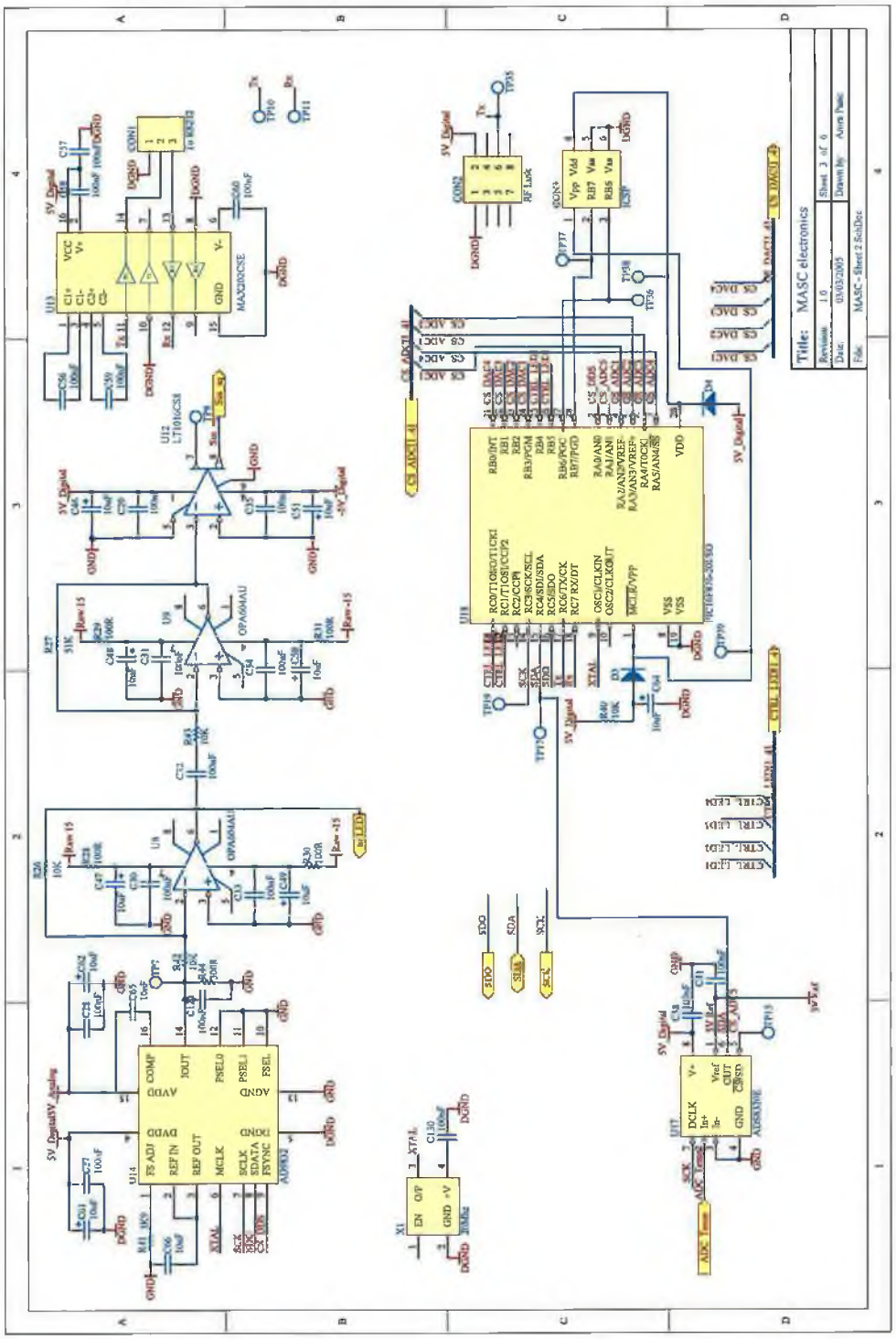

Figure D.6: MASC Board.

D.4 Relative humidity and temperature sensor

The relative humidity and temperature sensor used for the curved chip measurements, Sensirion SHT75 (Sensirion; U.K.) consisted of a digital meter which outputted values which could be processed via a programmable interface controller (PIC) and sent to a computer serial port. The circuit diagram for the sensor control circuit is shown in Figure D.7.

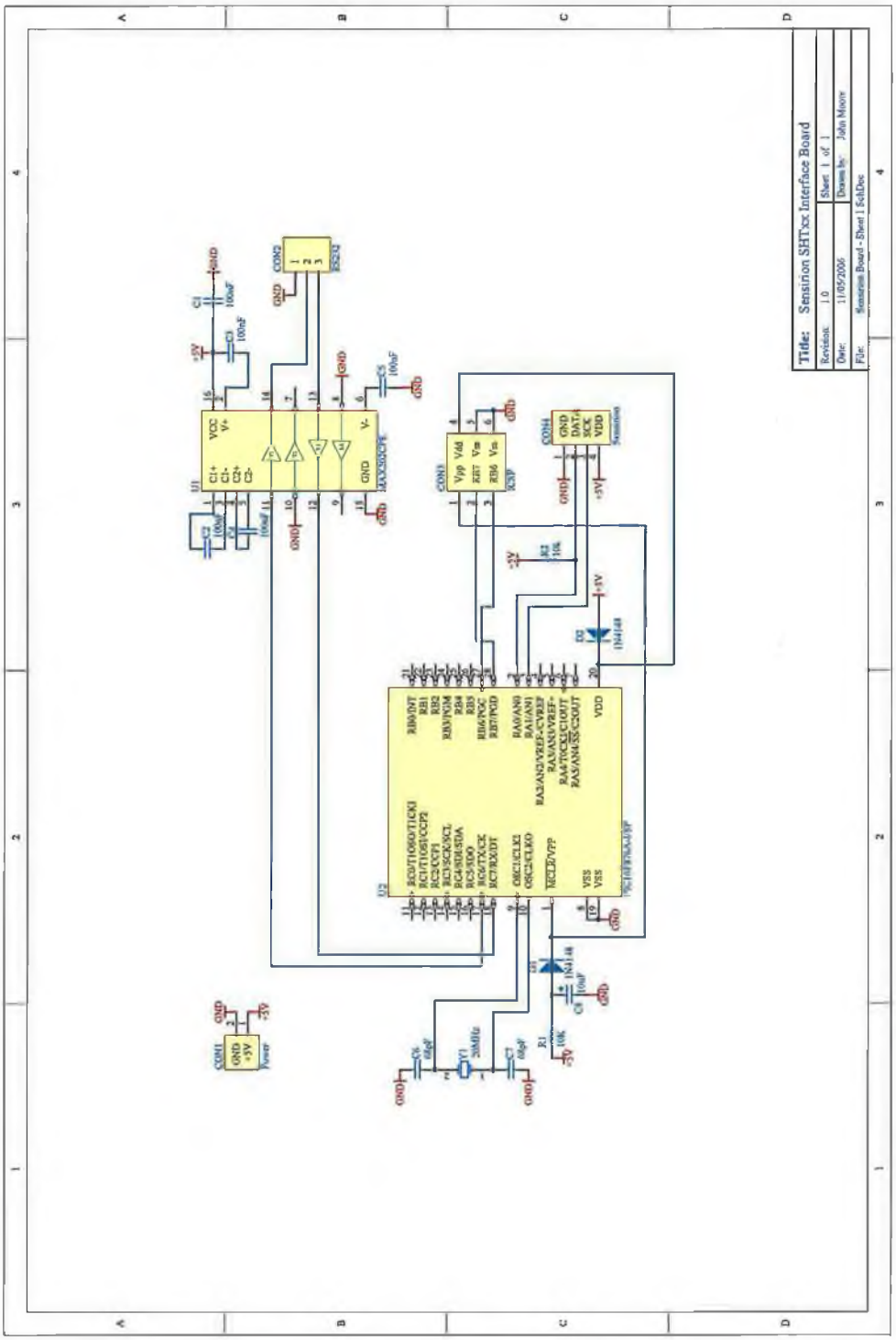

Figure D.7: Control circuit for Sensirion SHT75 relative humidity and temperature sensor.